Modelling Oxygen Isotopes in the UVic Earth System Climate Model Under Preindustrial and Last Glacial Maximum Conditions: Impact of Glacial-Interglacial Sea Ice Variability on Seawater $\delta^{18}O$

by

Catherine Elizabeth Brennan
B.A., Wellesley College, 2000
M.Sc., the Pennsylvania State University, 2006

A Dissertation Submitted in Partial Fulfillment of the
Requirements for the Degree of

DOCTOR OF PHILOSOPHY

in the School of Earth and Ocean Sciences

Modelling Oxygen Isotopes in the UVic Earth System Climate Model Under Preindustrial and Last Glacial Maximum Conditions: Impact of Glacial-Interglacial Sea Ice Variability on Seawater δ^{18}O

by

Catherine Elizabeth Brennan
B.A., Wellesley College, 2000
M.Sc., the Pennsylvania State University, 2006

Supervisory Committee

Dr. Andrew J. Weaver, Co-Supervisor
(School of Earth and Ocean Sciences)

Dr. Katrin J. Meissner, Co-Supervisor
(School of Earth and Ocean Sciences)

Dr. Kirsten Zickfeld, Departmental Member
(School of Earth and Ocean Sciences)

Dr. Diana Varela, Outside Member
(Department of Biology)

Supervisory Committee

Dr. Andrew J. Weaver, Co-Supervisor
(School of Earth and Ocean Sciences)

Dr. Katrin J. Meissner, Co-Supervisor
(School of Earth and Ocean Sciences)

Dr. Kirsten Zickfeld, Departmental Member
(School of Earth and Ocean Sciences)

Dr. Diana Varela, Outside Member
(Department of Biology)

ABSTRACT

Implementing oxygen isotopes ($H_2^{18}O$, $H_2^{16}O$) in coupled climate models provides both an important test of the individual model's hydrological cycle, and a powerful tool to mechanistically explore past climate changes while producing results directly comparable to isotope proxy records. The addition of oxygen isotopes in the University of Victoria Earth System Climate Model (UVic ESCM) is described. Equilibrium simulations are performed for preindustrial and Last Glacial Maximum (LGM) conditions. The oxygen isotope content in the model's preindustrial climate is compared against observations for precipitation and seawater. The distribution of oxygen isotopes during the LGM is compared against available paleo-reconstructions.

Records of temporal variability in the oxygen isotopic composition of biogenic carbonates from ocean sediment cores inform our understanding of past continental ice volume and ocean temperatures. Interpretation of biogenic carbonate $\delta^{18}O$ variability typically neglects changes due to factors other than ice volume and temperature, equivalent to assuming constant local seawater isotopic composition. This

investigation focuses on whether sea ice, which fractionates seawater during its formation, could shift the isotopic value of seawater during distinct climates. Glacial and interglacial states are simulated with the isotope-enabled UVic ESCM, and a global analysis is performed. Results indicate that interglacial-glacial sea ice variability produces as much as a 0.13 permil shift in local seawater, which corresponds to a potential error in local paleotemperature reconstruction of approximately 0.5°C. Isotopic shifts due to sea ice variability are concentrated in the Northern Hemisphere, specifically in the Labrador Sea and northeastern North Atlantic.

Contents

List of Tables

List of Figures

ACKNOWLEDGEMENTS

I would like to thank:

my supervisors, Andrew Weaver and Katrin Meissner, for your kind support, continual encouragement, and invaluable academic guidance.
Your mentoring has deeply inspired me, for which I am ever grateful.

my UVic Climate Lab colleagues, especially Michael Eby and Ed Wiebe, for all the technical help, scientific advice and friendship a PhD student could want.

my partner, Tony Gilman, and our friends and families, for the love and joy that has illuminated my academic and life journey.

DEDICATION

To my ancestors, and to the great, unknown future.

Chapter 1

Introduction

The main goal of this thesis is to describe the implementation of stable water oxygen isotopes within the University of Victoria Earth System Climate Model (UVic ESCM), the evaluation of the isotope-enabled model for pre-industrial and Last Glacial Maximum (LGM) climates, and the application of the model to address a longstanding problem in paleoceanography: whether different sea ice conditions resulting from distinct climate states (e.g. interglacial versus glacial) may shift the isotopic content of seawater.

Parts of this thesis have been previously published by or submitted to peer-reviewed journals. The full references are included in the thesis bibliography (Brennan et al., 2012b,a) and are listed here:

- Brennan, C.E., A.J. Weaver, M. Eby, and K.J. Meissner, Modelling oxygen isotopes in the University of Victoria Earth System Climate Model for preindustrial and Last Glacial Maximum Conditions, *Atmosphere-Ocean*, doi:10.1080/07055900.2012.707611, 2012 (in press).

- Brennan, C.E., K.J. Meissner, M. Eby, C. Hillaire-Marcel, and A.J. Weaver, Impact of sea ice variability on the oxygen isotope content of seawater under glacial and interglacial conditions, *Paleoceanography*, manuscript 2012PA002385, 2012 (submitted). Reproduced by permission of American Geophysical Union.

The aims of this chapter are as follows:

1. List the key components of the research;

2. List the primary results of the work;

3. Describe the significance of the work;

4. Describe the structure of the thesis document.

1.1 Research contributions and primary results

The key contributions of the completed work are (**I.**) the full implementation of stable water oxygen isotopes within the ocean, atmosphere, land surface, and sea ice subcomponents of the UVic ESCM, and (**II.**) the isotope-enabled model investigation of how changes in sea ice conditions between glacial and interglacial states may result in a shift in local seawater δ^{18}O.

The primary results detailed within this thesis are summarized by the following:

I. Implementing stable water oxygen isotopes in the UVic ESCM results in:

1. A new model capability to simulate δ^{18}O, a ubiquitous paleoproxy.
2. A modelled distribution of pre-industrial δ^{18}O in precipitation and seawater.
3. A LGM-specific modelled distribution of δ^{18}O in precipitation and seawater.

II. Investigating the impact of glacial-interglacial sea ice variability on seawater isotopic chemistry indicates:

1. Glacial and interglacial sea ice conditions produce distinct 3-dimensional distributions of δ^{18}O in seawater.
2. High-latitude surface waters in the North Atlantic, specifically in the Labrador Sea and northeastern North Atlantic, undergo the largest isotopic shift – up to 0.13‰;
3. Deep water δ^{18}O is essentially unaffected by sea ice variability.

Claim **I** will be examined by describing the implementation of oxygen isotopes in the model, comparing the modelled distribution of isotopes for pre-industrial and LGM conditions to available observations, and assessing the model results. Claim **I** implies

that:

1. The large scale spatial patterns of observed present day δ^{18}O in precipitation can be captured by the UVic ESCM with a simplified atmosphere model sub-component.

2. Under LGM conditions, the modelled distribution of δ^{18}O in precipitation shifts, producing large scale patterns similar to other isotope-enabled models, but not well reproducing the isotopic shifts reconstructed from < 30 individual ice cores.

Claim **II** will be demonstrated through the description and analysis of model experiments.
Claim **II** implies that:

1. The isotopic signature of sea ice in seawater varies with sea ice conditions.

2. While sea ice conditions varied in both Northern and Southern Hemispheres, the isotopic impact is significant only in the Northern Atlantic Ocean, in surface waters.

3. The results do not support the hypothesis of enhanced sea ice brine production transferring isotopically depleted surface water to depth in the North Atlantic during Last Glacial stadial periods when overturning ceased.

This research has resulted in the production of the first oxygen isotope enabled climate model in Canada, which is one of very few coupled atmosphere-ocean models, and one of very few Earth System Models of Intermediate Complexity (EMICs), in which oxygen isotopes are represented throughout the hydrologic cycle. Employing this model, one may efficiently investigate processes occurring at the ocean-atmosphere or ocean-cryosphere interface that can affect the distribution of oxygen isotopes in seawater. I have conducted a set of experiments to determine whether changes in sea ice production contributed to the isotopic excursions observed in the glacial Labrador Sea pycnocline and Northeastern Atlantic surface and deep water. This analysis allows the first global model estimates of the isotopic contribution of sea ice to seawater δ^{18}O for the pre-industrial and the LGM. These results comprise a new understanding of an open question in paleoceanography.

1.2 Significance of This Work

The representation of stable water oxygen isotopes within the UVic ESCM is significant given the following:

- The isotope-enabled model code will be made publicly available, providing interested UVic ESCM users the possibility of constructing their own model investigations of processes producing shifts in the distribution of stable water oxygen isotopes.

Investigating the impact of glacial-interglacial sea ice variability on seawater isotopic chemistry is significant, given the following:

- This work produces the first estimate of the 3-dimensional seawater δ^{18}O fields that result only from sea ice processes in interglacial and glacial climate states.
- Likewise, this work results in the first estimate of the shift in local seawater δ^{18}O due to interglacial-glacial sea ice variability.
- Researchers employing foraminiferal δ^{18}O records derived from high latitude sediment cores, especially in the North Atlantic, will find the results of this work useful, as it will aid them in:
    1. Determining whether interglacial or glacial sea ice brine or meltwater may influence the isotopic content of planktonic and benthic foraminiferal shells at a particular sediment core location;
    2. Diagnosing the potential contribution of sea ice processes to the isotopic content in interglacial and glacial seawater at the sediment core site;
    3. Providing an estimate of the magnitude of the interglacial-glacial isotopic shift in seawater due to changes in sea ice between interglacial and glacial conditions.
- This work finds no evidence for an interglacial-glacial shift in the δ^{18}O of bottom waters in the global oceans (Atlantic, Pacific, Indian and Southern Oceans) due to changes in sea ice, and therefore indicates that paleoreconstructions of sea level based on benthic foraminiferal δ^{18}O variability do not include errors due to sea ice variability.

1.3 Outline

Below I provide a short summary of the main focus of each chapter of the dissertation.

Chapter 1 contains a statement of the claims which will be proved by this dissertation followed by an overview of the structure of the document itself.

Chapter 2 introduces the rationale for modelling oxygen isotopes, as well as motivating the question of why sea ice variability should be considered in the context of changes in seawater isotopic composition between glacial and interglacial climates.

Chapter 3 describes the implementation of oxygen isotopes in the UVic model.

Chapter 4 consists of the experimental design and modelling approach, and the evaluation of the model experiments.

Chapter 5 summarizes the key results.

Appendix A describes how oxygen isotopes are partitioned within the earth system, and their usefulness to paleoclimatology.

Appendix B provides details of isotope representation within the UVic ESCM and additional model testing.

Appendix C consists of supplemental figures of modelled interglacial-glacial sea ice variability.

Chapter 2

Modelling Oxygen Isotopes in UVic ESCM: Paleoclimate motivation and application

2.1 Oxygen isotope enabled paleoclimate modelling

From ocean sediment cores to ice cores to speleothems, measurements of oxygen isotopes and the corresponding estimates of changes in temperature and the hydrologic cycle have permitted reconstructions of past climate variability. Isotope-enabled models have likewise figured prominently in questions concerning hydrologic cycling under modern and past climates. Since the pioneering implementation of stable water isotopes in the LMD atmospheric general circulation model (AGCM) by Joussaume et al. (1984), the modern distribution of stable water isotopes in the atmosphere is increasingly well captured in models (e.g., Hoffmann et al., 1998; Lee et al., 2007; Werner et al., 2011). Additionally, the comparison of modelled stable water isotope variability to isotope records from ice and sediment cores (e.g., Roche et al., 2004a; LeGrande et al., 2006) and cave deposits (stalagmites) (e.g., Langebroek et al., 2011) has undoubtably advanced the understanding of past climate changes, and illuminated records of modern climate variability. Forward modeling of stable water isotopes, combined with model-data intercomparison, is likely to grow as an important contributor to understanding past climate changes.

Stable water isotopes have been implemented in a range of atmosphere, ocean, and coupled models to date. Of these, few are fully coupled atmosphere-ocean mod-

els, and fewer still are Earth system models of intermediate complexity (or EMICs). The isotope-enabled UVic ESCM may fill a unique role in that it is an intermediate complexity model with a full ocean GCM (as opposed to the EMIC CLIMBER-2 with a zonally-averaged 3-basin ocean model), and the atmosphere and ocean models are fully-coupled for all fluxes (heat, moisture, oxygen isotopes, etc.). As an intermediate complexity model (due to it's 2-D, vertically integrated atmosphere), the UVic ESCM combines computational efficiency with a complete representation of ocean dynamics. Ultimately, the goal of modelling oxygen isotopes using the UVic ESCM is to investigate the distribution of isotopes in seawater under different climate conditions, with the objective of improving the interpretation of oxygen isotope records from ocean sediment cores.

The implementation of stable oxygen water isotopes ($H_2^{18}O$, $H_2^{16}O$) in the UVic ESCM is presented in this dissertation, with an investigation into changes in seawater isotopic content due to glacial-interglacial sea ice variability. Equilibrium simulations for two distinct climates, the preindustrial (year 1800) and LGM (21 kyr BP, kyr = 1000 years and BP = before present) are performed, and the model's distribution of oxygen isotopes is evaluated with respect to available observations and reconstructions.

Oxygen isotope content is expressed as the ratio (R) of $H_2^{18}O$ to $H_2^{16}O$, or more typically, as $\delta^{18}O$ when referenced to the Vienna Standard Mean Ocean Water (V-SMOW) standard: $\delta^{18}O = (R/R_{VSMOW} - 1) \times 10^3$) in units of permil (‰). The terms *enriched* or *more positive* indicate a shift towards more $H_2^{18}O$ and therefore larger R and $\delta^{18}O$ values. Conversely, the terms *depleted* or *more negative* indicate a shift towards less $H_2^{18}O$ and therefore smaller R and $\delta^{18}O$ values. An introduction to stable oxygen isotopes, including their partitioning within the Earth system and usefulness as recorders of paleoclimate information, is provided in Appendix A.

2.2 Impact of Sea Ice Variability on Seawater $\delta^{18}O$

Oxygen isotope content measured in biogenic carbonates derived from ocean sediment cores constitutes a key paleoproxy, its record of temporal and spatial variation having provided a wealth of knowledge informing past ocean and climate conditions. Variations in mean seawater $\delta^{18}O$ on timescales of 10^3 to 10^5 years result from changes in continental ice volume. However, ocean organisms secrete carbonate shells in temperature-dependent equilibrium with their local seawater environment. As de-

scribed by Waelbroeck et al. (2002), the isotopic changes (thus, $\Delta\delta$) recorded by benthic foraminifera ($\Delta\delta^{18}O_b$) reflect both changes in the isotopic composition of seawater ($\Delta\delta^{18}O_w$) and changes in temperature ($\Delta\delta^{18}O_{temp}$). The changes in the isotopic composition of seawater can be further decomposed into changes in the mean isotopic state of the ocean ($\Delta\delta^{18}O_{icevol}$) (a function of how much depleted ice is stored on the continents), and changes in the local seawater isotopic composition ($\Delta\delta^{18}O_{local}$), such that:

$$\begin{aligned}\Delta\delta^{18}O_b &= \Delta\delta^{18}O_w + \Delta\delta^{18}O_{temp} \\ &= \Delta\delta^{18}O_{icevol} + \Delta\delta^{18}O_{local} + \Delta\delta^{18}O_{temp} \end{aligned} \tag{2.1}$$

(Waelbroeck et al., 2002, their Eqn. 1).

Local seawater $\delta^{18}O$ depends on the isotopic content of its water source and the sum of any upstream isotopic contributions. The balance of surface evaporation and precipitation of source water (when the water parcel was last in contact with the atmosphere), additions of river runoff, ice sheet melt, and sea ice brine and melt, as well as ocean circulation all may affect $\delta^{18}O_{local}$ (Rohling and Bigg, 1998). Each of these processes contributing to $\delta^{18}O_{local}$ may change in time and space. By extension, assuming any factor to be constant can introduce error to paleoreconstructions. Neglecting a variable component of seawater $\delta^{18}O$ when interpreting isotopic records from ocean sediments may, in effect, superimpose error upon the resulting paleoreconstruction. The alternative is to acknowledge process variability, where possible. Here I investigate sea ice variability on glacial-interglacial timescales, and the extent to which the isotopic signature of sea ice in seawater may fluctuate.

Sea ice formation is accompanied by fractionation of stable water isotopes, such that newly formed sea ice is enriched in $H_2^{18}O$ relative to seawater, and the expelled sea ice brine is depleted (O'Neil, 1968). Thus, sea ice growth represents the only process by which changes in seawater salinity and isotope content are negatively correlated (see discussion in Hillaire-Marcel and de Vernal (2008)). Sea ice is dynamic, and may form (and expel depleted brines) in one location and melt (depositing enriched meltwater into surface waters) in a distant location. The presence or absence of sea ice meltwater or brines may therefore produce an isotopic shift in surface waters, as large as the isotopic shifts found in the paleorecord (cf. Tan and Strain (1980)).

2.2.1 Sea ice growth and brine formation

When new sea ice forms in open water, freezing produces ice crystals, which congelate into a layer of ice. The resulting sea ice consists of a complex network of (fresh) ice, pockets of brine, solid salts, and air. During freezing, brine is expelled to the underlying water. This sea ice system has a typical salinity of 5 (Malmgren, 1927), although is highly variable. The ice may continue to grow at the ice-water interface through accretion to the ice base. As the sea ice grows thicker, a complex network of brine inclusions in the ice may drain, reducing the salinity of first year ice. In contrast to the variability of first-year ice salinity, multiyear ice has a mean salinity of 4 ± 1, as summarized in Ekwurzel et al. (2001).

2.2.2 Sea ice growth and isotopic fractionation

As seawater freezes, fractionation takes place between water molecules. With its larger mass, the molecule $H_2^{18}O$ exhibits a lower vibrational frequency and zero-point energy (relative to $H_2^{16}O$). The heavier molecule is therefore slightly preferred within the solid ice structure. In fresh water, this leads to a freezing induced fractionation of 3.0 permil at equilibrium, such that ice is enriched (by 3‰) (O'Neil, 1968). During the formation of sea ice, ice is enriched by up to a maximum of 3‰ and the expelled sea ice brine is depleted by the equivalent amount.

In fact, the magnitude of fractionation may vary with the rate of ice growth, such that larger fractionation occurs with slower ice growth (Eicken, 1998). As discussed by Ekwurzel et al. (2001), a range of fractionation factors for newly formed sea ice have been determined in the field based on the $\delta^{18}O$ values in ice and the underlying seawater. For example, Melling and Moore (1995) found a mean fractionation of 2.5‰ in the Beaufort Sea, Macdonald et al. (1995) measured a fractionation of 2.6 ± 0.1‰ in the Arctic, and Eicken (1998) observed a maximum 2.7‰ fractionation factor in the Weddell Sea. Pfirman et al. (2004) found a $\sim$ 2‰ fractionation at the base of Arctic multiyear ice, while Ekwurzel et al. (2001) determined that Arctic modern conditions could theoretically result in fractionation ranging from 1.5‰ to 2.7‰.

2.2.3 Glacial-interglacial sea ice variability

Considering glacial and interglacial climate states, one would expect significant changes in patterns of sea ice extent, volume, and rates of growth and melt – both spatially

(e.g. for the Arctic, North Atlantic, and Southern Ocean) and temporally (e.g. shifts in the seasonal cycle of sea ice processes at a given location). For example, the present day Arctic exhibits a large annual cycle of ice growth and melt, whereas during the LGM the Arctic Ocean would have been permanently ice-covered, with significantly thicker ice and lower in situ rates of ice growth and melt. Regions further south not subject to present day sea ice would have seen seasonal ice cover. For example, evidence suggests that winter sea ice extended to $\sim 55°$N in the central and eastern North Atlantic and to 40°N along the coast of North America (Kucera et al., 2005; de Vernal et al., 2005). Glacial-interglacial differences in sea ice seasonality and spatial patterns have been investigated using microfossil-based transfer functions, including dinoflagellate cysts and diatoms, in the northern North Atlantic (de Vernal et al., 1994; de Vernal and Hillaire-Marcel, 2000; Rochon et al., 1998), the Southern Ocean (Crosta et al., 1998) and northern Pacific (Sancetta, 1983; de Vernal and Pedersen, 1997).

Sea ice variability may encompass changes in: 1) the areal extent of summer and winter ice, 2) ice thickness, 3) rates of ice production, 4) locations of ice growth and melt. Hillaire-Marcel and de Vernal (2008) investigated the potential for variable sea ice production to shift $\delta^{18}O_w$ in the Labrador Sea pycnocline between late Holocene, Heinrich event, and Last Glacial Maximum (LGM) conditions. Those authors found a pattern of off-equilibrium isotopic excursions (of ~ -1 to -2‰) during Heinrich events (with no associated change in surface salinity) that was not evident during the LGM. This difference was attributed to high sea ice production and brine addition to the pycnocline during Heinrich conditions, in contrast with insignificant LGM sea ice production.

Sea ice brines increase water mass density, and contribute to deepwater formation (Redfield and Friedman, 1969). To what extent sea ice brines may have played a larger role as a mechanism of North Atlantic deep water production during stadials, and in particular, Heinrich events, during the Last Glacial (60 to 10 kyr BP) (Dokken and Jansen, 1999; Vidal et al., 1998) is a matter of controversy. The Last Glacial is the most recent glacial period (110 to 10 kyr BP) since the last interglacial, and stadials are the cold phases (alternating with warmer phases, known as interstadials). Dokken and Jansen (1999) proposed that freshwater additions to surface water during Last Glacial stadials caused overturning circulation to cease, and instead brine formation functioned as the main deepwater formation mechanism in the North Atlantic. This idea, which became known as the sea ice brine hypothesis, was invoked to explain the

observed isotopic depletion in both planktonic and benthic foraminiferal δ^{18}O values in the Nordic Seas during Last Glacial stadials between 60 and 10 kyr BP. They proposed that enhanced sea ice brine production in the Nordic Seas transported surface waters which were already depleted by freshwater additions to depth. Processes with the potential to shift Last Glacial δ^{18}O in polar North Atlantic benthic foraminifera were investigated by Bauch and Bauch (2001), who concluded that only by invoking high rates of sea ice production on a seasonally ice-free shelf in the Barents Sea could a -1‰ benthic shift result in the Nordic Seas, and other processes (i.e. not brine formation) remained more likely. While the balance of evidence calls into question the sea ice brine hypothesis for the Nordic Seas during Heinrich events in particular (Bauch and Bauch, 2001; Stanford et al., 2011), the possibility of sea ice changes shifting subsurface seawater δ^{18}O may be applicable elsewhere, especially, as discussed by Stanford et al. (2011), in cold, high-salinity waters (Rasmussen and Thomsen, 2010). The extent to which sea ice variability holds the potential to produce a deepwater isotopic shift has not been explored in a general circulation model.

Disentangling the individual roles of processes contributing to local seawater δ^{18}O, and assessing how each may vary through time (e.g. between different climate states), is a problem uniquely suited to oxygen isotope-enabled climate models. Using an isotope-enabled coupled climate model, this work attempts to characterize the isotopic signature of sea ice in seawater under two climate end-members (interglacial and full glacial), and investigate the potential role of sea ice variability in shifting local seawater δ^{18}O.

Chapter 3

Implementation and evaluation of stable water oxygen isotopes in UVic ESCM

This thesis presents two main contributions, the first being the representation of oxygen isotopes within the UVic ESCM, and the second the analysis of the extent to which sea ice variability between glacial and interglacial climates can shift local seawater $\delta^{18}O$, and thus impose error to paleo-reconstructions when this process is not accounted for.

This chapter describes:

- UVic ESCM version 2.9.
- model implementation of water isotopes $H_2^{18}O$ and $H_2^{16}O$ within atmosphere, ocean, land surface, and sea ice model subcomponents.
- evaluation of the modelled distribution of $\delta^{18}O$ for preindustrial and Last Glacial Maximum conditions.

3.1 Model description

The UVic ESCM version 2.9 is a fully coupled ocean-atmosphere-land surface-sea ice model without flux adjustments, fully described by Weaver et al. (2001) and Meissner et al. (2003). Horizontal resolution is uniformly 3.6 degrees (longitude) by 1.8 degrees (latitude) in all model subcomponents. The ocean general circulation

model has 19 vertical levels. Ocean diffusivity in the horizontal is $k_h = 8 \times 10^2 m^2 s^{-1}$, and in the vertical varies from thermocline $k_v = 0.3 \times 10^{-4} m^2 s^{-1}$ to deep ocean $k_v = 1.3 \times 10^{-4} m^2 s^{-1}$ (after Bryan and Lewis (1979)). Ocean mixing by mesoscale eddies is parameterized via the Gent and McWilliams (1990) isopycnal diffusion scheme.

The atmosphere model consists of vertically-integrated energy and moisture balance equations, and is forced by seasonally-varying solar insolation and NCEP reanalysis winds (Kalnay et al., 1996). Atmospheric moisture transport is achieved through diffusion and advection by winds. More specifically, the moisture advection scheme applies a wind field calculated as the weighted average of the NCEP long term monthly mean winds (from atmospheric levels below $10,000$ m) (Kalnay et al., 1996). The weighting of the NCEP winds decreases exponentially with height to account for the exponential decrease in atmospheric water vapour with height. Superimposed wind anomalies are calculated dynamically as a function of surface temperature gradients, as described by Weaver et al. (2001). Moisture diffusion coefficients vary with latitude and are held constant in time. Zonal diffusivity is essentially symmetric around the equator, and achieves peak values between 40 and 50 ° in both hemispheres. In contrast, meridional diffusivity is higher in the southern hemisphere, with peak values occurring between 40 and 50 °S. Meridional (zonal) diffusivity ranges from 0.8 to $3.56 \times 10^6 m^2 s^{-1}$ (0.05 to $3.1 \times 10^7 m^2 s^{-1}$). The parametrization of atmospheric moisture diffusivity is different from the K (ADVDIF) originally described in Weaver et al. (2001). After the implementation of the dynamic vegetation scheme by Meissner et al. (2003), the diffusivity scheme was modified to its current form. Here, diffusivity varies only with latitude, and K consists of different coefficients for meridional and zonal moisture diffusivity (see left panel in Figure 3.1).

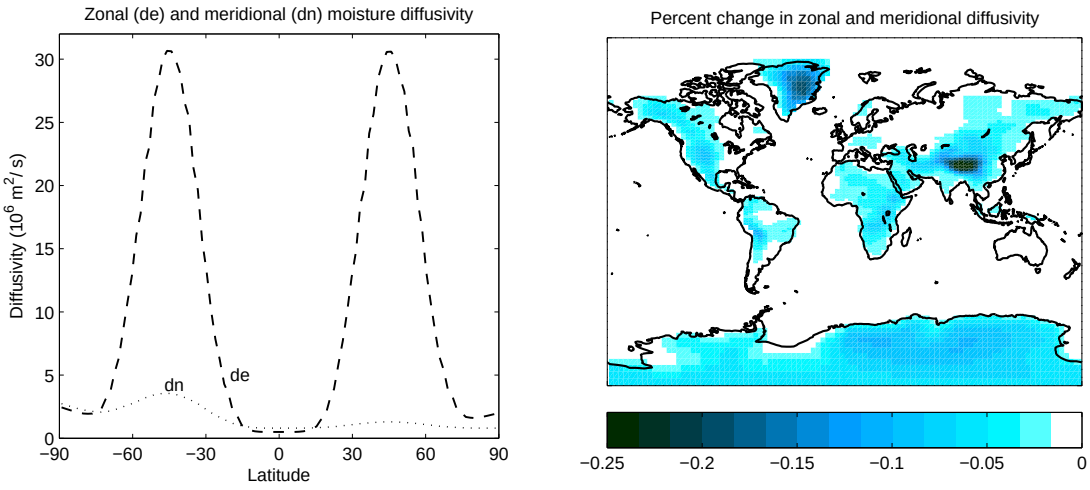

Figure 3.1: Model atmospheric water vapour diffusivity. Variation of initial model zonal (de) and meridional (dn) $H_2^{16}O$ diffusivity with latitude (left), and percent change in zonal and meridional diffusivity for $H_2^{18}O$ relative to $H_2^{16}O$ (maximum reduction is 0.25%) (right).

The land surface model employs a dynamic vegetation land surface scheme (MOSES/ TRIFFID) using a one-layer soil moisture (leaky bucket) representation (Meissner et al., 2003), which runs off to one of thirty-two rivers according to which river catchment basin the gridcell is located within. Snow may accumulate as a single, height-varying layer in the land surface model, with snowmelt either replenishing soil moisture or contributing to river runoff when the soil is saturated.

The standard thermodynamic-dynamic sea ice model (Semtner, 1976; Hibler, 1979) employed here consists of sub-gridscale ice-covered and open-ocean categories, with a height-varying sea ice layer and elastic viscous plastic ice rheology (Hunke and Dukowicz, 1997). Snow falling on sea ice may accumulate as a single height-varying snow layer. The sea ice model is described in detail below, since the impact of sea ice variability between interglacial and glacial states upon $\delta^{18}O$ in seawater is the topic of the following chapter.

3.1.1 Sea ice model

The standard thermodynamic-dynamic sea ice model is based on work by Maykut and Untersteiner (1971) and the zero-layer ice model by Semtner (1976), and employs the lateral growth and melt parameterization of Hibler (1979). Model sea ice manifests

elastic viscous plastic dynamics, the elastic viscous ice rheology based on work by Hibler (1979) and the plastic component contributed by Hunke and Dukowicz (1997). The two-category sea ice model operates upon the domain of ocean grid cells at the sub-grid scale level, such that each grid cell is characterized by an open water areal fraction (ao) and an ice covered areal fraction (ai), with the two categories summing to one ($ao + ai = 1$). Sea ice is assumed to form as a horizontally-uniform slab, and snow may accumulate on top of the ice as a single horizontally-uniform layer. The layers of sea ice and overlying snow may each vary in height, although the snow layer is limited to a thickness of 10 m. The top surface of the sea ice or snow layer may sublimate to the atmosphere. At the ice-ocean interface, ice may grow via accretion or decrease via melt (ablation) (depending upon the balance of ocean heat and ice diffusive fluxes). Brine pockets within sea ice are not explicitly represented, and model sea ice is considered as fresh for purposes of freshwater flux exchange with the ocean model. Brine rejection is parameterized in the model, such that when sea ice forms in the model, expelled brine is added to the underlying water. A determination of water column stability is performed, and if instability exists then convective vertical mixing ensues (Duffy and Weaver, 1999; Weaver et al., 2001). The thermodynamic and dynamic equations used in the standard sea ice model are summarized in Weaver et al. (2001).

3.2 Implementation of Oxygen Isotopes

Moisture is modelled explicitly as humidity in the atmosphere model, soil moisture and lying snow in the land surface model, and ice and overlying snow in the sea ice model. I assumed the pre-existing model moisture to consist of the isotopic species $H_2^{16}O$, and I added equivalent $H_2^{18}O$ reservoirs. On land, $H_2^{18}O$ is represented in soil moisture and in snow lying on the land surface. In the sea ice model, $H_2^{18}O$ is represented in the ice layer and the overlying snow layer.

The rigid-lid ocean model employs a constant-volume assumption such that salt fluxes are substituted for moisture fluxes, necessitating the addition of both $H_2{}^{18}O$ and $H_2{}^{16}O$ as ocean tracers (as in Tindall et al. (2009)). At the sea surface, variations in isotopic content result from evaporation, precipitation, sea ice growth and melt, and inputs of river runoff. Away from the sea surface, $H_2{}^{18}O$ and $H_2{}^{16}O$ are essentially passive tracers due to the absence of subsurface sources or sinks. While seafloor water-rock interaction fractionates oxygen isotopes in seawater, with low (high) temperature

interaction producing depleted (enriched) seawater (Walker and Lohmann, 1989), these water-rock isotope exchange processes are considered to be in isotopic balance on the time scales applicable to our model simulations (i.e. $< 10^5$ yr, contrasted with a shift of 1‰ every 10^8 yr described by Walker and Lohmann (1989)).

Following the implementation of stable water isotopes in other models (e.g., Hoffmann et al., 1998; Lee et al., 2007; Tindall et al., 2009), $H_2{}^{18}O$ undergoes exchange across surface boundaries and fractionation during the appropriate phase changes, summarized in Table 3.1. Figure 3.2 presents a schematic of the isotope-enabled UVic ESCM. Additional model equations and results from model testing are presented in Appendix B.

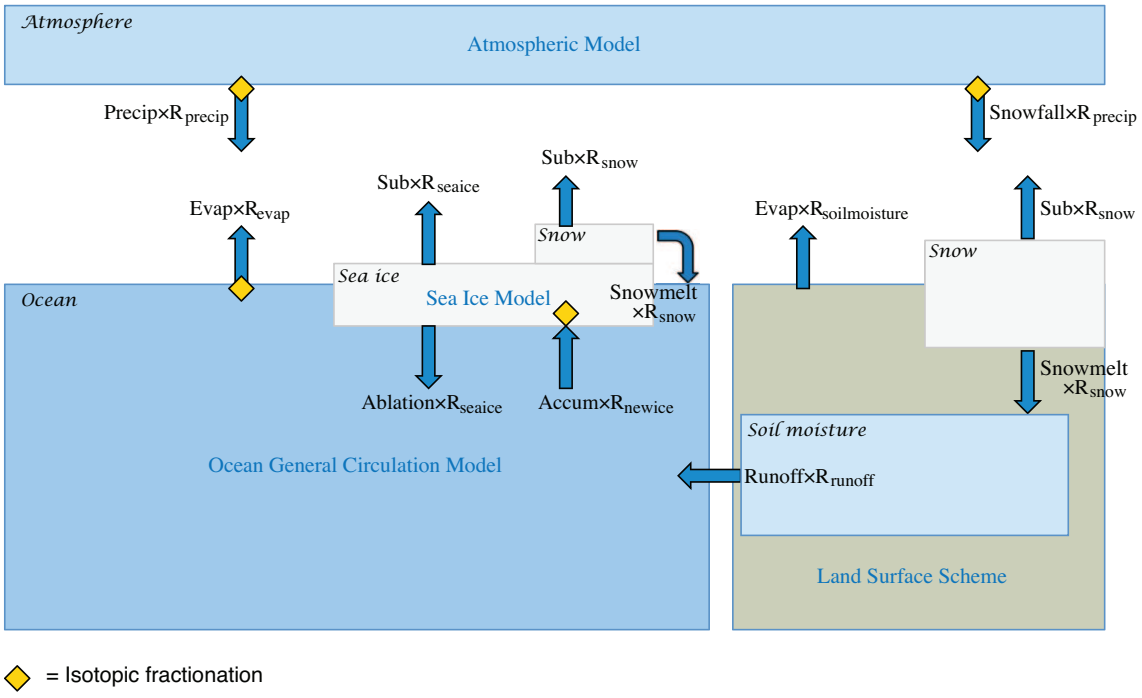

Figure 3.2: Schematic of the isotope-enabled UVic ESCM. Fluxes of $H_2^{18}O$ between model components are shown (blue arrows), equal to the moisture flux (Precip = precipitation, Evap = evaporation, Sub = sublimation, Accum = accumulation) multiplied by the oxygen isotopic ratio (R=$H_2^{18}O/H_2^{16}O$) determined for the flux. Isotopic fractionation occurs in the model at phase changes indicated by the yellow diamond.

Table 3.1: Oxygen isotope fractionation during surface exchanges and phase changes.

Process	**Fractionation**	
Condensation, vapour-liquid ($T \geq -10°C$)	$R_p = \alpha_{eq} R_v$	$ln\alpha_{eq} = \frac{1.137\times10^3}{T^2} - \frac{0.4156}{T} - 2.0667 \times 10^{-3}$ (Majoube, 1971b)
Condensation, vapour-ice ($T < -10°C$)	$R_p = \alpha_{eq} R_v$	$ln\alpha_{eq} = \frac{11.839}{T} - 28.224 \times 10^{-3}$ (Majoube, 1971a)
Condensation, vapour-ice ($T < -20°C$)	$R_p = \alpha_{eq}\alpha_{kin} R_v$	$ln\alpha_{eq} = \frac{11.839}{T} - 28.224 \times 10^{-3}$ (Majoube, 1971a) $\alpha_{kin} = \frac{S}{\alpha_{eq}\times\frac{D}{D_i}\times(S-1)+1}$ (Jouzel and Merlivat, 1984) $S = 1 - 0.0004T$ (Jouzel et al., 1987b)
Evaporation from sea surface	$R_e = \frac{\alpha_{eq}^{-1} R_{oc} - h R_v}{(1-h)(\frac{\rho_i}{\rho})}$	$ln\alpha_{eq} = \frac{1.137\times10^3}{T^2} - \frac{0.4156}{T} - 2.0667 \times 10^{-3}$ (Majoube, 1971b) $\frac{\rho_i}{\rho} - 1 = \theta \cdot n \cdot C_D$ (Gat, 1996)
Evaporation from soils	$R_e = R_s$	
Freezing (sea ice growth), liquid-ice	$R_i = \alpha_{eq} R_{oc}$	$\alpha_{eq} = 1.003$ (O'Neil, 1968)
Sublimation, solid-vapour	$R_v = R_i$	
Transpiration, liquid-vapour	$R_e = R_s$	

R = mass ratio $H_2^{18}O/H_2^{16}O$ for precipitation (p), atmospheric vapour (v), ice (i), evaporation (e), seawater (oc), and soil moisture (s); α = fractionation factor, with α_{eq} and α_{kin} the equilibrium and kinetic fractionation factors (respectively); S = supersaturation parameter; T = temperature (in K for α_{eq} expressions, $°C$ for S expression); D, $D_i = H_2^{16}O$, $H_2^{18}O$ diffusivities; h = relative humidity; ρ_i/ρ = ratio of effective resistances for $H_2^{18}O$ and $H_2^{16}O$ (in the Craig and Gordon (1965) linear-resistance type model for evaporation of isotopic species); following Gat (1996), evaporation under open-water conditions is represented in the selection of constants $\theta = 0.5$ and $n = 0.5$, while $C_D = 28.5‰$.

3.2.1 Condensation

Precipitation forms in the model when atmospheric relative humidity is above 85%. Precipitation occurs under Rayleigh (or open system) conditions, as rain or snow that forms in the model is immediately removed from the atmosphere without any exchange with ambient vapour (see Dansgaard (1964) and Joussaume and Jouzel (1993) for treatment of modelling precipitation in open versus closed systems). At temperatures above -20°C, all precipitation forms in thermal equilibrium with the atmospheric vapour and is enriched relative to the vapour by α, the equilibrium fractionation factor, such that $R_{precip} = \alpha R_{vapour}$. As in Jouzel et al. (1987b), it is assumed that the isotopic vapour condenses to liquid at or above -10°C, and forms a solid otherwise. The appropriate equilibrium fractionation factors from Majoube (1971b,a) are applied for vapour-liquid and vapour-solid transitions (respectively). An additional kinetic fractionation is included at temperatures below $-20\,$°C to account for the effects of differential molecular diffusion of $H_2^{18}O$ and $H_2^{16}O$ through a supersaturated layer surrounding an ice crystal (described in Jouzel and Merlivat (1984)). After Schmidt et al. (2005), the supersaturation is parameterized as $S_{ice} = 1 - 0.004T$ (T is air temperature, °C) (such that S_{ice} varies between 1 and the ratio of saturation vapour pressures of ice to water (see Jouzel et al. (1987b))). Fractionation effects during condensation are summarized in Table 3.1.

3.2.2 Evaporation

Fractionation during evaporation from the sea surface depends on the moisture and isotope gradients at the ocean-atmosphere interface, and takes into account both equilibrium effects (i.e. temperature-dependent) and kinetic effects (i.e. due to the differences in molecular diffusivity for $H_2^{18}O$ and $H_2^{16}O$). The isotopic fluxes in evaporation are well described by the Craig-Gordon evaporation model (Craig and Gordon, 1965), which is based on a Langmuir resistance model. In the Craig-Gordon model, the evaporative flux of $H_2^{16}O$ (E) is a simple function of the humidity gradient between the sea surface boundary (where relative humidity is equal to one) and aloft (characterized by relative humidity h). The evaporative flux driven by the humidity gradient is reduced by a resistivity parameter, ρ, such that $E = (1-h)/\rho$. Likewise, the evaporative flux of $H_2^{18}O$ (E_i) includes the additional assumption that the vapour at the sea surface boundary is in isotopic equilibrium with the seawater (therefore equal to R_{oc}/α_{eq}), while the atmospheric water vapour aloft has isotopic content of R_v,

giving $E_i = (R_{oc}\alpha_{eq}^{-1} - hR_v)/\rho_i$. As discussed in Gat (1996), the kinetic fractionation effects due to differential molecular diffusion in air for $H_2^{18}O$ and $H_2^{16}O$ are included in the resistivity coefficients. The resulting ratio of $H_2^{18}O$ and $H_2^{16}O$ in evaporation, or R_e, is simply equal to E_i/E, shown in Table 3.1.

When snow or ice sublimates, the entire sublimated layer is removed to the atmosphere, and no fractionation occurs. Likewise, transpiration by plants communicates unfractionated root water (i.e. soil moisture) to the atmosphere (Gat, 1996). Evaporation from bare soil is also returned to the atmosphere without fractionation in the model. While evaporation from a soil column should include fractionation in theory (due to vertical humidity and isotopic gradients between saturated and undersaturated soils), this process is neglected for the sake of simplicity (following most models). Since bare soil evaporation is small compared to the total evaporative flux, this simplification should have a minor effect. The isotopic content in soil moisture (R_s) depends on the balance of isotopic fluxes in precipitation and evaporation. Fractionation processes during evaporation are summarized in Table 3.1.

3.2.3 Sea ice formation

When sea ice forms in the model, the ice is enriched by 3.0‰ relative to its seawater source. This fractionation factor is identical to that employed in other isotope-enabled coupled models (for example, the GISS (Schmidt et al., 1999) and GENESIS-MOM (Mathieu et al., 2002) models), although it is slightly larger than the values observed in field studies discussed previously (see Section 2.2.2). Snowfall that accumulates on top of sea ice in the snow layer retains its isotopic content separately. Isotopes in sea ice and the overlying snow layer may be transferred to the atmosphere via sublimation, and to the surface ocean via melting. No fractionation occurs during either sublimation or melting, since it is assumed that an entire layer of ice or snow is removed to the atmosphere or ocean.

3.2.4 Moisture transport over elevation

In an earlier version of the model, precipitation was not sufficiently depleted when atmospheric humidity was transported over grid cells containing higher land elevation (relative to the low elevation precipitation, as compared to both observations and AGCMs with multiple levels in the vertical). The likeliest explanation is that because the UVic model does not resolve atmospheric vertical convection, moisture

transported to higher elevations would simply condense at colder temperatures from overly enriched vapour (as opposed to the depleted vapour aloft found in AGCMs, presumably via distillation from vertical air motion). To address this problem, the diffusion of $H_2^{18}O$ is decreased by an elevation-dependent amount. The difference in atmospheric diffusivity between $H_2^{18}O$ and $H_2^{16}O$ is zero over ocean points, negligible over low elevation (most continental points), and important only over significant high elevation regions (Antarctica, Greenland, and the Himalayas), shown in Figure 3.1 (right). While the highest model elevation is found in Eastern Antarctica (which is more than 1000 m higher than central Greenland), the percent reduction is larger in Greenland because the initial absolute value of the meridional moisture diffusivity coefficient is smaller at 70°N than at 82°S.

3.3 Preindustrial Equilibrium Simulation: Setup and Climatology

The model preindustrial climatology discussed here results from a 5 kyr simulation with constant radiative forcing conditions such that solar forcing is based on year 1800 orbital configuration, and pCO_2 is set to 283.87 ppm. The ocean model is initialized to 0.1‰, the atmosphere humidity to −10‰, and other water reservoirs to 0‰.

The UVic ESCM present day climatology has been fully described by Weaver et al. (2001). For reference, the model (preindustrial) surface air temperature and precipitation (both annual mean and seasonal variation, defined as DJF-JJA) are presented in Figures 3.3 and 3.4. The differences between the model fields and the corresponding NCEP reanalysis fields are included to highlight model-data discrepancies, which could potentially shift the resulting distribution of isotopes.

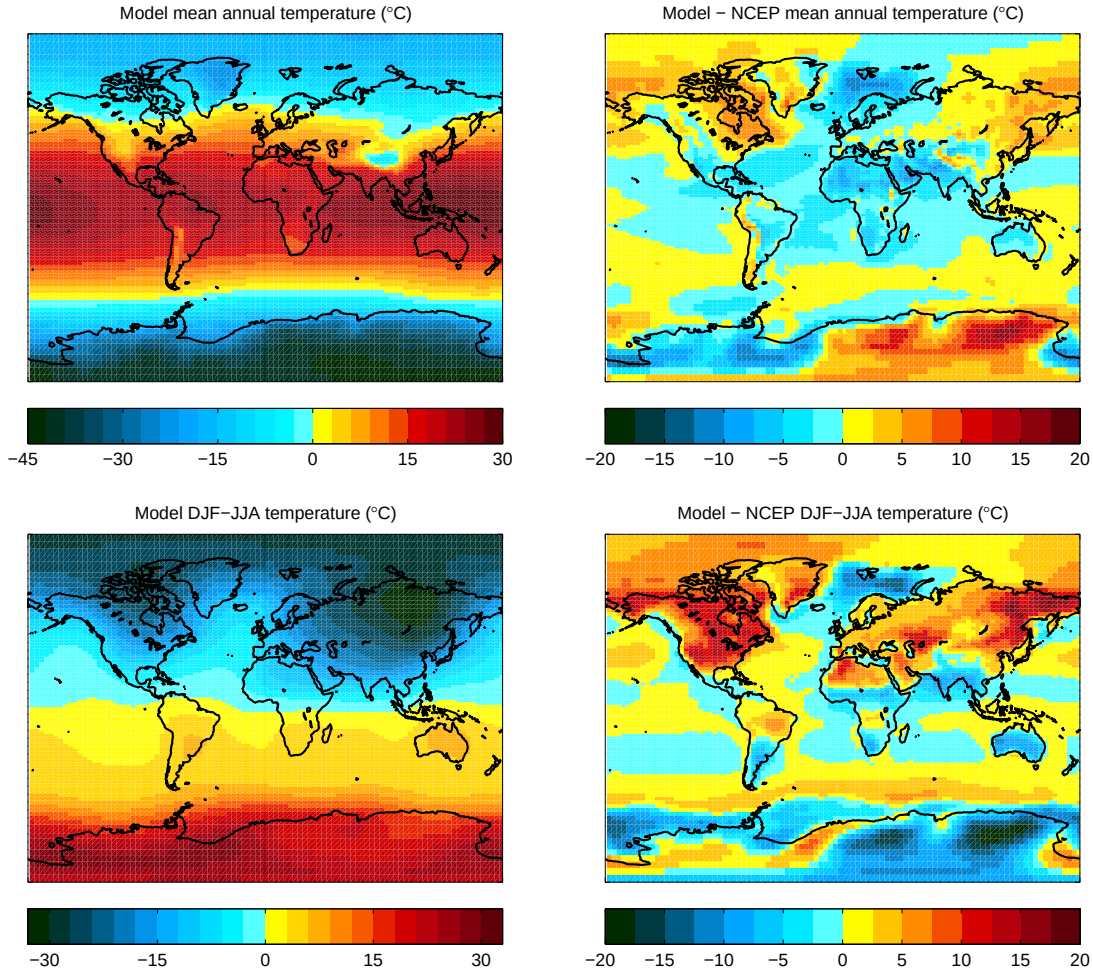

Figure 3.3: Model surface air temperature climatology. Temperature (°C) in the annual mean UVic model pre-industrial simulation (top left), the difference between the model and NCEP reanalysis annual means (top right), seasonal variation in the UVic model (DJF-JJA) (bottom left), and the difference in seasonality between the model and NCEP reanalysis DJF-JJA.

The annual average temperature in the model closely resembles that of NCEP (Figure 3.3). The simulated global annual mean temperature (area-weighted) is 13.28°C, and the equivalent NCEP value is 13.81°C (using NCEP data interpolated to the UVic model grid spacing). Eastern Antarctica, northeastern North America, and northeastern Asia are warmer in the model relative to observations, with the largest discrepancy in Eastern Antarctica, where the simulated annual mean value temperature is 16.66°C warmer than NCEP. The largest negative discrepancy is located in

Western Antarctica, where modelled annual mean temperature is 13.42°C cooler than NCEP. The seasonal difference in temperature (DJF-JJA) is reduced in the model relative to NCEP (Figure 3.3, bottom right). The largest model-NCEP seasonality anomalies are located over land (especially over Northern Hemisphere continents and Eastern Antarctica, with maximum anomalies of −19.36°C and +18.25°C in Eastern Antarctica and Northeastern Asia, respectively), while most of the global ocean exhibits only small differences in seasonality. The model-NCEP seasonality difference may possibly be enhanced over land due to the neglect of vertical atmospheric processes in the model, which is likely to propagate greater error over land (since topography may induce complex atmospheric responses), and due to propagation of model errors in continental soil moisture and moisture fluxes.

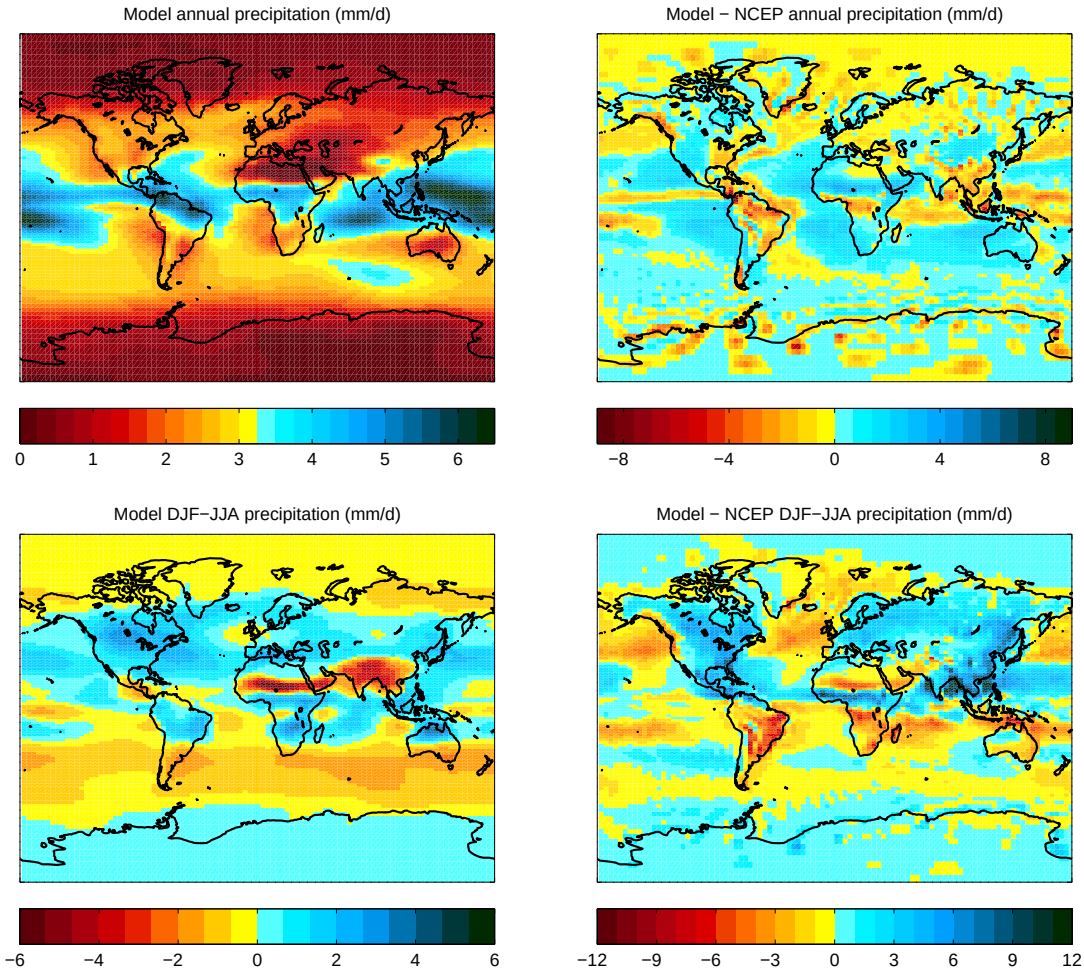

Figure 3.4: Model precipitation climatology. Precipitation (mm/day) in the annual mean UVic model pre-industrial simulation (top left), the difference between the model and NCEP reanalysis annual means (top right), seasonal variation in the UVic model (DJF-JJA) (bottom left), and the difference in seasonality between the model and NCEP reanalysis DJF-JJA.

With respect to precipitation, the model reproduces the global pattern of observed annual precipitation, and the model global mean precipitation rate is close to the observed value (respectively, 2.89 and 2.74 mm day^{-1}). The highest observed precipitation rates in the annual mean are underestimated by the model, such as in Amazonia (Figure 3.4), a feature common across models. Differences in seasonality in precipitation (DJF-JJA) between the model and NCEP are most pronounced over southern and eastern Asia, eastern North America, Central America, and central

Africa. The differences in precipitation seasonality are larger than model estimates at some locations.

Below the modelled distribution of oxygen isotopes in moisture fluxes and seawater are assessed and the modelled isotope patterns are compared to observations.

3.4 Results: Isotopes in preindustrial precipitation

Dansgaard (1964) described a set of isotope effects relating the oxygen isotopic content in precipitation ($\delta^{18}O_{precip}$) to factors including precipitation amount, latitude, surface air temperature, distance from the coast, and altitude. These observed relationships are all produced by the total amount of moisture lost from an air mass (known as rain-out) as it travels away from its moisture source (Rozanski et al., 1993). The degree to which the UVic model can capture these observed patterns in $\delta^{18}O_{precip}$ is a function of the accuracy of the modelled temperature, evaporation, and precipitation fields, as well as the representation of moisture transport. As shown in Figure 3.5 (top panel), model annual zonal mean moisture flux quantities (here, precipitation, evaporation, and E-P, the difference between evaporation and precipitation) all fall within one standard deviation of NCEP annual mean values at all latitudes.

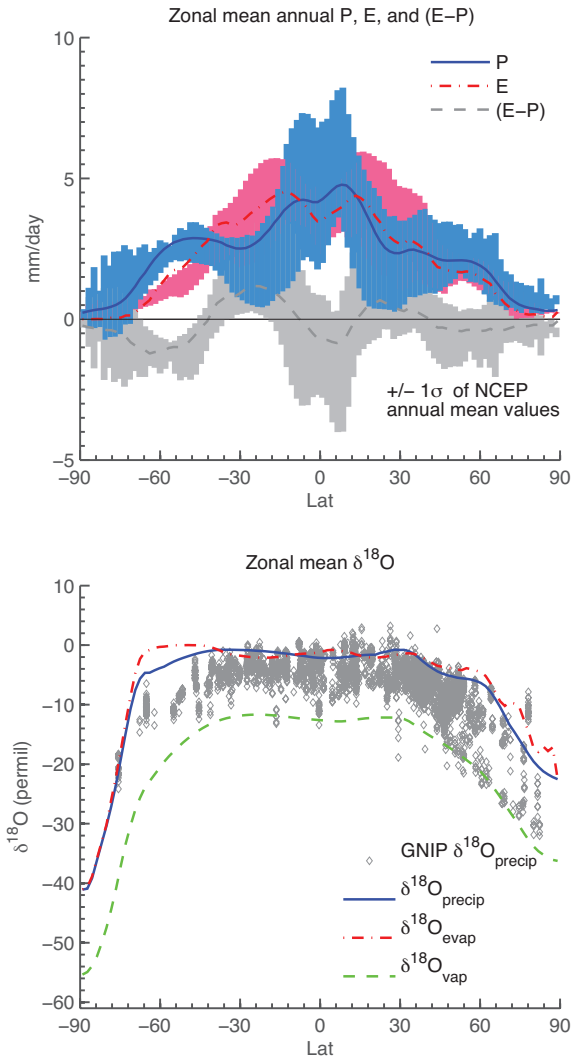

Figure 3.5: Zonal mean fluxes of moisture and isotopes. Zonal annual mean precipitation (solid blue line), evaporation (red dash-dot line), and E-P (dark gray dashed line) in the UVic model, superimposed upon the range of the NCEP zonal annual mean values $\pm 1\sigma$ observed in precipitation (blue bars), evaporation as calculated from NCEP latent heat fluxes (pink bars), and E-P (light gray bars) (top), and zonal annual mean δ^{18}O in precipitation (blue solid line), evaporation (red dash-dot) and atmospheric water vapour (green dash) (bottom) in the model, superimposed upon all available annual mean precipitation δ^{18}O observations in GNIP data (gray diamonds), separated into 1/4 degree latitude bins. NCEP reanalysis data are from Kalnay et al. (1996); GNIP δ^{18}O data are provided by IAEA/WMO (2006). Figure based on Fig. 12 in Lee et al. (2007) and Fig. 1 in Zhou et al. (2008).

Observations of isotopes in precipitation have been collected at several hundred stations since the 1960's, forming the Global Network of Isotopes in Precipitation (GNIP) (IAEA/WMO, 2006). To compare the model against GNIP observations, all GNIP stations for which the weighted annual average of oxygen-18 and surface air temperature are available for individual years (between 1961 and 2001) are selected (369 stations). The UVic model grid cell located nearest each GNIP station was determined, and the annual mean isotope content and surface air temperature from that grid location is sampled from the model.

While the model zonal mean isotopic content in precipitation falls within the range of the GNIP long term mean δ^{18}O values at most latitudes (with the exception of the latitude band -30°S to -70°S) (Figure 3.5, bottom panel), the zonal mean $\delta^{18}O_{precip}$ is more enriched than GNIP observations on average. This model enrichment may be explained by overly enriched vapour δ^{18}O ($\delta^{18}O_{vap}$) where condensation forms in the atmospheric model: model condensation forms from the bulk (well-mixed) atmospheric $\delta^{18}O_{vap}$. The model zonal mean $\delta^{18}O_{vap}$ is quite similar to the NCAR CAM2 AGCM surface (lowest) layer of $\delta^{18}O_{vap}$ (see their Figure 12b in Lee et al. (2007)). However, in an AGCM condensation may form aloft (in one of > 20 vertical atmospheric layers), and $\delta^{18}O_{vap}$ decreases with height. The latitude band -30°S to -70°S corresponds to the latitude of least land surface. The large ocean area may increase the relative component of local oceanic evaporation contributing to $\delta^{18}O_{vap}$, and can decrease the effect of reduced $H_2^{18}O$ diffusivity (which is a function of elevation, see Figure 3.1) in this region. The model $\delta^{18}O_{precip}$ globally averaged value of -7.5‰ is within the range of values reported from AGCMs (-6 to -7.5‰, see Table 3.2).

Table 3.2: Global general circulation and intermediate complexity models with stable water isotopes. If it was reported, the global mean $\delta^{18}O_{precip}$ value is given (NA if isotopes are not explicitly modelled in atmospheric precipitation).

Models	**Reference**	**Global mean $\delta^{18}O_{precip}$**
Atmospheric GCMS		
ECHAM3	Hoffmann et al. (1998)	(N. Atl. vapour −12‰)
ECHAM4	Werner et al. (2001)	
ECHAM5	Werner et al. (2011)	
GENESIS	Mathieu et al. (2002)	
GISS	Jouzel et al. (1987b)	
ICM	Yoshimura et al. (2003)	
LMD	Joussaume et al. (1984)	
LMDZ4	Risi et al. (2010)	−7.56‰
MUGCM	Noone and Simmonds (2002)	
NCAR CAM2	Lee et al. (2007)	
NCAR CAM3	Noone and Sturm (2010)	
ECPC GSM	Yoshimura et al. (2008)	−6.5 to −7.0‰
Ocean GCMs		
CCM3	Delaygue et al. (2000)	NA
GISS	Schmidt (1998)	NA
AOGCMs		
GENESIS-MOM	Zhou et al. (2008)	−7.1‰
GISS ModelE	Schmidt et al. (2007)	−6.0‰ (vapour −13.0‰)
HadCM3	Tindall et al. (2009)	
EMICs		
CLIMBER-2	Roche et al. (2004b)	NA
GENIE-1	Marsh et al. (2006)	NA
UVic ESCM	This work	−7.5‰

LMDZ4 global $\delta^{18}O$ mean value is for AMIP simulation 1979 annual mean (Risi et al., 2010). Yoshimura et al. (2008) provide a range of monthly global mean $\delta^{18}O_{precip}$ for ECPC GSM.

Figure 3.6 maps both the modelled mean annual $\delta^{18}O_{precip}$ and the long-term mean values at each GNIP station supplemented with Antarctic surface snow isotopic

observations from Masson-Delmotte et al. (2008), interpolated to a UVic model grid to enable comparison. Consistent with the observed relationship between precipitation isotopic content and latitude (the latitude effect, first described by Dansgaard (1964)), $\delta^{18}O_{precip}$ decreases poleward in the model, reaching a minimum value of -47.1‰ in central Antarctica (in the Northern Hemisphere, a minimum of -26.2‰ is achieved in northern Greenland). A local enrichment ($+4.4$‰) occurs in southeast Asia on the lee side of the Himalaya. This feature is not found in the observations, and likely results from the elevation-dependent modification of $H_2^{18}O$ diffusivity described in Section 3.2.4. While the model $\delta^{18}O_{precip}$ exhibits close to observed latitudinal patterns, regional discrepancies between modelled and observed are evident. For example, the regions of northern North America, northern Europe and southern South America are too enriched in the model. Otherwise, the model is generally consistent with observations throughout Asia (not including the aforementioned enrichment east of the Himalayas), Australia, Africa, and Antarctica. The root mean square error (RMSE) provides a quantitative measure of the differences between the modelled annual average $\delta^{18}O_{precip}$ and the GNIP long term mean values (interpolated to the UVic model grid), which for individual stations ranges from a minimum of 0.0‰ to a maximum of 18.2‰, with an expected value of 4.1‰.

For mean annual temperatures below 15°C (excluding extreme outliers below -21°C), the spatial relationship between temperature and $\delta^{18}O_{precip}$ is very similar in slope between model (sampled at GNIP station locations) and GNIP data, shown in Figure 3.7. The model slope of 0.51 is very close to the slope of 0.49 for the data, with r^2 values of 0.77 and 0.65, respectively. Plotted values include all years of GNIP station data with annual average surface temperature and weighted $\delta^{18}O_{precip}$ (N = 3085), and mean annual surface air temperature and $\delta^{18}O_{precip}$ from the UVic model at GNIP station locations (N = 369).

3.4.1 Discussion of model $\delta^{18}O_{precip}$

In order to explain model-data discrepancies in $\delta^{18}O$ of precipitation (and, by extension, seawater (Section 3.5)), here the impacts of several parameterizations in the atmospheric model on condensation and moisture transport are considered as they relate to isotopes. These parameterizations are necessary to achieve the desired model computational efficiency and speed, but require the simplification of several atmospheric processes. First, condensation forms in the model when relative humidity

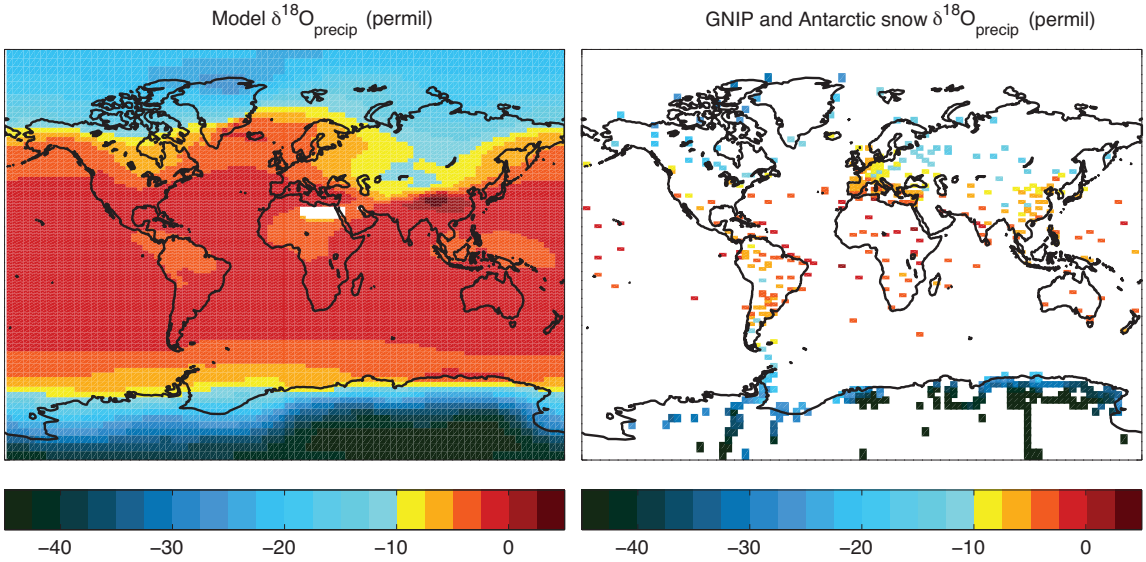

Figure 3.6: Annual average δ^{18}O in precipitation. Annual average δ^{18}O in present-day precipitation for the UVic model (left) and observations from the Global Network of Isotopes in Precipitation (IAEA/WMO, 2006) (long term time averages shown) and Antarctic surface snow (Masson-Delmotte et al., 2008) datasets, interpolated to a UVic model grid (right). Observational values are plotted at a slightly larger size than the actual gridcell (130%) for improved visualization.

exceeds 85%. This precipitation is instantaneously removed from the atmospheric column, and is subsequently added to the surface moisture flux. In effect, partial re-evaporation of falling precipitation is neglected. Without partial re-evaporation (which adds depleted vapour), local precipitation is more depleted, while the remaining vapour is more enriched. The overall result of more enriched remaining vapour would tend to dampen the "latitude effect" in the model.

Second, condensation occurs in the model at surface air temperatures (adjusted for elevation over land by a lapse rate). Since condensation forms at (warmer) surface temperatures as opposed to (cooler temperatures) aloft, this yields a smaller effective fractionation. Smaller fractionation during condensation produces slightly more depleted local precipitation and more enriched remaining atmospheric vapour (as in the case of neglecting re-evaporation).

Third, model precipitation derives from a vertically-integrated atmospheric column, such that the atmospheric moisture is essentially well-mixed with respect to isotopes. This assumption precludes a description of vertical motion of air masses (and their associated condensation) or vertical differentiation of isotopes. In contrast,

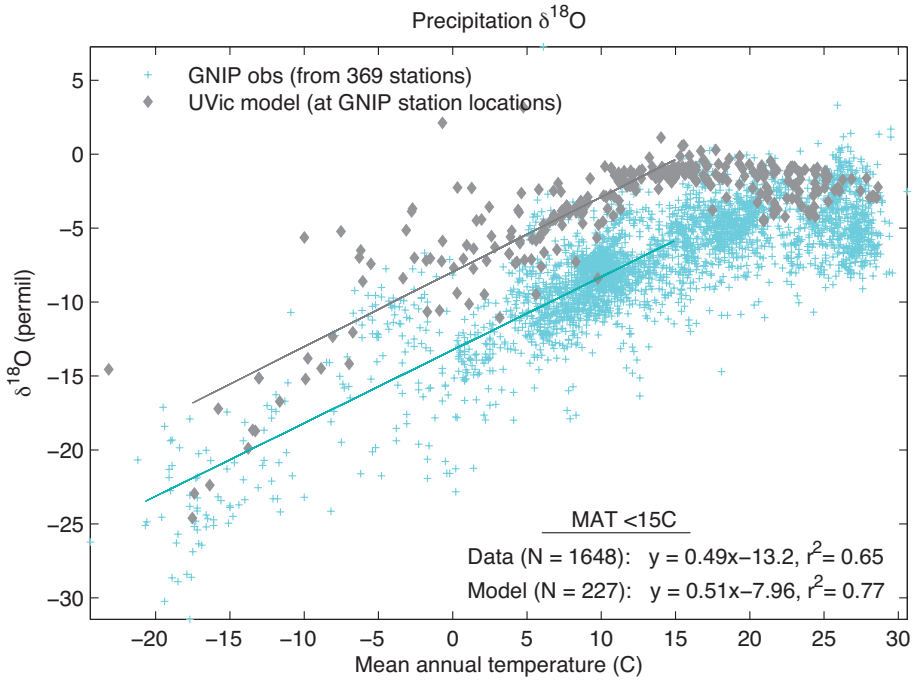

Figure 3.7: Temperature $-$ $\delta^{18}O$ spatial relationship. Mean annual temperature and $\delta^{18}O$ in precipitation are plotted for observations at GNIP stations for each available year (blue crosses, N = 3085) and the UVic model at GNIP station locations (gray diamonds, N = 369). The linear fit and trend line for GNIP and model values with mean annual temperature less than 15°C (excluding outliers below −21°C) are indicated (teal line, N = 1648, and gray line, N = 227, respectively).

condensation forms in the earth's atmosphere at variable height, and the atmospheric column is characterized by variable $\delta^{18}O$ and temperature (typically, with more isotopically depleted and colder values aloft) (for example, see discussion in Lee et al. (2007), and their Figure 15). The result is that the vapour from which condensation forms (the well-mixed atmospheric column) is likely to be more enriched in the model (than vapour at several thousand meters altitude, for example), and in turn, precipitation would be more enriched. However, isotopes in precipitation are generally observed to be in equilibrium with the vapour in the lowest layer of the atmosphere, which may partially account for the model's capturing of the observed large scale patterns in $\delta^{18}O_{precip}$.

The above processes may create opposing isotopic effects, with local precipitation becoming more enriched due to a more enriched bulk vapour, and/or less enriched based on both the smaller fractionation factor due to warmer surface temperature

and the neglect of re-evaporation. The net effect of neglecting these processes may be to reduce variability in model $\delta^{18}O_{precip}$ in regions where vertical moisture transport, re-evaporation of falling droplets and high-altitude condensation are important. By extension, reduced latitude and continental effects may result, due to the integration of these effects for atmospheric moisture transported long distances. As seawater surface $\delta^{18}O$ variability mainly depends on the variability of $\delta^{18}O$ in moisture fluxes at the sea surface (and river inputs are essentially a signal of average $\delta^{18}O_{precip}$ over the drainage basin), $\delta^{18}O_{sw}$ may be reduced in variability by these processes as well (see Section 3.5).

3.5 Results: Isotopes in preindustrial seawater

The distribution of oxygen isotopes at the ocean model surface reflects the isotopic fluxes occurring during evaporation from the sea surface, precipitation, additions of river runoff, and sea ice melt and brine production, in addition to the effects of transport and mixing of water masses. The model δ^{18}O at the sea surface (top 50 m) is compared with the interpolated observations (averaged over the top 50 m) (LeGrande and Schmidt, 2006) based on the GISS seawater O18 dataset (Schmidt et al., 1999) in Figure 3.8. Because maximum variability is located nearest the sea surface, and the upper layer of the UVic ocean model is 50 m deep, the model-data comparison of the top 50 m is appropriate in assessing model variability. The oxygen isotope composition of seawater ($\delta^{18}O_{sw}$) in the model displays the same broad features found in the observations. Surface water is more depleted at high latitudes than in low latitudes. Net evaporative regions (where $E - P > 0$) contain more positive $\delta^{18}O_{sw}$ values. The Atlantic, for example, contains more enriched $\delta^{18}O_{sw}$ than the Pacific. These observed large-scale patterns suggest the model produces a reasonable first-order distribution of moisture fluxes. A model-data discrepancy, however, is apparent in the absolute range of surface $\delta^{18}O_{sw}$ values, which is narrower in the model than in observations. This reduced variability in surface $\delta^{18}O_{sw}$ may result from the treatment of moisture transport and condensation in the atmospheric model, which affect seawater via precipitation and river runoff.

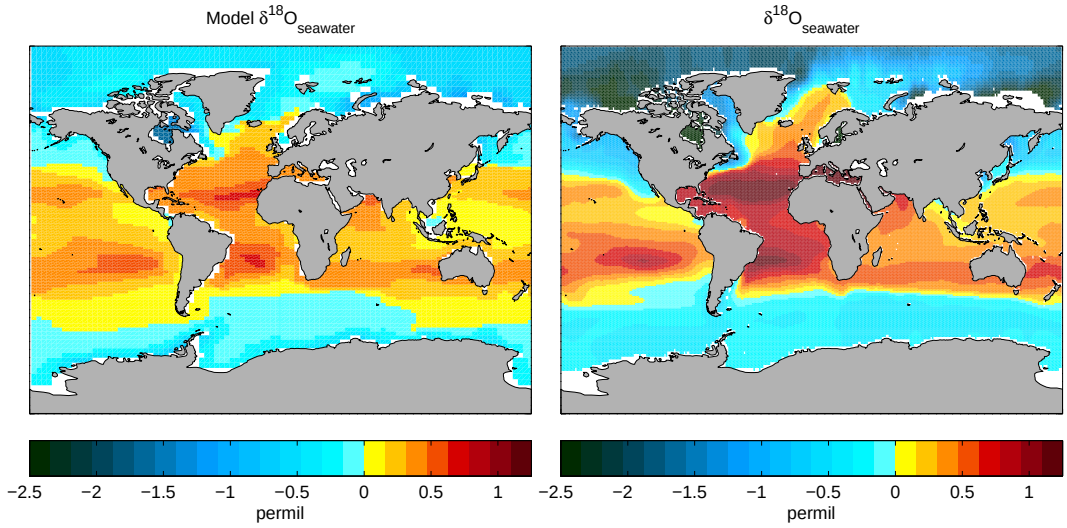

Figure 3.8: Sea surface δ^{18}O. Surface seawater δ^{18}O in the UVic model (annual mean of surface ocean model level (depth 50 m)) (left), and the gridded δ^{18}O seawater dataset (LeGrande and Schmidt, 2006) (averaged over the top 50 m) (right).

Since precipitation and snowmelt are returned immediately to the ocean (once soil moisture is saturated) via river runoff, it is useful to compare observations of river runoff δ^{18}O ($\delta^{18}O_r$) with model values. Yi et al. (2012) report annual discharge and weighted mean $\delta^{18}O_r$ data collected between 2003 and 2006 from six major Arctic rivers as part of the Pan-Arctic River Transport of Nutrients, Organic Matter and Suspended Sediments (PARTNERS) project. The most depleted runoff originates in the Kolyma River (−22.18‰), the least depleted in the Ob River (−14.85‰), and the annual weighted mean $\delta^{18}O_r$ value for all six rivers (Mackenzie, Kolyma, Lena, Yenlsey, Ob, and Yukon) is −18.72‰. In the model, river discharge to the Arctic ranges from −7.2‰ to −11.0‰, and only runoff from the (non-physical) island at the pole is as depleted as observations (−20.9‰). The mean annual Antarctic discharge in the model is −16.8‰ (Figure 3.9).

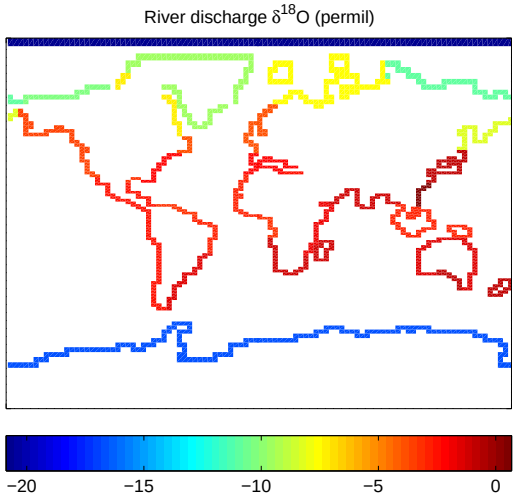

Figure 3.9: Annual mean δ^{18}O in model river discharge (permil). River runoff from 32 river basins is discharged at coastal points (described in Weaver et al. (2001)).

3.5.1 Salinity-$\delta^{18}O_{sw}$ relationships

Both seawater δ^{18}O and salinity are shifted in the same direction by processes occurring at the ocean surface (with the noted exception of sea ice growth and melt (e.g., Strain and Tan, 2003)), resulting in a linear relationship between the two quantities. For example, evaporation (precipitation) typically increases (decreases) both salinity and $\delta^{18}O_{sw}$. The slope of the best fit line is compared for the salinity-$\delta^{18}O_{sw}$ data sampled from the model to that sampled from the same region in the observations.

To best describe water mass characteristics, it is standard practice to separately assess the properties of upper water (< 400 m), intermediate water ($400 - 2500$ m), and deep water (> 2500 m). To characterize the upper water column, surface waters are defined as the top 400 m, and in the model the top four ocean levels, which corresponds to a depth of 380 m, within the salinity range of 28 to 38. Observations from the same coordinate and depth level are time-averaged. The model salinity and $\delta^{18}O_{sw}$ are sampled from every ocean grid cell, resulting in a larger sample size from the model relative to the observations.

Tropical surface waters (between 20°N and 20°S) have very similar model and observed salinity-$\delta^{18}O_{sw}$ relationships (Figure 3.10). In the tropical Atlantic, a model slope (in salinity-δ^{18}O space) of 0.19 ($r^2 = 0.74$) is found, with an observed slope of

0.18 ($r^2 = 0.50$). In the tropical Pacific, the salinity-δ^{18}O slopes are 0.23 ($r^2 = 0.96$) in the model and 0.24 ($r^2 = 0.77$) in the observations. Model-data similarity decreases slightly in tropical Indian Ocean surface waters which have a salinity-δ^{18}O slope of 0.16 ($r^2 = 0.55$) in the model and 0.24 ($r^2 = 0.57$) in the data. In comparison, the extratropical surface water salinity-δ^{18}O relationship is weaker in the model than in the observations. The model slope of 0.32 ($r^2 = 0.78$) is significantly less than the observed slope of 0.57 ($r^2 = 0.68$). Similarly, the surface waters of the global ocean have a slope of 0.32 ($r^2 = 0.79$) in the model, which is less than the slope of 0.55 ($r^2 = 0.68$) observed in the data (Figure 3.10).

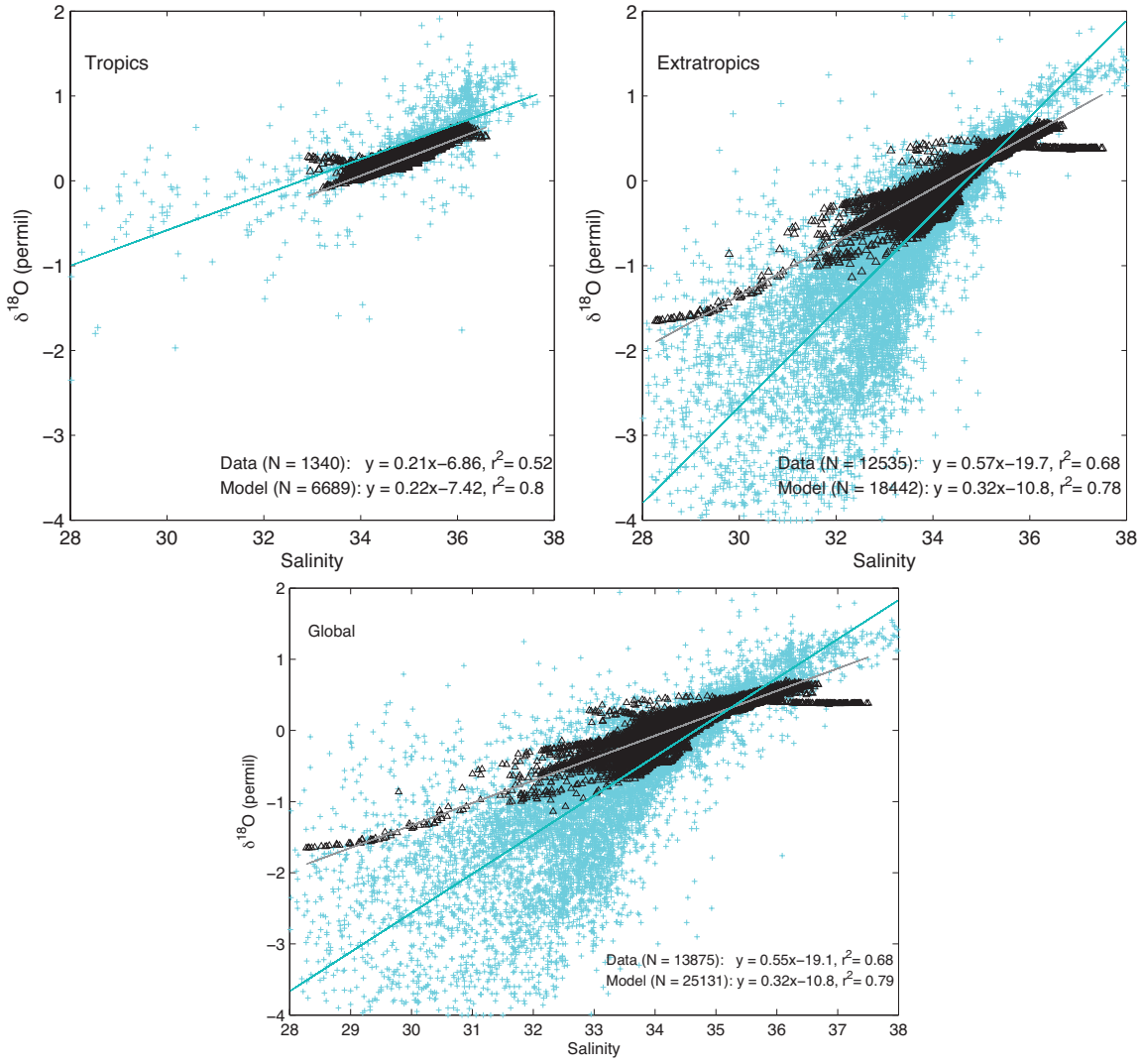

Figure 3.10: Salinity $-$ δ^{18}O spatial relationships in seawater. Surface water salinity-δ^{18}O relationships found in the modelled preindustrial annual mean (black diamonds) and the Seawater O18 dataset (Schmidt et al., 1999) (blue crosses) in the tropics (20°S-20°N) (top left), extratropics ($>$ 20° N and S) (top right), and in the global surface waters (bottom). The linear fit to the observations (blue line) and model values (gray line) is indicated in the lower right.

Intermediate waters (400 to 2500 m) have a global mean salinity and $\delta^{18}O_{sw}$ of 34.7 psu and 0.10‰ in the model, indistinguishable from the GISS seawater O18 dataset values of 34.9 psu and 0.10‰ for intermediate water (n $>$ 5400). The salinity-$\delta^{18}O_{sw}$ spatial relationship in global intermediate waters is slightly reduced in the model than

in the data (slope of 0.23 ($r^2 = 0.52$) vs 0.39 ($r^2 = 0.76$), respectively). In the model, as in observations, deep water (> 2500 m) is more saline and more enriched in $H_2^{18}O$ in the North Atlantic than in the other ocean basins. While observations reveal the global deep ocean to be on average 0.3 to 0.45‰ more negative than deep water in the North Atlantic, the difference in the model is less dramatic, approximately 0.1‰.

3.6 Last Glacial Maximum Equilibrium Simulation

3.6.1 Set-up and initialization

A 5 kyr simulation was performed using constant radiative forcing conditions for the Last Glacial Maximum (LGM), including an orbital configuration corresponding to 21 kyr BP, atmospheric pCO_2 of 189.65 ppm, and increased elevations where ice had accumulated on land (following the Peltier (1994) ICE4G reconstruction). The LGM simulation employs the same NCEP wind forcing used for the preindustrial, although the superimposed dynamic wind feedback component (a function of surface temperature gradients) is different. Atmospheric moisture diffusivity is unchanged from the preindustrial. Additionally, LGM surface albedo is increased in grid cell locations corresponding to the expanded prescribed ice sheet cover and the increased snow cover (both with albedo of 0.80). The model was initialized using a previous LGM simulation such that the ocean and climate physical parameters were already at quasi-equilibrium values.

In order to initialize the water isotope reservoirs, recent estimates of the difference between LGM and present day values were considered. By applying a pore water diffusion model to a deep western Pacific sediment core, Schrag et al. (1996) estimated a 1.0 ± 0.25‰ LGM seawater enrichment, relative to present day. Duplessy et al. (2002) considered the full range of LGM sea level estimates ($120 - 140$ m), and with the same methods (i.e., Schrag et al., 1996; Adkins and Schrag, 2001) concluded that the LGM ocean was enriched relative to present day by $0.95 - 1.08$‰. Duplessy et al. (2002) further assessed all other robust methods for estimating the LGM seawater isotopic shift, and determined a best estimate of 1.05 ± 0.20‰. Therefore the LGM ocean is initialized to 1.1‰ above the pre-industrial seawater initial value of 0.1‰. Ice on land was set to -30‰, atmospheric water vapour to -10‰, and other water reservoirs (sea ice, snow lying on land and sea ice, and soil moisture) to 0‰.

3.6.2 LGM Climatology

The modelled LGM climatological patterns (e.g. surface air temperatures and ocean temperatures) are very similar to the LGM simulation described by Weaver et al. (2001). As shown in Figure 3.11, the LGM global mean temperature is cooler by 4.08°C, and global mean precipitation is decreased by 0.19 mm/day, relative to the preindustrial (PI). Precipitation is slightly enhanced only in a narrow mid-latitude band in each hemisphere. Climatological mean values for the LGM and PI simulations as well as the LGM-PI differences are presented in Table 3.3.

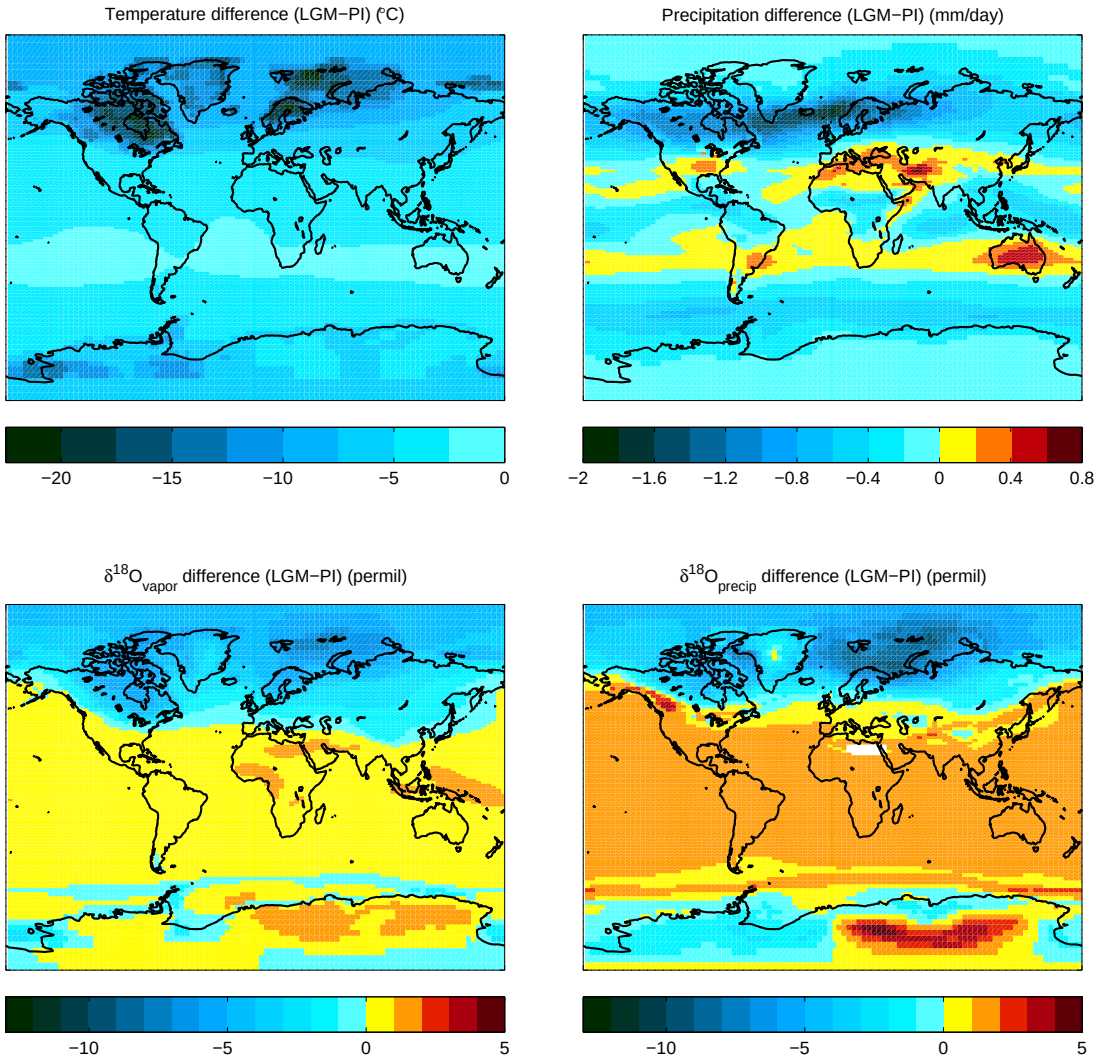

Figure 3.11: Model LGM-PI climatological and isotopic differences. Annual mean difference between LGM and PI for surface air temperature (top left), precipitation (top right), δ^{18}O in atmospheric water vapour (bottom left), and δ^{18}O in precipitation (bottom right).

As in previous LGM simulations in the UVic model, relative to the preindustrial the maximum meridional overturning streamfunction is reduced (14.4 Sv in the LGM compared to preindustrial 21.7 Sv), sea ice cover is expanded (2.5×10^{13} m^2 during LGM compared to a preindustrial annual mean of 2.2×10^{13} m^2), and sea surface temperature is decreased (the largest decrease, > 8°C, is found in the northeast

Table 3.3: Climatological and isotopic annual mean values from the preindustrial (PI) and Last Glacial Maximum (LGM) model equilibrium simulations, the difference between LGM and PI (LGM-PI), and available reference data for comparison. Low and mid-latitudes refer to $0-30°$N, S and $30-60°$N, respectively. Where reference time period not specified, value refers to PI. For LGM-PI data references, see Table 2 in Risi et al. (2010) and Table 2 in Duplessy et al. (2002).

	PI	**LGM**	**LGM-PI**	**Reference**
Global				
Surface air temp. (°C)	13.26	9.18	−4.08	
Surface ocean temp. (°C)	17.86	15.57	−2.29	
Precipitation (mm/day)	2.89	2.70	−0.19	2.74
$\delta^{18}O_{precip}$ (‰)	−7.5	−7.4	0.1	
$\delta^{18}O_{precip}$, marine (‰)	−4.2	−3.9	0.3	
$\delta^{18}\boldsymbol{O}_{precip}$ ***(‰)***				
Greenland				
GRIP ice core	−16.7	−19.5	−2.8	−7
Camp Century ice core	−19.7	−22.9	−3.2	−12.9
Dye 3 ice core	−4.0	−7.5	−3.5	−5.5
Renland ice core	−10.5	−13.6	−3.0	−5
NGRIP ice core	−19.5	−20.7	−1.2	−8
Mid-latitude				
England	−3.8	−3.8	0.0	−1.2
Guliya ice core	−4.6	−3.6	+1.0	−5.4
Dunde ice core	−6.7	−6.2	+0.5	−2
Sanbao and Hulu caves	1.2	2.1	+0.9	+1.5
Low-latitude				
Stampriet aquifer	−1.4	−0.1	+1.3	+1.5
Huascaran ice core	−3.2	−1.9	+1.3	−6.3
Sajama ice core	−3.0	−1.7	+1.2	−5.4
Illimani ice core	−1.1	0.3	+1.4	−6
Botuvera cave	−1.3	−0.1	+1.2	−1.5
Santana cave	−1.5	−0.3	+1.2	−1.5
Rio Grande do Norte cave	−1.7	−0.5	+1.2	−0.5
Salar de Uyuni	−2.4	−1.3	+1.2	−4
Antarctica				
Vostok	−36.5	−32.9	+3.6	−3 to −5
Byrd	−21.4	−23.0	−1.6	−8
Dome C	−28.8	−27.2	+1.6	−5.4
Dome B	−35.6	−32.0	+3.7	−5
Taylor Dome	−36.3	−35.1	+1.2	−3

Atlantic, while the mean tropical SST change is $-2.4°C$) except in the polar oceans where expanded sea ice cover decreases heat loss to the atmosphere (not shown, see Figures $37-39$ in Weaver et al. (2001)).

3.7 Results: Isotopes in LGM precipitation

Changes in the distribution of isotopes in LGM precipitation relative to the preindustrial ($\Delta\delta^{18}O = \delta^{18}O^{LGM}_{precip} - \delta^{18}O^{PI}_{precip}$) may result from changes in the rate, timing (e.g. seasonality), and/or isotopic content of surface moisture fluxes, the relative enrichment of the primary moisture source (the surface ocean), and changes in moisture transport. Temperature change has a direct effect on $\delta^{18}O_{precip}$ in modifying the equilibrium fractionation factor during condensation (with cooler temperatures producing larger fractionation), but otherwise indirectly influences $\delta^{18}O_{precip}$ through its impact on moisture fluxes and transport. The LGM climate exhibits cooler surface temperatures (notably in the Northern Hemisphere), increased subtropical precipitation coupled with decreased precipitation elsewhere (shown in Figure 3.11), and an enriched surface ocean (due to the expanded continental ice). This set of conditions is likely to produce enriched atmospheric vapour and precipitation at low latitudes (a consequence of the enriched source evaporate), and increased rain-out of isotopes in mid- and high-latitudes, or an increased latitude effect (a function of both cooling and the precipitation changes).

Atmospheric water vapour and precipitation are slightly more enriched at low latitudes in the LGM simulation compared to preindustrial (Figure 3.11). A similar slight increase in low latitude $\delta^{18}O_{precip}$ is found in other models (e.g., LMDZ-iso AGCM results shown in Figures 12-13 in Risi et al., 2010). The model is able to capture the LGM depletion in Northern Hemisphere high latitudes, but the magnitude of the depletion is smaller over northern North America than in the LMDZ-iso AGCM. For example, the model maximum decrease in annual mean $\delta^{18}O_{precip}$ is 10.6‰, while in LMDZ-iso LGM precipitation falling in the Hudson Bay region is depleted by more than 15 to 25‰ relative to present day (depending on which LGM SST forcing is applied).

The model LGM-PI depletion in the Southern Hemisphere high latitudes is rather weak (less than 2.5‰), and whereas one of the LMDZ-iso AGCM simulations produces an enrichment near the Antarctic coast (see Figure 13 in Risi et al. (2010)), our model also simulates an enrichment over inland Eastern Antarctica, in contrast

with the depleted LMDZ-iso values. Relative to the preindustrial simulation, eastern Antarctica in the LGM simulation is characterized by only small changes in ice thickness (increases of 100 to 500 m), temperature (see Figure 3.5, top left), and precipitation (see Figure 3.5, top right). Eastern Antarctica contains the highest Southern Hemisphere elevations, generally above 3000 m. It is likely that the model does not produce sufficient successive condensation (rain-out) between the evaporation of (slightly enriched) moisture from the sea surface and the formation of local precipitation, such that the model vapour entering this region is overly enriched.

Model LGM $\delta^{18}O_{precip}$ can be compared to the $\delta^{18}O$ values measured from ice cores and cave deposits formed during the LGM (Table 3.3). Risi et al. (2010) compiled estimates from the most recently available ice core, cave deposit, and aquifer records spanning the LGM (their Table 2). The compilation includes the isotopic content in ice measured in fifteen ice cores from high-latitude (Greenland and Antarctica), mid-latitude (Tibet), and low-latitude (South America) ice cores, and the isotopic content determined at seven mid- and low-latitude cave and aquifer sites. The estimate of LGM $\delta^{18}O_{precip}$ at each site may be characterized by various types of uncertainty, including dating uncertainty as noted by Risi et al. (2010).

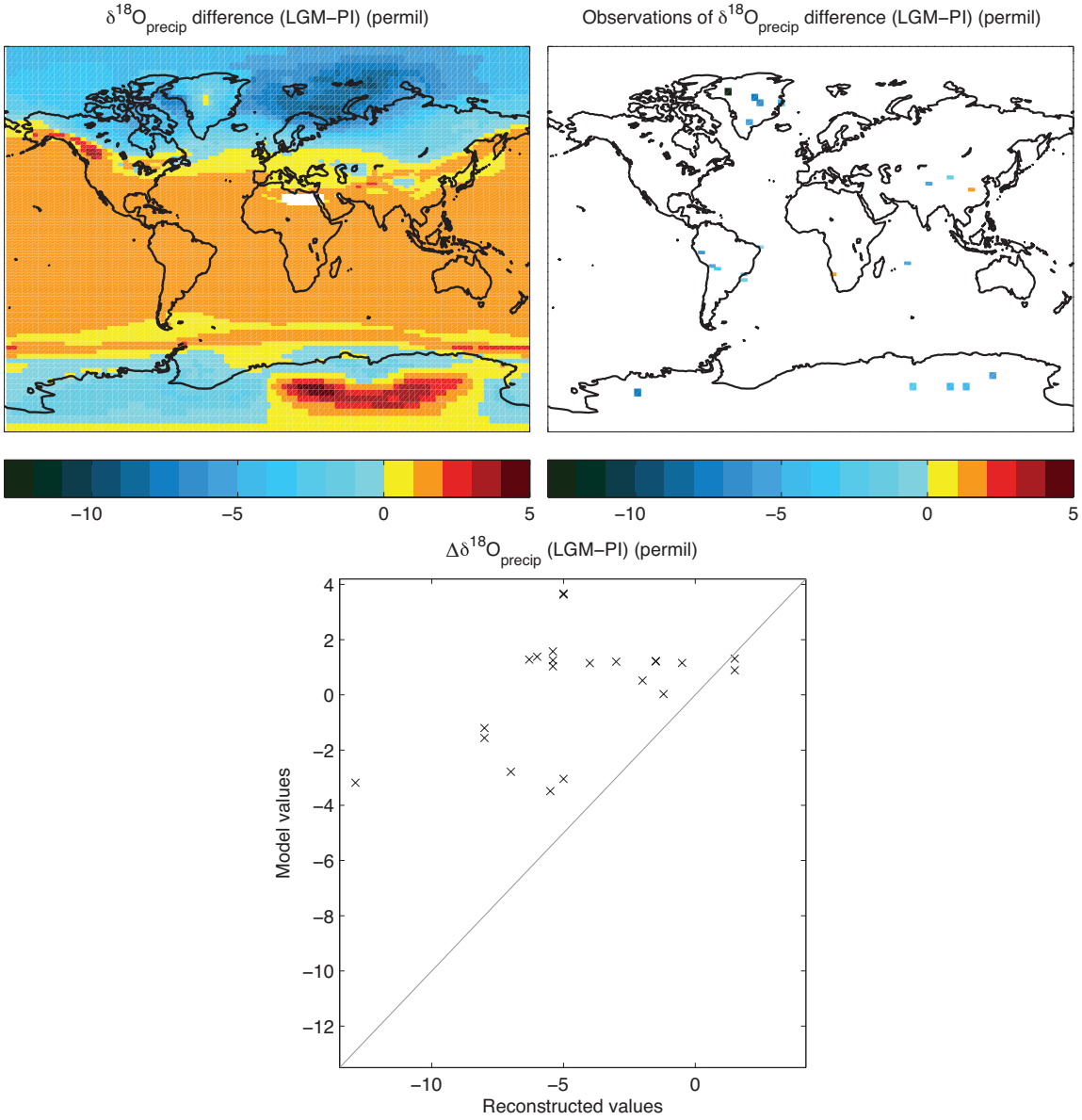

Figure 3.12: Model and reconstructed LGM-PI $\delta^{18}O_{precip}$ differences. Annual mean difference between LGM and PI for $\delta^{18}O$ in precipitation in the model (top left) and the reconstructions, interpolated to a UVic model grid (top right), with a scatter plot of reconstructed vs model values (sampled from the model at the locations of the reconstructed values) (bottom). A 1:1 line is included. Reconstructed values are plotted at a slightly larger size than the actual grid cell (130%) for improved visualization. LGM-PI data is summarized in Table 3.3. Complete references are provided in Table 2 in Duplessy et al. (2002) and Table 2 in Risi et al. (2010).

The model LGM-PI difference in mean annual $\delta^{18}O_{precip}$ indicates that the simulated LGM may not be as depleted relative to preindustrial as the reconstructed values suggest (Figure 3.12). The reconstructed values are interpolated to a UVic model grid to permit direct model-data comparison. By plotting the LGM-PI change in the model mean annual $\delta^{18}O_{precip}$ (sampled at the locations of the reconstructed values) against the reconstructed values with a 1:1 line, it is clear that the model is not as depleted in the LGM relative to preindustrial. The model-data discrepancy is largest in northwestern Greenland and eastern Antarctica, and small at sites in Southern Africa, South-Eastern Asia, Southern Greenland, England and along the east coast of South America. The likeliest explanation for the discrepancy in Eastern Antarctica is insufficient rain-out in the model before precipitation forms, due to the proximity of the ocean and extreme topography where vertical processes are important (as noted above), but there is no clear single explanation for the misfit in northwestern Greenland.

To better understand the processes affecting the LGM-PI shift in $\delta^{18}O_{precip}$, one would ideally isolate portions of the forcing (including changes in temperature, precipitation, evaporation, atmospheric moisture transport, and the isotopic content of seawater). Due to the constraint of conserving heat and moisture in the coupled model, partitioning the effects due to LGM-PI changes in temperature and moisture fluxes directly is not an option, since these are not independent. However, it is possible to assess the role of change in fractionation during condensation as a function of the LGM-PI temperature change, as well as that of an enriched LGM ocean.

Fractionation during condensation is a function of temperature, as described in Table 3.1 (α). By imposing a global field of preindustrial surface air temperatures (specifically, the annual cycle using 5-day averages) within the LGM climate at equilibrium, the fractionation factor using the forced PI temperature (α^*) is determined, as well as the resulting isotopic content of precipitation, which is saved offline ($\delta^{18}O_{precip^*}$). The difference in $\delta^{18}O_{precip}$ and $\delta^{18}O_{precip^*}$ gives the effect of the local temperature change on fractionation during condensation, shown in Figure 3.13 (top left). With the aim of identifying the component of the LGM-PI shift in $\delta^{18}O_{precip}$ due to ocean enrichment, a second LGM simulation is performed in which seawater is initialized to the preindustrial value (0.1 permil), and the model is integrated 5 kyr to equilibrium. The difference in $\delta^{18}O_{precip}$ between the enriched and unenriched seawater LGM simulations is plotted in Figure 3.13 (top right).

Adding the effects of changes due to temperature-dependent fractionation in con-

densation and seawater enrichment produces a combined effect (not shown), which when removed from the observed LGM-PI $\delta^{18}O_{precip}$ signal, reveals the role of changes due to all other processes (bottom panel of Figure 3.13). A significant portion of the low to mid-latitude signal is explained by the combined effect, while clearly model changes in other factors (i.e. temperature, precipitation, transport, etc.) dominate the high-latitude LGM-PI shift in $\delta^{18}O_{precip}$.

3.8 Results: Isotopes in LGM seawater

Changes in the distribution of oxygen isotopes in LGM seawater relative to the preindustrial ($\Delta\delta^{18}O = \delta^{18}O_{sw}^{LGM} - \delta^{18}O_{sw}^{PI}$) may occur due to changes in the amount of (relatively depleted) ice stored on land, ocean-atmosphere moisture exchanges, river inputs, sea ice production, and ocean circulation. As for changes in $\delta^{18}O_{precip}$ (described above), changes in surface temperatures may result in both direct and indirect effects on $\delta^{18}O_{sw}$. Temperature changes cause changes in the (temperature-dependent) fractionation during evaporation from the sea surface (a direct effect), and also may cause a shift in the amount, timing, and/or geographical pattern of moisture fluxes at the sea surface (an indirect effect). The total LGM-PI shift in $\delta^{18}O_{sw}$ is plotted in Figure 3.14 for surface waters (depth-weighted average from 0 to 380 m, corresponding to the uppermost four ocean model levels) and a layer of intermediate water located at 980 to 1240 m depth in the model.

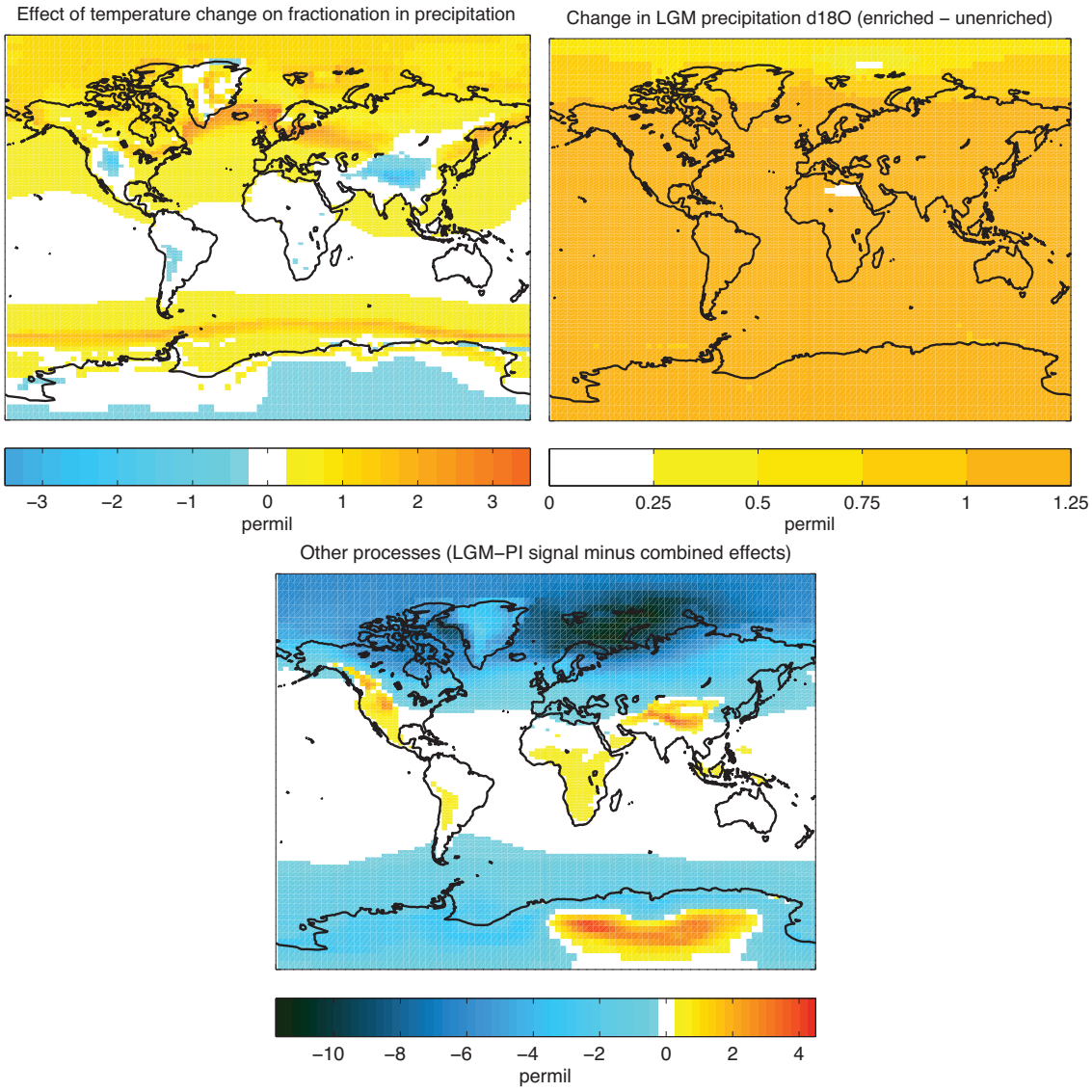

Figure 3.13: Contributions to LGM-PI annual difference in model precipitation isotopic content (permil). Component of LGM-PI shift in $\delta^{18}O_{precip}$ due to the temperature-dependent equilibrium fractionation factor in condensation (top left), due to the enrichment of the glacial ocean (by 1.1 permil) (top right), and due to other processes (bottom), which is the combined effect removed from the LGM-PI shift.

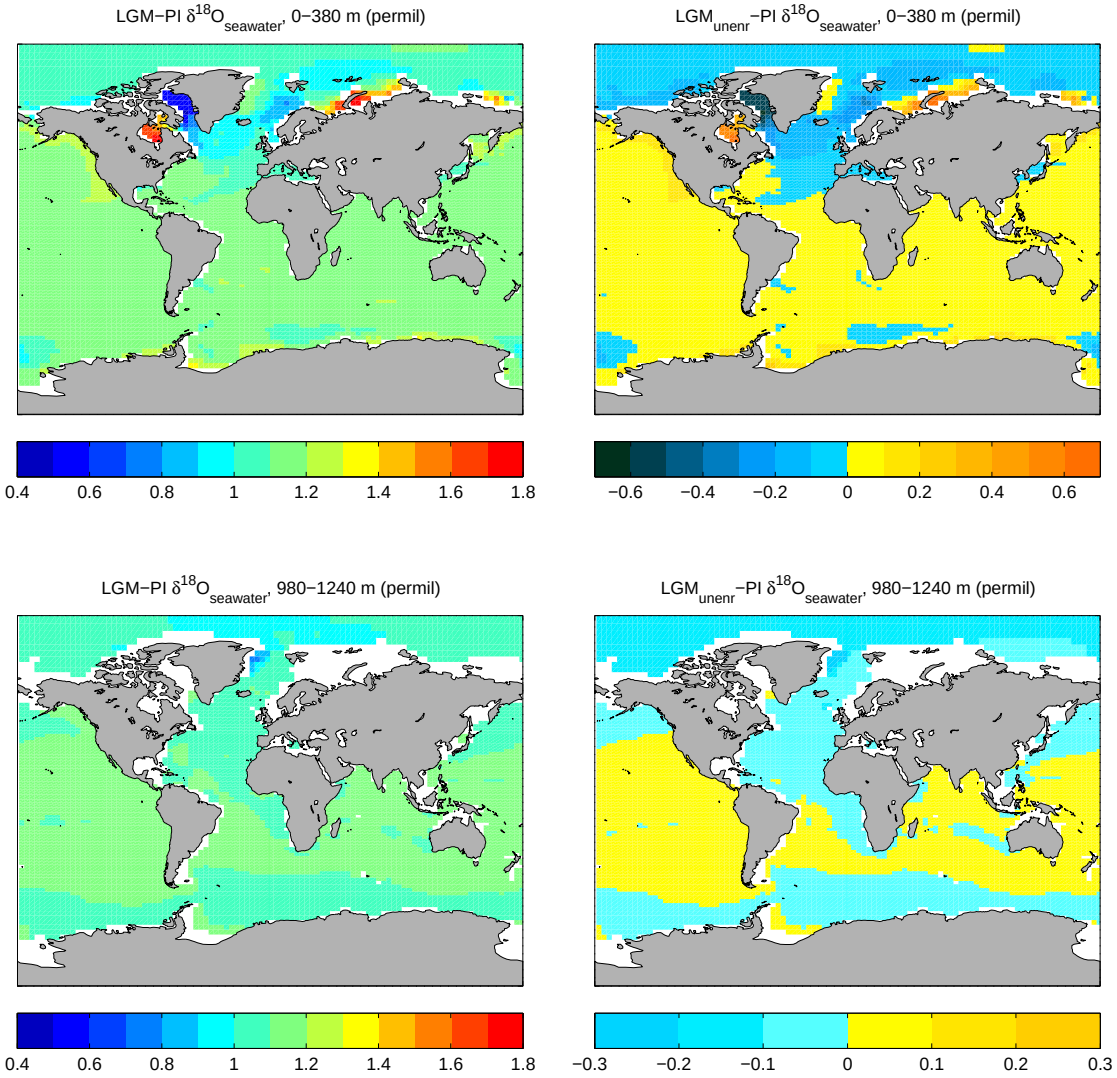

Figure 3.14: LGM-PI differences in seawater δ^{18}O (permil) in the ocean model. Total annual mean difference between modelled LGM and PI $\delta^{18}O_{sw}$ (includes ocean enrichment due to increased continental ice volume) (left), and with the component due to ocean enrichment removed (right) for surface waters (weighted average value from 0 to 380 m) (top), and for a mid-intermediate water layer (980 to 1240 m) (bottom).

As described in Section 3.7, a second LGM simulation in which seawater is initialized to the preindustrial value (0.1 permil) is integrated 5 kyr to equilibrium, to represent a LGM state with an unenriched ocean (LGM_{unenr}). While the difference between LGM and PI $\delta^{18}O_{sw}$ represents the full expected change in $\delta^{18}O_{sw}$ due to

both climatic forcing and the build up of continental ice (Figure 3.14, left), the difference between LGM_{unenr} and PI displays the same signal, but without the influence of changes in continental ice volume (Figure 3.14, right).

The LGM-PI difference in $\delta^{18}\text{O}_{sw}$ ranges from 0.41 to 1.78 permil in surface waters, and from 0.76 to 1.18 permil in the intermediate water layer (at 980 to 1240 m depth). When the enrichment effect due to LGM continental ice accumulation is removed, the shift in $\delta^{18}\text{O}_{sw}$ (LGM_{unenr}-PI) ranges from -0.69 to 0.68 permil in surface waters, and from -0.35 to 0.07 permil in the intermediate water layer. The modelled pattern of LGM_{unenr}-PI $\delta^{18}\text{O}_{sw}$ is the product of changes in the physical state of the ocean, due to water mass reorganization and changes in the magnitude, timing, and/or isotopic content of moisture fluxes at the sea surface. Therefore, while the primary cause of isotopic differences in LGM seawater relative to the preindustrial is the seawater enrichment due to the accumulation of continental ice, local changes can produce a sizeable isotopic shift (here, of up to 0.69 permil).

3.9 Discussion and summary

Stable water isotopes have been implemented in a range of atmosphere, ocean, and coupled models to date (see Table 3.2). Of these, few are fully coupled atmosphere-ocean models, and fewer still are Earth system models of intermediate complexity (or EMICs). The isotope-enabled UVic ESCM may fill a unique role in that it is an intermediate complexity model with a full ocean GCM, and the atmosphere and ocean models are fully-coupled for all fluxes (heat, moisture, oxygen isotopes, etc.).

When undertaking the implementation of H_2^{18}O and H_2^{16}O in the UVic model, it was unknown as to whether the final distribution of $\delta^{18}\text{O}$ would prove sufficiently realistic, given the simplified atmospheric sub-component of the model, and especially the model formulation of condensation (i.e. precipitation forms when relative humidity exceeds 85%).

As discussed in Section 3.3, despite the model's similarity to NCEP in global annual mean temperature and precipitation, significant discrepancies are seen in the seasonal cycles of temperature and precipitation over broad continental regions. While the modelled annual and seasonal distribution of heat is fairly well represented over ocean regions, at low and mid-latitudes marine precipitation is both underestimated at its peak locations (e.g. the tropical Western Pacific), and overestimated otherwise (e.g. the eastern Pacific to the west of USA and Peru). For stable water isotopes, the

lack of an explicit representation of atmospheric vertical structure and motions in the model may be the most significant model challenge. Isotopic fluxes resulting from dynamical, small-scale processes that are neglected in the model can simply not be captured. Nevertheless, as noted below, the analysis indicates that the UVic model succeeds in capturing the broad pattern and magnitude of δ^{18}O composition in mean annual precipitation and seawater.

Long (5 kyr) equilibrium model simulations have been performed under preindustrial and LGM boundary conditions and the resulting isotope fields were compared to available data. In the evaluation of the model isotope distribution, the model is found to reproduce the large-scale patterns in precipitation. At the regional scale, the model is reasonably consistent with preindustrial $\delta^{18}O_{precip}$ observations throughout Australia, Africa, South America, and across Asia (with the exception of the locally enriched area east of the Himalayas). The Antarctic region contains the maximum depletion in $\delta^{18}O_{precip}$ both in the model and in observations, although precipitation in the model is not as depleted as observations from the Antarctic Surface Snow Dataset (Masson-Delmotte et al., 2008) suggest. Likewise, northern North America (Canada) is too enriched in the model relative to observations.

Under preindustrial forcing, the model reproduces the observed large-scale sea surface isotopic patterns, including enrichment in evaporative regions and depletion at high latitudes, but the model is not as depleted as the observations in northern high-latitude seawater. This shortcoming is reflected in the model salinity-δ^{18}O relationship in surface waters, which while similar to the observations in the tropics, is significantly weaker in extratropical surface waters. Model and observations are highly similar for global mean salinity and δ^{18}O values in intermediate and deep waters.

Given these results, the isotope-enabled UVic ESCM may be best utilized in performing simulations requiring integrations over long time scales, in combination with determining oxygen isotopic anomalies (between simulated climate states). The implementation of oxygen isotopes in the UVic ESCM adds new functionality to this intermediate-complexity model, allowing exploration of the potential processes determining the distribution of δ^{18}O for a given climate. For example, one useful application may involve investigating variability in seawater isotopic content under distinct climate states. Finally, the model may be well suited to improving the interpretation of oxygen isotope records from ocean sediment cores.

Ocean sediment core δ^{18}O records are generated from the seafloor accumulation

of marine planktonic and benthic calcareous plankton (e.g. foraminifera) which form their shells essentially in equilibrium with $\delta^{18}O_{sw}$ (recognizing the caveats of species-specific offsets and uncertainty surrounding ontogenic effects) (Rohling and Cooke, 2003). Since the shell calcite $\delta^{18}O$ is a function of both $\delta^{18}O_{sw}$ and seawater temperature (with temperature inversely proportional to fractionation), interpreting changes in $\delta^{18}O_{calcite}$ from a sediment core requires assumptions involving how both $\delta^{18}O_{sw}$ and temperature are simultaneously changing (Shackleton, 1974). Given the computational efficiency of an isotope-enabled UVic model with a full ocean model, there may be great usefulness in applying the model to aid in the interpretation of planktonic foraminiferal $\delta^{18}O_{calcite}$ records. Relative to the (sparse) land-based LGM-PI reconstructions from ice cores and cave deposits (e.g. Table 3.3 and Figure 3.12), the number of ocean-based records spanning both LGM and PI time periods may be large. Of course, whether the model can be thus exploited will depend on critical tests of fidelity, beginning with the baseline simulations presented here.

Chapter 4

Impact of Glacial-Interglacial Sea Ice Variability on Seawater δ^{18}O

This chapter describes:

- the first global analysis of sea ice isotopic contributions to seawater δ^{18}O;
- the first analysis of the effect of interglacial-glacial sea ice variability on local seawater δ^{18}O;
- results and discussion.

4.1 Radiative forcing and surface conditions for interglacial and glacial climates

To simulate the interglacial and glacial climate states, the model is integrated for 5 kyr under preindustrial (year 1800) and LGM (21 kyr BP) radiative forcing conditions. These include equivalent CO_2 at 284 and 190 ppm, and orbital parameters corresponding to year 1800 and 21 kyr BP, respectively, and present day monthly mean wind fields superimposed with wind stress anomalies calculated dynamically as a function of surface pressure anomalies (Weaver et al., 2001) for both climate states. Both interglacial and glacial simulations employ ocean bathymetry and sea level corresponding to modern conditions with a closed Bering Strait. For the glacial climate, LGM land ice is simulated after the ICE-4G reconstruction of Peltier (1994). The ICE 4-G implementation includes permanent ice shelves extending from the coast

over multiple ocean points in the Arctic and Antarctic, preventing ocean-atmosphere exchange and sea ice at those grid cells.

4.2 Experimental design and modelling approach

A set of four simulations allows us to isolate the sea ice component of seawater δ^{18}O for the interglacial and glacial climates, and calculate the difference in this field between these climate states. From the interglacial and glacial equilibrium states, a pair of simulations are performed that are identical except that during sea ice formation isotopic fractionation either remains on or is turned off. If isotopic fractionation does not occur during sea ice formation, there is no isotopic signature of sea ice in the global ocean. Both interglacial and glacial simulation pairs (with fractionation on and off during ice formation, called 'frac-on' and 'frac-off' hereafter) are integrated for 3 kyr. Table 4.1 summarizes the experimental design and model simulations.

By differencing the pair of simulated seawater oxygen isotope fields ('frac-on' minus 'frac-off'), the seawater δ^{18}O field that is due to sea ice is determined for the given climate. For example, glacial seawater δ^{18}O due to sea ice, $\delta^{18}\mathrm{O}_{glacial}^{f(seaice)}$, is calculated as the difference of the pair of glacial seawater oxygen isotopic fields, $\delta^{18}\mathrm{O}_{glacial}^{frac.on}(x,y,z)$ - $\delta^{18}\mathrm{O}_{glacial}^{frac.off}(x,y,z)$. Then, by taking the difference of the seawater oxygen isotopic field due solely to sea ice for the interglacial and glacial climate states ($\delta^{18}\mathrm{O}_{interglacial}^{f(seaice)}(x,y,z) - \delta^{18}\mathrm{O}_{glacial}^{f(seaice)}(x,y,z)$), the local shift in seawater δ^{18}O attributable to sea ice variability is estimated. The analysis is performed for the sea surface (the top ocean model level with a depth of 50 m), averaged over the upper water column (the top four ocean model levels, $0-380$ m), averaged over intermediate waters (ocean model levels $5-12$, or $380-2580$ m), averaged for deep water (ocean model levels $13-19$, corresponding to the depth range $2580-6080$ m), and for the deepest level in the ocean model (k_{max}), representing bottom water.

4.3 Paleotemperature reconstruction error

The isotopic shift due to interglacial-glacial changes in sea ice can then be interpreted in terms of potential error in reconstructing paleotemperature. The paleotemperature equation relates the local seawater temperature (T in $^{\circ}C$) to the isotopic offset between carbonate ($\delta^{18}\mathrm{O}_c$) and seawater ($\delta^{18}\mathrm{O}_w$, letting $A = \delta^{18}\mathrm{O}_w - 0.27‰$): $T = 16.9 - 4.38(\delta^{18}O_c - A) + 0.10(\delta^{18}O_c - A)^2$ (Shackleton, 1974). Because the sea ice

Table 4.1: Model simulations and experimental design.

Boundary Conditions	**Fractionation during sea ice formation**	**Difference of simulations with fractionation on & off**	**Difference of interglacial & glacial seawater $\delta^{18}\mathbf{O}^{f(seaice)}$**
Interglacial (Preindustrial, year 1800)	On	Seawater $\delta^{18}\mathrm{O}^{f(seaice)}_{interglacial}$	Isotopic shift in seawater due to sea ice variability
	Off		
Glacial (LGM, 21 kyr BP)	On	Seawater $\delta^{18}\mathrm{O}^{f(seaice)}_{glacial}$	
	Off		

component of $\delta^{18}\mathrm{O}_w$ can vary between interglacial and glacial climate states, $\delta^{18}\mathrm{O}_w$ is effectively superimposed with a noise term, which would then propagate through the paleotemperature equation if sea ice variability is neglected. We use the known model quantities $\delta^{18}\mathrm{O}_w$ and temperature with the paleotemperature equation of Shackleton (1974) to calculate $\delta^{18}\mathrm{O}_c$. We again solve the paleotemperature equation, this time for seawater temperature (T^*) after having removed the sea ice component from $\delta^{18}\mathrm{O}_w$. The difference between the model temperature T and T^* returns the sea ice isotopic component of the paleotemperature estimate, T_{seaice}. The interglacial-glacial change in T_{seaice} corresponds to the error in reconstructing paleotemperature due to (the neglect of interglacial-glacial) sea ice variability.

4.4 Model interglacial and glacial sea ice

Monthly mean September and March sea surface temperature and the corresponding maximum and minimum sea ice and snow concentrations are plotted for the model's Northern and Southern Hemispheres in Figure 4.1. The modeled monthly mean sea ice concentration is similar to the corresponding monthly climatological sea ice concentrations (1979-1987) constructed from satellite passive-microwave observations

(as in Figures 1.16-1.19 in Wadhams (2000) after Gloersen et al. (1992)). The sea ice model performance is evaluated in Weaver et al. (2001), where the present-day seasonal climatology for sea ice and snow cover (considered together and separately) is demonstrated to be ranked highly against that of other coupled atmosphere-ocean GCMs (their Table 3). Discrepancies include the formation site of North Atlantic Deep Water which is shifted slightly southward in the model. This in turn allows sea ice cover to persist too far south (as shown in Figures 18a and 19 in Weaver et al. (2001)).

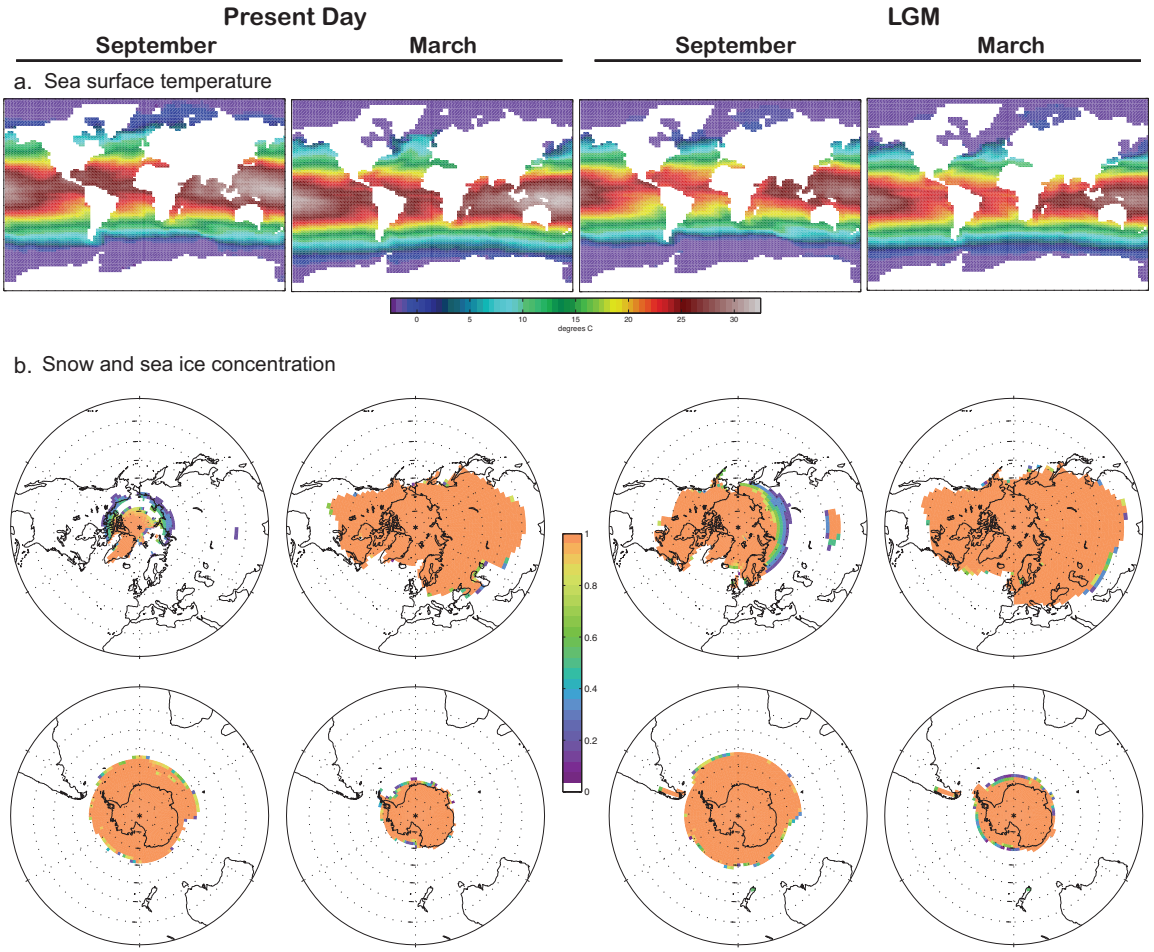

Figure 4.1: Model September and March monthly mean sea surface temperatures (°C) (a) and Northern and Southern Hemisphere sea ice and snow concentration (%) (b) in the preindustrial (left) and LGM (right) simulations.

In the Northern Hemisphere, the maximum sea ice thickness (> 5 m) occurs in

the Canadian Archipelago region of the Arctic, and the mean ice thickness in the Arctic Ocean is approximately 1 m. In contrast, Antarctic average sea ice thickness is approximately 40 cm. A maximum thickness of Southern Hemisphere ice ($\leq$ 2.1 m) is found near 75° W. The simulated seasonal cycle of Northern Hemisphere sea ice area produces a maximum in early March and a minimum in early September. The Southern Hemisphere cycle reaches its peak in mid-September and its minimum in mid-February. The modeled seasonal cycle is very similar in timing to that observed in the climatology (Gloersen et al., 1992; Wadhams, 2000).

Figure 4.1 also maps the modeled glacial monthly mean September and March fields of sea surface temperature with the corresponding sea ice and snow concentrations for each hemisphere. Under glacial conditions, perennial ice cover is simulated for the entire Arctic Ocean, in the northern Labrador Sea, and in the northeastern North Atlantic (north of $\sim$ 70°N), while winter sea ice extends significantly further south. The modeled LGM winter sea ice edge appears consistent with available recent reconstructions (Kucera et al., 2005; de Vernal et al., 2006). Northern Hemisphere glacial sea ice volume at its peak is three times that of the interglacial (about 4.5×10^4 km^3 vs 1.5×10^4 km^3, respectively).

In the Southern Hemisphere, glacial sea ice covers at least 20% more area at its maximum than under interglacial conditions (approximately 2.5×10^7 km^2 vs 2.1×10^7 km^2). Compared to a range of LGM winter and summer ice edge reconstructions for the Southern Hemisphere summarized in Gersonde et al. (2005), the modeled winter ice distribution is indistinguishable from the reconstructions except for the region south of Australia (90°E to 150°E) where the model simulates less ice, while the modeled summer ice edge is more similar to the EPILOG reconstruction (albeit with less ice simulated in the region of 30°W to 10°E) (Gersonde et al., 2005) than that of CLIMAP Project Members (1981). Additional aspects of simulated interglacial and glacial sea ice variability, including seasonality and patterns of ice growth and melt, are presented in Appendix C.

4.5 Interglacial and glacial seawater δ^{18}O due to sea ice

The interglacial and glacial seawater δ^{18}O fields due to sea ice ($\delta^{18}O^{f(seaice)}_{interglacial}$ and $\delta^{18}O^{f(seaice)}_{glacial}$) are shown in Figure 4.3. A positive (i.e. isotopically enriched) sea ice

contribution to seawater δ^{18}O corresponds to regions dominated by a net addition of sea ice meltwater, while a negative (i.e. isotopically depleted) sea ice contribution is associated with a net addition of sea ice brine. For example, in the interglacial sea surface, a net brine addition is present in the Labrador Sea and adjacent to Arctic and Antarctic coasts, while a net meltwater addition is apparent in the Arctic Chukchi Sea (Fig. 4.3a). A similar pattern of sea ice isotopic contribution is found when the signal is averaged over the upper water column (Fig. 4.3b). In the model circum-Antarctic, significant brine production results in the largest negative isotopic contribution from sea ice to deep water (Fig. 4.3d, -0.0135‰, found at 65.7°S, 48.6°W). Interglacial bottom waters receive only very diluted isotopic contributions from sea ice, except in the Labrador Sea and Arctic coastal regions, which are dominated by net brine addition (Fig. 4.3e).

The glacial sea surface exhibits a markedly different pattern of sea ice meltwater and brine additions in the Northern Hemisphere from the interglacial. The Labrador Sea net brine addition is larger, while the net meltwater addition is focused between southern Greenland and northern Europe, entirely displaced from the Arctic basin (Fig. 4.3f). This pattern extends throughout the surface water column (averaged over the top 380 m) (Fig. 4.3g). Glacial deep water contains its largest isotopic contribution from sea ice brine production (-0.0167‰ at 62.1°S, 45°W) in the circum-Antarctic, which appears to be enhanced relative to the interglacial state (Fig. 4.3i). In glacial bottom waters, the most significant depleted (net brine) contribution is found in the Labrador Sea, while the largest enriched (net melt) contribution is in the North Sea (Fig. 4.3j).

Table 4.2 lists the maximum positive and negative sea ice isotopic contribution to seawater δ^{18}O for the simulated interglacial and glacial sea surface (top 50 m), surface waters (0 to 380 m, averaged), intermediate water (380 to 2580 m, averaged), deep water ($>$ 2580 m, averaged), and bottom water (corresponding to the deepest

---

Figure 4.2 *(following page)*: Annual mean seawater δ^{18}O due to sea ice in equilibrium interglacial (top row) and glacial (bottom row) climates in the model sea surface (top 50 m) (a, f), surface waters (averaged over the top 380 m) (b, g), intermediate water (380-2580 m averaged) (c, h), deep water ($>$ 2580 m averaged) (d, i), and bottom water (deepest ocean model level, k_{max}) (e, j). Red (blue) regions in the figure correspond to a positive (negative) isotopic component, and therefore a net addition of sea ice meltwater (brine).

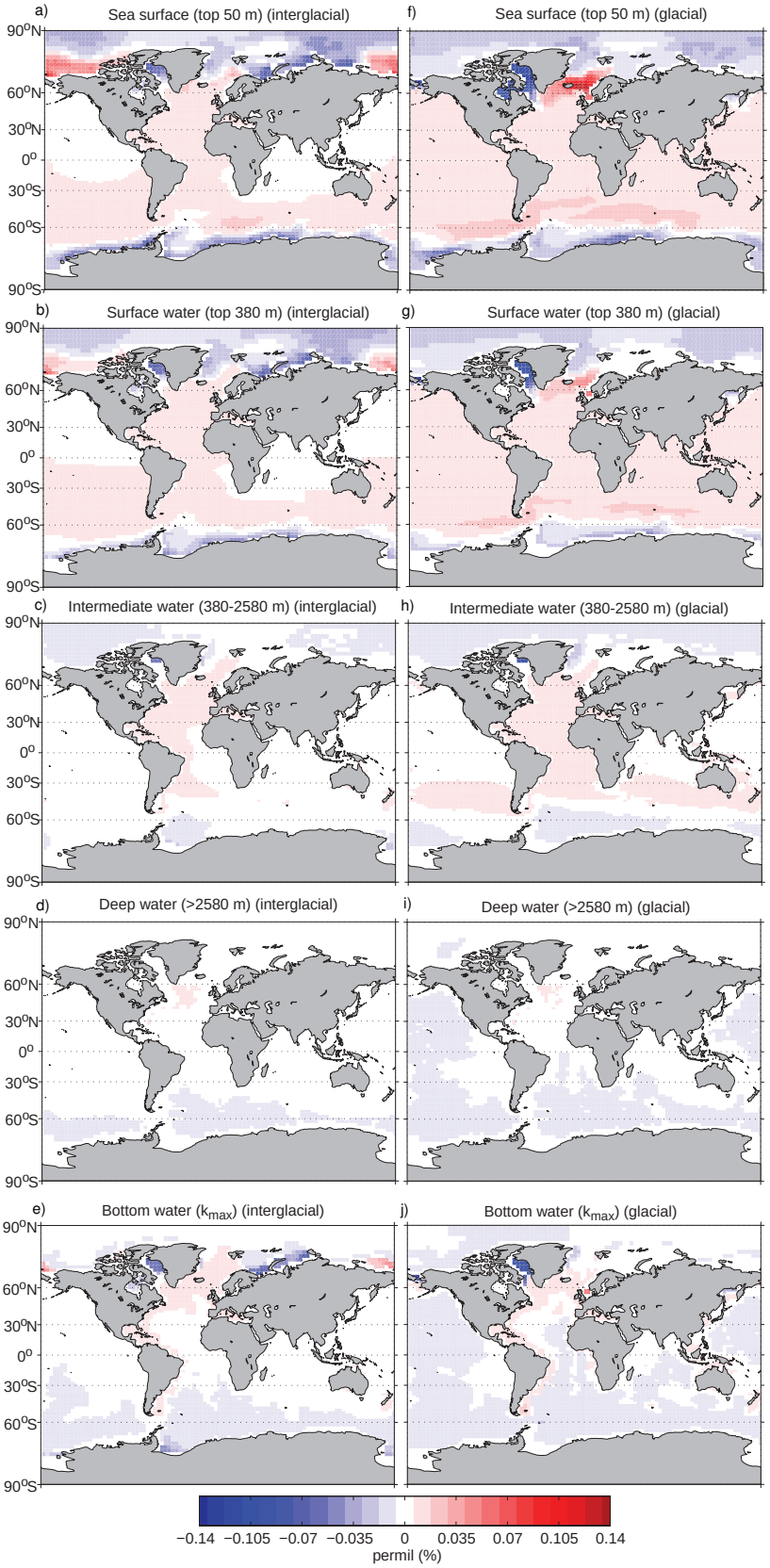
a) Sea surface (top 50 m) (interglacial)
f) Sea surface (top 50 m) (glacial)
b) Surface water (top 380 m) (interglacial)
g) Surface water (top 380 m) (glacial)
c) Intermediate water (380-2580 m) (interglacial)
h) Intermediate water (380-2580 m) (glacial)
d) Deep water (>2580 m) (interglacial)
i) Deep water (>2580 m) (glacial)
e) Bottom water (k_max) (interglacial)
j) Bottom water (k_max) (glacial)
90°N
60°N
30°N
0°
30°S
60°S
90°S
−0.14 −0.105 −0.07 −0.035 0 0.035 0.07 0.105 0.14
permil (%)

ocean model level). The magnitude of isotopic contributions by sea ice processes to the sea surface and surface waters is as large as 0.14‰, while that to deep water is smaller by an order of magnitude (< 0.02‰).

Table 4.2: Upper and lower bounds of the sea ice isotopic contribution to $\delta^{18}O_w$ (in units of permil): interglacial, glacial, and interglacial-glacial shift (IG-G).

	Sea surface	**Surface water**	**Intermediate water**	**Deep water**	**Bottom water**
Interglacial					
max	0.0849	0.0687	0.0093	0.0058	0.0525
min	−0.0869	−0.0748	−0.0554	−0.0135	−0.0791
Glacial					
max	0.1255	0.1280	0.0546	0.0122	0.1304
min	−0.1379	−0.1351	−0.1095	−0.0167	−0.1346
IG-G shift					
max	0.1255	0.1280	0.0546	0.0085	0.1304
max site	65.7°N, 171°W	65.7°N, 171°W	74.7°N, 63°W	35.1°S, 41.4°W	65.7°N, 171°W
min	−0.1237	−0.0748	−0.0266	−0.0102	−0.0791
min site	62.1°N, 1.8°W	76.5°N, 91.8°E	74.7°S, 189°W	71.1°S, 19.8°W	76.5°N, 91.8°E

4.6 Interglacial-glacial shift in seawater $\delta^{18}O$ due to sea ice

We find evidence for a change in local seawater isotope content due solely to differences in glacial versus interglacial sea ice. The shift in local seawater $\delta^{18}O$ due to interglacial-glacial sea ice variability is shown in Figure **??** (a-e), where positive (negative) isotopic shifts correspond to a more enriched (depleted) interglacial sea ice isotopic contribution to seawater. The interglacial-glacial shift due to sea ice variability is most significant in high latitude surface waters of the Northern Hemisphere, namely the Labrador Sea and the northeastern North Atlantic, with a magnitude as large as 0.13 permil. The isotopic changes detected in intermediate water ($380 - 2580$ m, averaged) and deep water (> 2580 m, averaged) due to interglacial-glacial sea ice variability are small (≤ 0.05‰ and 0.01‰, respectively) relative to those in surface water. Regions where isotopic changes in bottom water are not insignificant

include the shallow Arctic shelf regions, the Bering Strait, and in Baffin Bay west of Greenland.

The largest positive and negative isotope contributions from sea ice for each analyzed depth interval (sea surface, upper water column, intermediate water, deep water, and bottom water) are summarized in Table 4.2, along with the greatest positive and negative isotope shift between interglacial and glacial climate states (i.e. the difference interglacial minus glacial $\delta^{18}O^{f(seaice)}$). The variation of the isotopic shift with depth is shown in Figure 4.4 for six Northern Hemisphere high latitude locations where the anomalies are particularly pronounced (see inset map for locations).

The sea ice component of paleotemperature (T_{seaice}) is calculated for interglacial and glacial climates (not shown). The difference in T_{seaice} in the interglacial and glacial climates corresponds to the potential error in reconstructing paleotemperature due to sea ice variability, shown in Figure **??** (f-j). The spatial pattern of paleotemperature error mirrors that of the interglacial-glacial shift in seawater $\delta^{18}O$ (Fig. **??** a-e). The largest local paleotemperature error is 0.44°C at the sea surface, 0.44°C in the upper water column, 0.19°C in intermediate water, −0.04°C in deep water, and 0.45°C in bottom water.

Figure 4.3 *(following page)*: Shift in annual mean seawater $\delta^{18}O$ ($\Delta\delta^{18}O$) due to interglacial-glacial variability in sea ice in the model sea surface (top 50 m) (a), surface waters (averaged over the top 380 m) (b), intermediate water (380-2580 m averaged) (c), deep water (> 2580 m averaged) (d), and bottom water (deepest ocean model level, k_{max}) (e). Red (blue) regions in the figure correspond to a positive (negative) isotopic shift, and therefore an interglacial state with increased sea ice meltwater (brine) addition and/or decreased brine (meltwater) addition. The bottom row maps the corresponding error in paleotemperature reconstruction (°C) due to interglacial-glacial sea ice variability (f-j).

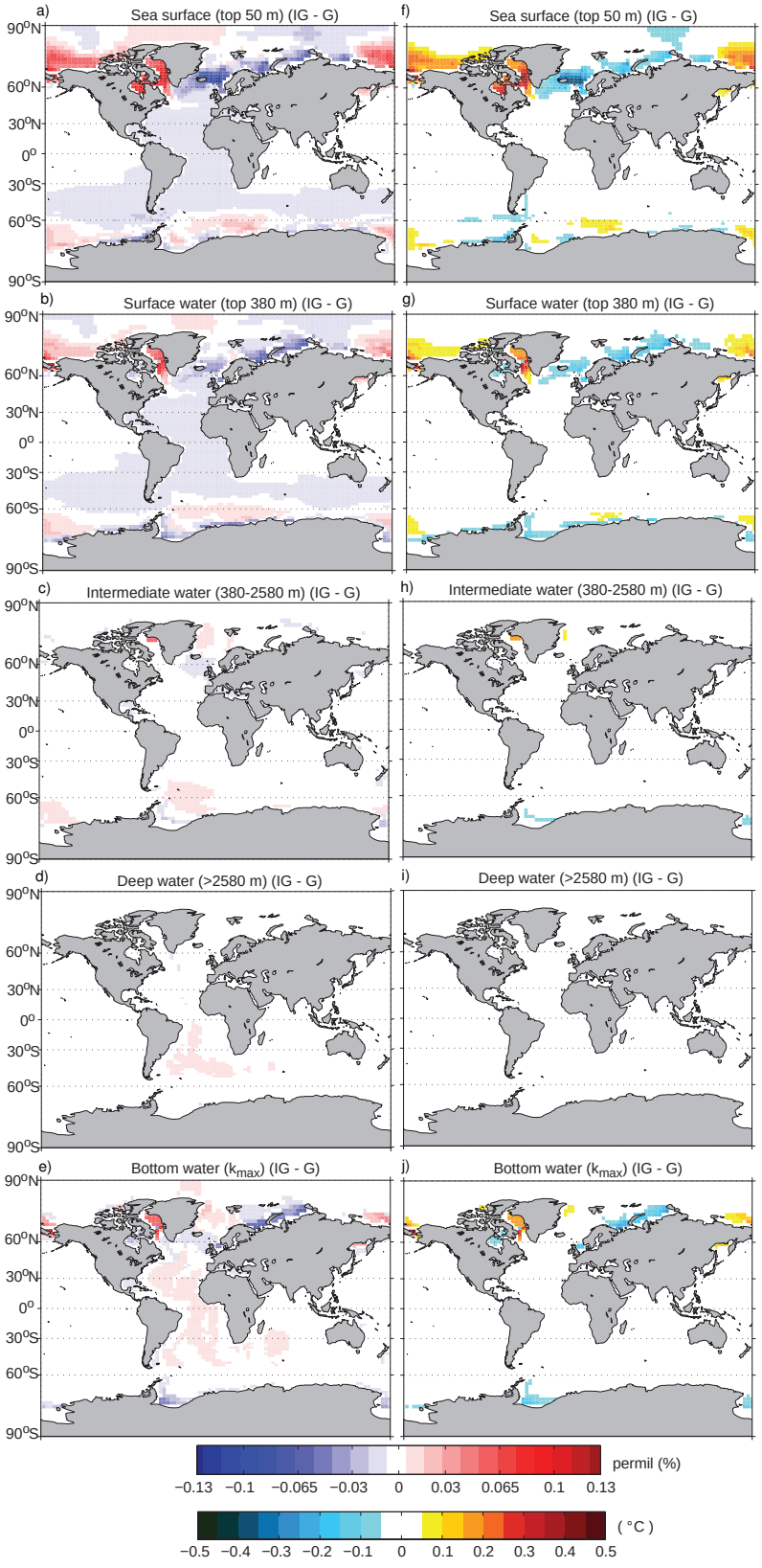
a) Sea surface (top 50 m) (IG - G)
f) Sea surface (top 50 m) (IG - G)
b) Surface water (top 380 m) (IG - G)
g) Surface water (top 380 m) (IG - G)
c) Intermediate water (380-2580 m) (IG - G)
h) Intermediate water (380-2580 m) (IG - G)
d) Deep water (>2580 m) (IG - G)
i) Deep water (>2580 m) (IG - G)
e) Bottom water (k_max) (IG - G)
j) Bottom water (k_max) (IG - G)
90°N
60°N
30°N
0°
30°S
60°S
90°S
permil (%)
−0.13 −0.1 −0.065 −0.03 0 0.03 0.065 0.1 0.13
(°C)
−0.5 −0.4 −0.3 −0.2 −0.1 0 0.1 0.2 0.3 0.4 0.5

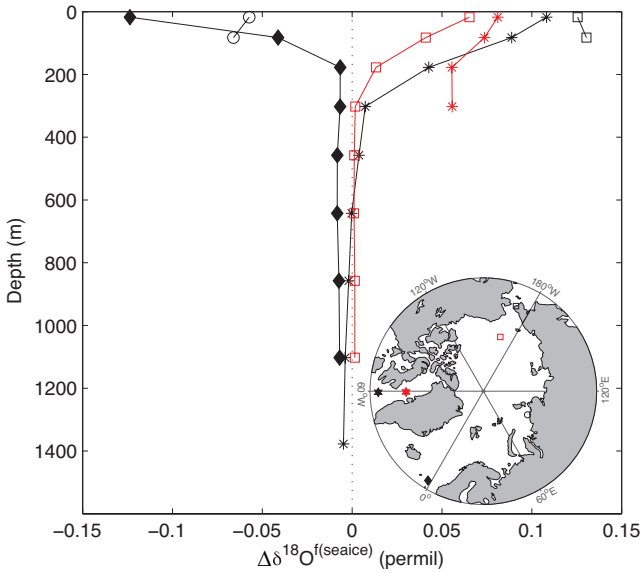

Figure 4.4: Interglacial-glacial shift (Δ) in the annual mean sea ice component of $\delta^{18}O_w$ (permil) at locations indicated on the inset map: 62.1°N, 1.8°W (black diamond), 76.5°N, 91.8°E (black circle), 74.7°N, 167.4°W (red square), 69.3°N, 59.4°W (red star), 62.1°N, 59.4°W (black star), and 65.7°N, 171°W (black square).

4.7 Discussion

That sea ice varied throughout geologic time between glacial and interglacial climates is unquestionable. Changes in sites of sea ice growth and brine rejection, sites of sea ice melt, and rates of sea ice production at a given location can shift the isotopic signature of sea ice processes in seawater. In the model, we indeed observe differences in interglacial versus glacial sea ice extent, volume, and seasonal cycle of growth and melt (see Appendix C).

To gauge the potential effect of the above results on paleoreconstructions, we assess the seawater isotopic content in the model at the grid cells located nearest each North Atlantic sediment core site (between $50° - 85°$N and $65°$W$-20°$E, N$= 64$), primarily those employed by Glacial Atlantic Ocean Mapping (GLAMAP 2000) (Pflaumann et al., 2003). The sediment cores are listed in Table 4.3 and the core sites are mapped in Figure 4.5. In the case of multiple cores corresponding to the same model grid cell, only one core is selected (to avoid sampling the same model location more than once).

Table 4.3: North Atlantic sediment core sites (50° to 85° N and 65° W to 20° E).

Core	**Latitude (°N)**	**Longitude (°E)**
OD41-4-1	84.03	11.24
21533-3	82.03	15.18
PS2876-1	81.91	−9.44
PS2129-1	81.37	17.47
PS2837-5	81.23	2.38
PS2887-1	79.60	−4.61
PS1230-1	78.86	−4.78
17725-1	77.47	4.58
17724-2	76.00	8.33
PS1922-1	75.00	−8.77
PS1919-2	75.00	−11.90
PS2613-6	74.18	−0.48
23294-4	72.75	−10.60
23262-2	72.23	14.43
MD2012	72.15	11.43
17730-4	72.11	7.32
PS1927-2	71.50	−17.12
HU-76-029-033	70.46	−64.65
23351-1	70.36	−18.22
23354-6	70.33	−10.63
PS1730-2	70.12	−17.70
PS1951-1	68.84	−20.82
23056-2	68.50	3.84
23065-2	68.50	0.82
V28-56	68.03	−6.12
1171-1	67.96	−18.61
PS2644-5	67.87	−21.77
23071-3	67.08	2.92
MD95-2011	66.97	7.64
23074-1	66.67	4.91
V27-86	66.60	1.12

Continued on next page

Table 4.3 – continued from previous page

Core	Latitude (°N)	Longitude (°E)
DSDP 337	64.87	−5.34
23519-5	64.80	−29.60
HU-87-033-007	64.40	−57.42
DSDP 352	63.65	−12.47
DSDP 336	63.35	−7.79
ENAM93-21	62.74	−4.00
HU87033	62.65	−53.88
HU-87-033-009	62.51	−59.44
NEAP3K	62.50	−23.57
16396-1	61.87	−11.25
HU2008-029-004-PC	61.46	−58.04
HU97-048-016-PC	59.70	−60.24
NEAP8K	59.47	−23.54
SU90I06	59.45	−39.52
SO82-5	59.17	−30.91
MD99-2242	58.92	−47.12
HU90-013-027-BC	58.76	−57.12
BOFS14	58.62	−19.43
HU90-013	58.21	−48.37
BOFS17	58.00	−16.50
NEAP15K	56.22	−27.49
17051-3	56.16	−31.99
DSDP 552	56.04	−23.23
NA8722	55.50	−14.58
17050-1	55.47	−27.89
23419-8	54.96	−19.75
V23-081	54.25	−16.13
23415-9	53.17	−19.20
SU90-39	52.57	−21.93
17045-3	52.43	−16.67
BOFS05KA	50.68	−21.87
HU91-04	50.33	−45.69

Continued on next page

Table 4.3 – continued from previous page

Core	Latitude (°N)	Longitude (°E)
KN708-1	50.00	−23.75

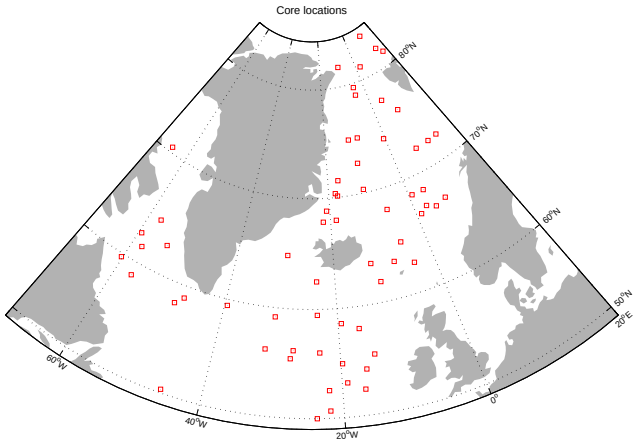

Figure 4.5: Locations of North Atlantic sediment cores. Indicated cores are listed in Table 4.3.

An additional glacial equilibrium simulation is performed without any seawater enrichment from continental ice volume, in order to be able to separate the local seawater isotopic shift into two components − one due to continental ice volume, and the other due to other processes (e.g. changes in precipitation, evaporation, sea ice, etc.). At the model locations corresponding to the North Atlantic sediment core sites, glacial surface water is enriched by 1.11 ± 0.01‰ (mean $\pm 1\sigma$) due to the accumulation of depleted ice on continents. This is demonstrated in Figure 4.6 by the offset between the glacial simulation with enriched seawater (black circles) and the glacial simulation with unenriched seawater (gray circles).

In the southernmost region of the domain, interglacial seawater δ^{18}O is consistently more enriched than the (unenriched) glacial: across sites, the offset is positive and of a similar magnitude. In contrast, the northernmost region displays variability in both sign (i.e. enrichment or depletion) and magnitude of the interglacial−glacial offset. The greatest variability, however, is found in the central region. This pattern is indicative of a dominant role for cryosphere-ocean interactions in shifting overall seawater δ^{18}O north of ~ 58°N, while a different set of processes, such as atmosphere-ocean interaction (for example, via changes in evaporation and precipitation) acts to

shift overall seawater δ^{18}O south of $\sim 58°$N.

The contribution of sea ice processes to the isotopic shift in surface seawater is plotted for each core site in Figure 4.7 (green bars), along with the total shift in seawater δ^{18}O (gray bars). The calculation of the former is described in Section 4.2. The latter is calculated as the difference between surface seawater δ^{18}O from the interglacial and unenriched glacial simulations. If instead the difference between the interglacial and enriched glacial simulation were to be determined, then all calculated shifts would necessarily include the additional 1.11 ± 0.01‰ offset due to continental ice. This total shift would obscure the physical climatic mechanisms producing changes in surface seawater δ^{18}O. Hence, the effects of seawater enrichment due to continental ice are not included, while all other interglacial-glacial shifts in the hydrologic cycle and ocean circulation are represented in the plotted shift in seawater δ^{18}O.

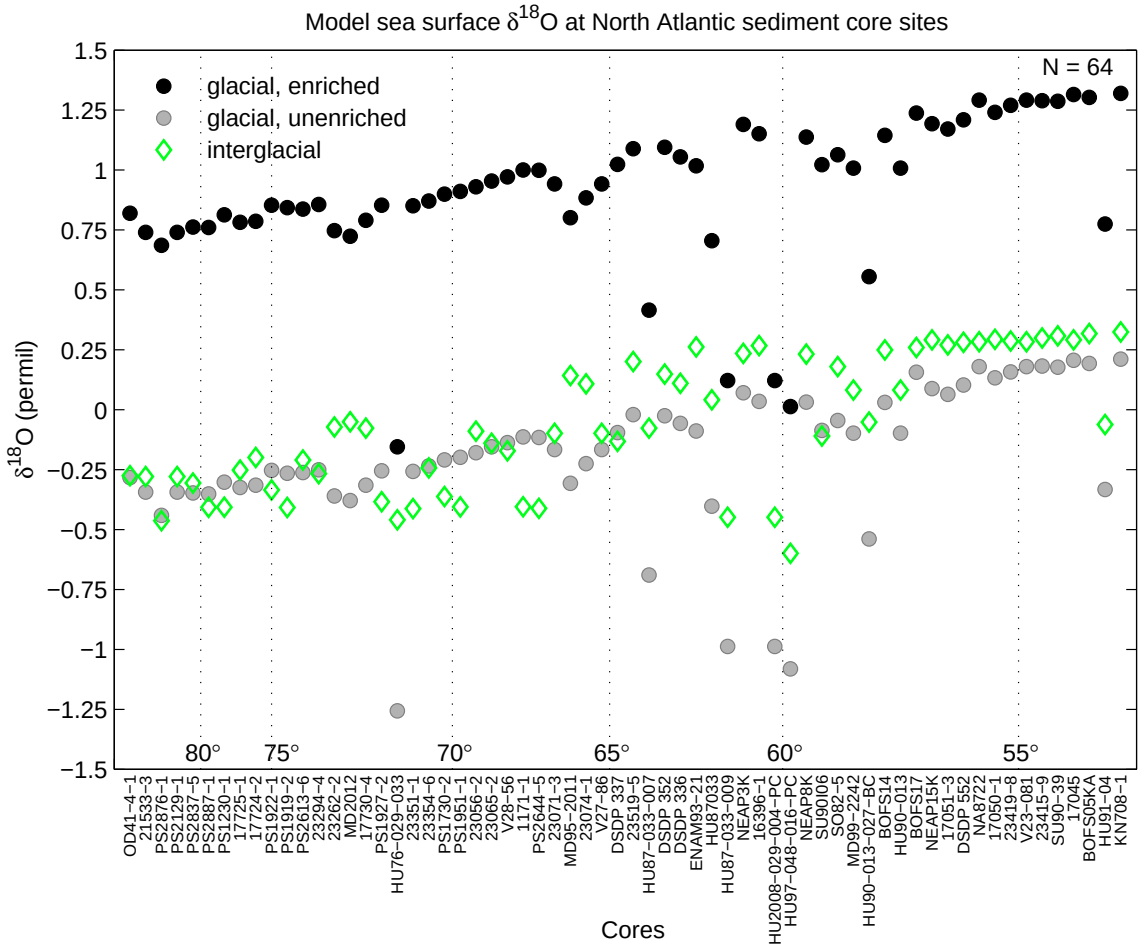

Figure 4.6: Seawater δ^{18}O sampled from the model grid cell nearest each North Atlantic sediment core (listed in Table 4.3) in the interglacial and glacial simulations. The two glacial simulations are with and without ocean isotopic enrichment due to continental ice volume.

Indeed, sea ice processes have a negligible isotopic contribution to surface seawater $\Delta\delta^{18}$O at sites south of $\sim 58°$N. Interestingly, sea ice has almost no impact on $\Delta\delta^{18}$O north of 70°N, with the exception of HU76-029-033 in Baffin Bay. This suggests that $\Delta\delta^{18}$O in the northern region of the domain results from changes in atmospheric forcing (e.g. evaporation, precipitation), discharge of freshwater from continents, and/or ocean circulation. In the central region of the domain ($58 - 70°$N) at sites where the sea ice contribution and the total observed seawater isotopic shift have the same sign, sea ice processes contribute between $\sim 7.7\%$ and $\sim 26.5\%$ of

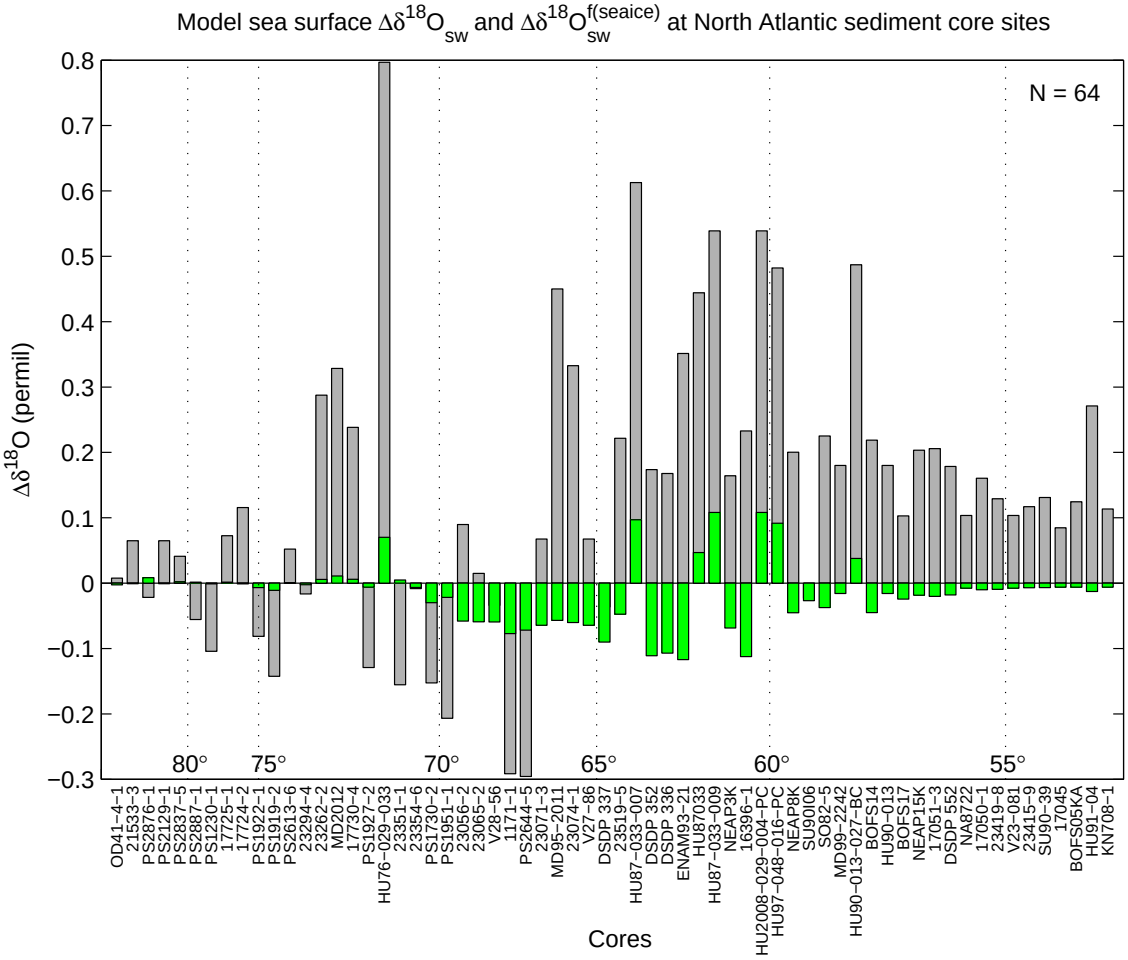

Figure 4.7: Interglacial-glacial shift in seawater δ^{18}O (gray bars), and the sea ice component of the shift (green bars), sampled from the model grid cell nearest each North Atlantic sediment core (listed in Table 4.3 and mapped in Fig. 4.5). The total interglacial-glacial shift in seawater δ^{18}O is the difference between the interglacial and unenriched ocean glacial simulations, hence the effects from ocean enrichment due to glacial continental ice volume are not included.

the observed seawater δ^{18}O shift. At those sites where the sea ice component of the shift is in the opposite direction of the observed shift in seawater δ^{18}O (e.g. 23056-2 or DSDP 336), the sea ice component may be sizeable, but competing effects cause local seawater δ^{18}O to change in the opposite direction. These effects amount to an unknown combination of changes in evaporation, precipitation, freshwater discharge from land, or ocean circulation (potentially each with an isotopic shift of unknown magnitude). Similarly, at sites where the sea ice component has the same sign but is

larger than the observed seawater $\Delta\delta^{18}$O (e.g. V28-56 or DSDP 337), again changes in other hydrological fluxes or circulation work to effectively cancel a portion of the contribution of sea ice processes to the isotopic shift at the site.

Bauch and Bauch (2001) concluded that the sea ice brine hypothesis for shifting benthic carbonate δ^{18}O in northern polar regions is possible but highly unlikely. The results of this study are consistent with that finding: here, the modeled isotopic signature of sea ice is insignificant in intermediate and deep water. It follows that there would be no impact of sea ice variability on the reconstruction of past sea level change, which is based on records of benthic carbonate δ^{18}O.

4.8 Limitations

The following potential caveats should be applied to the present analysis. First, the particular results depend on the distribution of sea ice, sea ice growth and melt, and the subsequent ocean transport of ice brine and meltwater in glacial and interglacial climates simulated by one model. Second, the selection of climate states from glacial-interglacial end members as well as an equilibrium fractionation factor of 3‰ during sea ice formation in the model implies that the calculated isotopic shift attributed to sea ice variability represents an upper-end estimate. Third, in addition to the effect of sea ice variability investigated here, the variability of the other processes that can affect $\delta^{18}O_{local}$ may obviously also contribute uncertainty. Fourth, variability in seawater δ^{18}O is recorded in biogenic carbonate concurrently with superimposed temperature effects and vital effects of the calcifying organisms. This latter biological aspect is not considered, but could potentially introduce additional, non-trivial error. In fact, the dominant species of high latitude foraminifera, *Neogloboquadrina pachyderma* (left-coiling) (Npl), thrives in very high-salinity waters, and as such, may be more likely to record seawater δ^{18}O with a significant component of sea ice brine (Ravelo and Hillaire-Marcel, 2007). Finally, the presented results are applicable for the current continental configuration, and for climate states within the range of atmospheric CO_2 levels considered in this study. As discussed by Raymo (1994), Northern Hemisphere glaciation began approximately 2.5 Ma ago, initially with seasonal Arctic sea ice and later ($\sim$ 1.6 Ma) with perennial sea ice cover, while perennial sea ice existed in the Weddell Sea after 2.46 Ma. Together these constraints may limit the timescale of relevance of the present results to possibly the last 2.4 myr (Pliocene to modern).

4.9 Summary and conclusions

The current study presents a global model analysis of the contribution of sea ice to seawater isotope chemistry, and the potential for variable sea ice to shift local seawater δ^{18}O. The modeled contribution of sea ice to seawater δ^{18}O for interglacial and glacial states is as large as 0.14‰. Interglacial-glacial sea ice variability results in up to 0.13‰ shift in local seawater δ^{18}O, or a maximum local temperature error on the order of 0.5°C. Results indicate that neglecting sea ice variability contributes error to paleoproxy interpretation at ocean sites influenced by sea ice brines and meltwater, notably in surface waters of the Labrador Sea and northeastern North Atlantic.

These results allow the estimation of the maximum possible change in local seawater δ^{18}O as a function of interglacial-glacial sea ice variability, one process that can shift seawater isotopic content. While we encourage their application to uncertainty estimates for data sourced from affected sediment core sites, we caution against applying sea ice effect isotopic 'corrections', which would involve additional assumptions.

Chapter 5

Key Results

5.1 Summary

- The UVic model succeeds in capturing the broad pattern and magnitude of δ^{18}O composition in mean annual precipitation and seawater.
- Under preindustrial forcing, the model reproduces the observed large-scale sea surface isotopic patterns, including enrichment in evaporative regions and depletion at high latitudes, but the model is not as depleted as the observations in northern high-latitude seawater.
- Implementing oxygen isotopes in the UVic ESCM provides new model capabilities: specifically, the model now directly simulates a key paleoproxy, and explorations of the processes determining the distribution of δ^{18}O for a given climate can therefore be conducted.
- The isotope-enabled UVic ESCM may be best utilized in performing simulations requiring integrations over long time scales, in combination with determining oxygen isotopic anomalies (between simulated climate states).
- Given the computational efficiency of an isotope-enabled UVic model with a full ocean model, there may be great usefulness in applying the model to aid in the interpretation of planktonic foraminiferal $\delta^{18}O_{calcite}$ records.
- I perform the first global model analysis of the 3-dimensional contribution of sea ice processes to seawater oxygen isotope chemistry - found to be as large as 0.14‰ - for both interglacial and glacial climates.

- Interglacial-glacial sea ice variability results in up to 0.13‰ shift in local seawater $\delta^{18}O$, or a maximum local temperature error on the order of 0.5°C.
- Neglecting sea ice variability contributes error to paleoproxy interpretation at ocean sites influenced by sea ice brines and meltwater, notably in surface waters of the Labrador Sea and northeastern North Atlantic.

Bibliography

Adkins, J. F. and D. P. Schrag, 2001: Pore fluid constraints on deep ocean temperature and salinity during the last glacial maximum. *Geophysical Research Letters*, **28**, 771–774.

Bauch, D. and H. A. Bauch, 2001: Last glacial benthic foraminiferal δ^{18}O anomalies in the polar north atlantic: a modern analogue evaluation. *Journal of Geophysical Research*, **106**, 9135–9143.

Bradley, R. S., 1999: *Paleoclimatology: reconstructing climates of the quaternary*. Harcourt Academic Press, New York, pp. 613 pp.

Brennan, C. E., K. J. Meissner, M. Eby, C. Hillaire-Marcel, and A. J. Weaver, 2012a: Impact of sea ice variability on the oxygen isotope content of seawater under glacial and interglacial conditions. *Paleoceanography*, manuscript 2012PA002385, submitted.

Brennan, C. E., A. J. Weaver, M. Eby, and K. J. Meissner, 2012b: Modelling oxygen isotopes in the University of Victoria Earth System Climate Model for pre-industrial and Last Glacial Maximum conditions. *Atmosphere-Ocean*, doi: 10.1080/07055900.2012.707611, in press.

Broecker, W. S., 1979: The salinity contrast between the Atlantic and Pacific Oceans during glacial time. *Paleoceanography*, **4**, 207–212.

Bryan, K. and L. Lewis, 1979: A water mass model of the world ocean. *Journal of Geophysical Research*, **84**, 311–337.

CLIMAP Project Members, 1981: Seasonal reconstructions of the Earth's surface at the Last Glacial Maximum. *Geological Society of American Map Chart Series MC-36*, 1–18.

Craig, H. and L. I. Gordon, 1965: Deuterium and oxygen-18 variations in the ocean and marine atmosphere. *Stable Isotopes in Oceanographic Studies and Paleo-Temperatures*, E. Tongiorgi, Ed., Lab. Geol. Nucl., Pisa, 9–130.

Crosta, X., J.-J. Pichon, and L. H. Burckle, 1998: Application of modern analog technique to marine Antarctic diatoms: Reconstruction of maximum sea-ice extent at the Last Glacial Maximum. *Paleoceanography*, **13**, 284–297.

Dansgaard, W., 1964: Stable isotopes in precipitation. *Tellus*, **16**, 436–468.

de Vernal, A. and C. Hillaire-Marcel, 2000: Sea-ice cover, sea-surface salinity and halo/thermocline structure of the NW Atlantic: modern vs full glacial conditions. *Quaternary Science Reviews*, **19**, 65–85.

de Vernal, A. and T. Pedersen, 1997: Micropaleontology and palynology of core PAR 87 A-10: a 30,000 years record of paleoenvironmental changes in the Gulf of Alaska, northeast North Pacific. *Paleoceanography*, **12**, 821–830.

de Vernal, A., A. Rosell-Melé, M. Kucera, C. Hillaire-Marcel, F. Eynaud, M. Weinelt, T. Dokken, and M. Kageyama, 2006: Multiproxy reconstruction of LGM sea-surface conditions in the northern North Atlantic. *Quaternary Science Reviews*, **25**, 2820–2834.

de Vernal, A., J.-L. Turon, and J. Guiot, 1994: Dinoflagellate cyst distribution in high latitude environments and quantitative reconstruction of sea-surface temperature, salinity and seasonality. *Canadian Journal of Earth Sciences*, **3**, 48–62.

de Vernal, A., et al., 2005: Reconstruction of sea-surface conditions at middle to high latitudes of the Northern Hemisphere during the Last Glacial Maximum (LGM) based on dinoflagellate cyst assemblages. *Quaternary Science Reviews*, **24**, 897–924.

Delaygue, G., J. Jouzel, and J.-C. Dutay, 2000: Oxygen 18-salinity relationship simulated by an oceanic general circulation model. *Earth and Planetary Science Letters*, **178**, 113–123.

Dokken, T. and E. Jansen, 1999: Rapid changes in the mechanism of ocean convection during the last glacial period. *Nature*, **401**, 458–461.

Duffy, M. E., P.B. and A. Weaver, 1999: Effects of sinking of salt rejected during formation of sea ice on results of an ocean-atmosphere-sea ice climate model. *Geophysical Research Letters*, **26**, 1739–1742.

Duplessy, J.-C., P.-L. Blanc, and A. W. H. Be, 1981: Oxygen-18 enrichment of planktonic foraminifera due to gametogenic calcification below the euphotic zone. *Science*, **213**, 1247–1250.

Duplessy, J.-C., L. Labeyrie, and C. Waelbroeck, 2002: Constraints on the ocean oxygen isotopic enrichment between the Last Glacial Maximum and the Holocene: Paleoceanographic implications. *Quaternary Science Reviews*, **21**, 315–330.

Duplessy, J.-C., C. Lalou, and A. C. Vinot, 1970: Differential isotopic fractionation in benthic foraminifera and paleotemperatures reassessed. *Science*, **168**, 250–251.

Eicken, H., 1998: Deriving modes and rates of ice growth in the Weddell Sea from microstructural, salinity and stable-isotope data. *Antarctic sea ice: Physical Processes, Interactions and Variability, Antarctic Research Series*, M. O. Jeffries, Ed., AGU, Washington, D.C., Vol. 74, 89–122.

Ekwurzel, B., P. Schlosser, R. A. Mortlock, R. G. Fairbanks, and J. H. Swift, 2001: River runoff, sea ice meltwater, and pacific water distribution and mean residence times in the Arctic Ocean. *Journal of Geophysical Research*, **106**, 9075–9092.

Gat, J. R., 1996: Oxygen and hydrogen isotopes in the hydrologic cycle. *Annual Review of Earth and Planetary Science*, **24**, 225–262.

Gent, P. R. and J. C. McWilliams, 1990: Isopycnal mixing in ocean circulation models. *Journal of Physical Oceanography*, **20**, 150–155.

Gersonde, R., X. Crosta, A. Abelmann, and L. Armand, 2005: Sea-surface temperature and sea ice distribution of the Southern Ocean at the EPILOG Last Glacial Maximum–a circum-Antarctic view based on siliceous microfossil records. *Quaternary Science Reviews*, **24**, 869–896.

Gloersen, P., W. J. Campbell, D. J. Cavalieri, J. C. Comiso, C. L. Parkinson, and H. J. Zwally, 1992: Arctic and Antarctic sea ice, 1978-1987: Satellite passive-microwave observations and analysis. *National Aeronautics and Space Administration*, Vol. Rep. NASA SP-511, 290pp.

Grossman, E. L., 1987: Stable isotopes in benthic foraminifera: a study of vital effect. *Journal of Foraminiferal Research*, **17**, 48–61.

Hibler, W. D., 1979: A dynamic thermodynamic sea ice model. *Journal of Physical Oceanography*, **9**, 815–846.

Hillaire-Marcel, C. and A. de Vernal, 2008: Stable isotope clue to episodic sea ice formation in the glacial North Atlantic. *Earth and Planetary Science Letters*, **268**, 143–150.

Hoffmann, G., M. Werner, and M. Heimann, 1998: Water isotope module of the ECHAM atmospheric general circulation model: a study on timescales from days to several years. *Journal of Geophysical Research*, **103**, 16 871–16 896.

Hunke, E. C. and J. K. Dukowicz, 1997: An elastic-viscous-plastic model for sea ice dynamics. *Journal of Physical Oceanography*, **27**, 1849–1867.

IAEA/WMO, 2006: Global Network of Isotopes in Precipitation. Accessible at: http://www.iaea.org/water., accessible at: http://www.iaea.org/water.

Joussaume, S. and J. Jouzel, 1993: Paleoclimatic tracers: an investigation using an atmospheric general circulation model under ice age conditions 2. Water isotopes. *Journal of Geophysical Research*, **98**, 2807–2830.

Joussaume, S., J. Jouzel, and R. Sadourny, 1984: A general circulation model of water isotope cycles in the atmosphere. *Nature*, **311**, 24–29.

Jouzel, J., 1986: Isotopes in cloud physics: multiphase and multistage condensation processes. *Handbook of environmental isotope geochemistry*, P. Fritz and J. C. Fontes, Eds., Elsevier, Amsterdam, Vol. 2, The terrestrial environment, B, 61–112.

Jouzel, J., R. D. Koster, R. J. Suozzo, and G. L. Russell, 1994: Stable water isotope behavior during the last glacial maximum: a general circulation model analysis. *Journal of Geophysical Research*, **99D**, 25 791–25 801.

Jouzel, J., C. Lorius, J. R. Petit, C. Genthon, N. I. Barkov, V. M. Koylyakov, and V. M. Petrov, 1987a: Vostok ice core: a continuous isotope temperature record over the last climatic cycle (160, 000 years). *Nature*, **329**, 403–408.

Jouzel, J. and L. Merlivat, 1984: Deuterium and O-18 in precipitation: Modeling of the isotopic effects during snow formation. *Journal of Geophysical Research*, **89**, 1749–1757.

Jouzel, J., G. L. Russell, R. J. Suozzo, R. D. Koster, J. W. C. White, and W. S. Broecker, 1987b: Simulations of the HDO and $H_2^{18}O$ atmospheric cycles using the NASA GISS general circulation model: the seasonal cycle for present-day conditions. *Journal of Geophysical Research*, **92**, 14 739–14 760.

Kalnay, E., et al., 1996: The NCEP/NCAR 40-year reanalysis project. *Bulletin of the American Meteorological Society*, **77**, 437–471.

Kucera, M., et al., 2005: Reconstruction of the glacial Atlantic and Pacific sea-surface temperatures from assemblages of planktonic foraminifera: multi-technique approach based on geographically constrained calibration datasets. *Quaternary Science Reviews*, **24**, 951–998.

Langebroek, P. M., M. Werner, and G. Lohmann, 2011: Climate information imprinted in oxygen-isotopic composition of precipitation in Europe. *Earth and Planetary Science Letters*, **311**, 144–154.

Lee, J.-E., I. Fung, D. J. DePaolo, and C. C. Henning, 2007: Analysis of the global distribution of water isotopes using the NCAR atmospheric general circulation model. *Journal of Geophysical Research*, **112 (D16306)**, doi:10.1029/2006JD007657.

LeGrande, A. N. and G. A. Schmidt, 2006: Global gridded data set of the oxygen isotopic composition in seawater. *Geophysical Research Letters*, **33 (L12604)**, doi:10.1029/2006GL026011.

LeGrande, A. N., G. A. Schmidt, D. T. Shindell, C. V. Field, R. L. Miller, D. M. Koch, G. Faluvegi, and G. Hoffmann, 2006: Consistent simulations of multiple proxy responses to an abrupt climate change event. *Proceedings of the National Academy of Sciences of the United States of America*, Vol. 103, 837–842.

Macdonald, R. W., D. W. Paton, E. C. Carmack, and A. Omstedt, 1995: The freshwater budget and under-ice spreading of the Mackenzie River water in the Canadian Beaufort Sea based on salinity and $^{18}O/^{16}O$ measurements in water and ice. *Journal of Geophysical Research*, **100**, 895–919.

Majoube, M., 1971a: Fractionnement en oxygene 18 entre la glace et la vapeur d'eau. *Journal de Chimie Physique*, **68**, 625–636.

Majoube, M., 1971b: Fractionnement en oxygene 18 et en deuterium entre l'eau et sa vapeur. *Journal de Chimie Physique*, **10**, 1423–1436.

Malmgren, F., 1927: On the properties of sea ice. *The Norwegian North Polar Expedition with the Maud, 1918-1925, Scientific Results*, Bergen, Vol. 1, 5, 85pp.

Marsh, R., M. P. L. M. Smith, E. J. Rohling, D. J. Lunt, T. M. Lenton, M. S. Williamson, and A. Yool, 2006: Modelling ocean circulation, climate and oxygen isotopes in the ocean over the last 120, 000 years. *Climate of the Past Discussions*, **2**, 657–709.

Masson-Delmotte, V., et al., 2008: A review of Antarctic surface snow isotopic composition: Observations, atmospheric circulation and isotopic modelling. *Journal of Climate*, **21**, 3359–3387.

Mathieu, R., D. Pollard, J. E. Cole, J. W. C. White, R. S. Webb, and S. L. Thompson, 2002: Simulation of stable water isotope variations by the GENESIS GCM for modern conditions. *Journal of Geophysical Research*, **107 (D4, 4037)**, doi:10.1029/2001JD900255.

Maykut, G. A. and N. Untersteiner, 1971: Some results from a time-dependent thermodynamic model of Arctic sea ice. *Journal of Geophysical Research*, **76**, 1550–1575.

Meissner, K. J., A. J. Weaver, H. D. Matthews, and P. M. Cox, 2003: The role of land surface dynamics in glacial inception: a study with the UVic Earth System Model. *Climate Dynamics*, **21**, 515–537.

Melling, H. and R. M. Moore, 1995: Modification of halocline source waters during freezing on the Beaufort Sea shelf: evidence from oxygen isotopes and dissolved nutrients. *Continental Shelf Research*, **15**, 89–113.

Mix, A. C. and W. F. Ruddiman, 1984: Oxygen isotope analysis and Pleistocene ice volumes. *Quaternary Research*, **21**, 1–20.

Noone, D. and I. Simmonds, 2002: Associations between δ^{18}O of water and climate parameters in a simulation of atmospheric circulation for 1979-95. *Journal of Climate*, **15**, 3150–3169.

Noone, D. and C. Sturm, 2010: *Comprehensive dynamical models of global and regional water isotope distributions*, 195–219. Springer, New York.

O'Neil, J. R., 1968: Hydrogen and oxygen isotope fractionation between ice and water. *Journal of Physical Chemistry*, **72**, 3683–3684.

Peltier, W. R., 1994: Ice age paleotopography. *Science*, **265**, 195–201.

Pfirman, S., W. Haxby, H. Eicken, M. Jeffries, and D. Bauch, 2004: Drifting Arctic sea ice archives changes in ocean surface conditions. *Geophysical Research Letters*, **31**, doi:10.1029/2004GL020 666.

Pflaumann, U., et al., 2003: Glacial North Atlantic: Sea-surface conditions reconstructed by GLAMAP 2000. *Paleoceanography*, **18**, doi:10.1029/2002PA000 774.

Rasmussen, T. L. and E. Thomsen, 2010: Stable isotope signals from brines in the Barents Sea: implications for brine formation during the last glaciation. *Geology*, **37**, 903–906.

Ravelo, A. C. and C. Hillaire-Marcel, 2007: The use of oxygen and carbon isotopes of foraminifera in paleoceanography. *Proxies in late Cenozoic Paleoceanography*, C. Hillaire-Marcel and A. de Vernal, Eds., Elsevier, Amsterdam, The Netherlands, Developments in Marine Geology, Vol. 1, 735–764.

Raymo, M. E., 1994: The initiation of Northern Hemisphere glaciation. *Annual Reviews of Earth and Planetary Science*, **22**, 353–383.

Redfield, A. C. and I. Friedman, 1969: The effect of meteoric water, melt water and brine on the composition of Polar Sea water and of the deep waters of the ocean. *Deep-Sea Research*, **16**, 197–214, supp.

Risi, C., S. Bony, F. Vimeux, and J. Jouzel, 2010: Water-stable isotopes in the LMDZ4 general circulation model: Model evaluation for present-day and past climates and applications to climatic interpretations of tropical isotopic records. *Journal of Geophysical Research*, **115 (D12118)**, doi:10.1029/2009JD013255.

Roche, D., D. Paillard, and E. Cortijo, 2004a: Constraints on the duration and freshwater release of Heinrich event 4 through isotope modelling. *Nature*, **432**, 379–382.

Roche, D., D. Paillard, A. Ganopolski, and G. Hoffmann, 2004b: Oceanic oxygen-18 at the present day and LGM: equilibrium simulations with a coupled climate model of intermediate complexity. *Earth and Planetary Science Letters*, **218**, 317–330.

Rochon, A., A. de Vernal, H.-P. Sejrup, and H. Haflidason, 1998: Climatic changes and sea-surface conditions during the deglaciation: Palynological evidences from the North Sea. *Quaternary Research*, **49**, 197–207.

Rohling, E. J. and G. R. Bigg, 1998: Paleosalinity and δ^{18}O: a critical assessment. *Journal of Geophysical Research*, **103 (C1)**, 1307–1318.

Rohling, E. J. and S. Cooke, 2003: Stable oxygen and carbon isotopes in foraminiferal carbonate shells. *Modern Foraminifera*, B. K. Sen Gupta, Ed., Springer, 239–258.

Rozanski, K., L. Araguas-Araguas, and R. Gonfiantini, 1993: Isotopic patterns in modern global precipitation. *Climate Change in Continental Isotopic Records*, P. K. Swart, K. C. Lohmann, J. McKenzie, and S. Savin, Eds., American Geophysical Union, Geophysical Monograph Series, Vol. 78, 1–36.

Ruddiman, W. F., 2001: *Earths climate: past and future*. W.H. Freeman and Company, New York, 465 pp. pp.

Sancetta, C., 1983: Effect of Pleistocene glaciation upon oceanographic characteristics of the North Pacific Ocean and Bering Sea. *Deep- Sea Research*, **30**, 851–869.

Savin, S. M. and F. G. Stehli, 1974: *Interpretation of oxygen isotope paleotemperature measurements: effect of the 18O/16O ratio of sea water depth stratification of foraminifera, and selective solution*, Vol. No. 219, 183–191. Colloques Internationaux du Centre National de la Recherche Scientifique (CNRS), Paris.

Schmidt, G. A., 1998: Oxygen-18 variations in a global ocean model. *Geophysical Research Letters*, **25**, 1201–1204.

Schmidt, G. A., G. R. Bigg, and E. J. Rohling, 1999: Global Seawater Oxygen-18 Database - v1.20. Online at http://data.giss.nasa.gov/o18data, online at http://data.giss.nasa.gov/o18data.

Schmidt, G. A., G. Hoffmann, D. T. Shindell, and Y. Hu, 2005: Modeling atmospheric stable water isotopes and the potential for constraining cloud processes and stratosphere-troposphere water exchange. *Journal of Geophysical Research*, **110 (D21314)**, doi:10.1029/2005JD005790.

Schmidt, G. A., A. N. LeGrande, and G. Hoffmann, 2007: Water isotope expressions of intrinsic and forced variability in a coupled ocean-atmosphere model. *Journal of Geophysical Research*, **112 (D10103)**, doi:10.1029/2006JD007781.

Schrag, D. P., G. Hampt, and D. W. Murray, 1996: Pore fluid constraints on the temperature and oxygen isotopic composition of the glacial ocean. *Science*, **272**, 1930–1932.

Scott, E. R. D., 2007: Oxygen isotopes give clues to the formation of planets, moons, and asteroids. Accessed online at http://www.psrd.hawaii.edu/Dec01/Oisotopes.html, accessed online at http://www.psrd.hawaii.edu/Dec01/Oisotopes.html.

Semtner, A. J., 1976: A model for the thermodynamic growth of sea ice in numerical investigations of climate. *Journal of Physical Oceanography*, **6**, 379–389.

Shackleton, N. J., 1974: Attainment of isotopic equilibrium between ocean water and the benthic foraminifera genus Uvigerina: Isotopic changes in the ocean during the last glacial. *Methodes quantitatives d'etude des variations du climat au cours du Pleistocene*, J. Labeyrie, Ed., Editions du C.N.R.S., France, 203–209.

Shackleton, N. J. and N. D. Opdyke, 1973: Oxygen isotope and paleomagnetic stratigraphy of equatorial Pacific core V28-238: oxygen isotope temperatures and ice volumes on a 10^5 year and 10^6 year scale. *Quaternary Research*, **3**, 39–55.

Sinclair, K. E., S. J. Marshall, and T. A. Moran, 2011: A Lagrangian approach to modelling stable isotopes in precipitation over mountainous terrain. *Hydrological Processes*, **25**, 2481–2491.

Stanford, J. D., E. J. Rohling, S. Bacon, A. P. Roberts, F. E. Grousset, and M. Bolshaw, 2011: A new concept for the paleoceanographic evolution of Heinrich event 1 in the North Atlantic. *Quaternary Science Reviews*, **30**, 1047–1066.

Strain, P. M. and F. C. Tan, 2003: Seasonal evolution of oxygen isotope-salinity relationships in high-latitude surface waters. *Journal of Geophysical Research*, **98**, 14 589–14 598.

Tan, F. C. and P. M. Strain, 1980: The distribution of sea ice meltwater in the Eastern Canadian Arctic. *Journal of Geophysical Research*, **85 (C4)**, 1925–1932.

Tindall, J. C., P. J. Valdes, and L. C. Sime, 2009: Stable water isotopes in HadCM3: isotopic signature of El Nino-Southern Oscillation and the tropical amount effect. *Journal of Geophysical Research*, **114 (D04111)**, doi:10.1029/2008JD010825.

Urey, H. C., 1947: The thermodynamic properties of isotopic substances. *Journal of the Chemical Society*, **152**, 190–219.

Urey, H. C., 1948: Oxygen isotopes in nature and in the laboratory. *Science*, **108**, 489–496.

Vidal, L., L. Labeyrie, and T. C. E. van Weering, 1998: Benthic δ^{18}O records in the North Atlantic over the last glacial period (60-10 kyr): evidence for brine formation. *Paleoceanography*, **13**, 245–251.

Vinot-Bertouille, A. C. and J. Duplessy, 1973: Individual isotopic fractionation of carbon and oxygen in benthic foraminifera. *Earth and Planetary Science Letters*, **18**, 247–252.

Wadhams, P., 2000: *Ice in the ocean*. Gordon and Breach, Amsterdam, 351 pp. pp.

Waelbroeck, C., L. Labeyrie, E. Michel, J. C. Duplessy, J. F. McManus, K. Lambeck, E. Balbon, and M. Labracherie, 2002: Sea-level and deep water temperature changes derived from benthic foraminifera isotopic records,. *Quaternary Science Reviews*, **21**, 295–305.

Walker, J. C. G. and K. C. Lohmann, 1989: Why the oxygen isotopic composition of sea water changes with time. *Geophysical Research Letters*, **16**, 323–326.

Weaver, A. J., et al., 2001: The UVic Earth System Climate Model: Model description, climatology, and applications to past, present and future climates. *Atmosphere-Ocean*, **39**, 361–428.

Werner, M., M. Heimann, and G. Hoffmann, 2001: Isotopic composition and origin of polar precipitation in present and glacial climate simulations. *Tellus, Series B*, **53**, 53–71, doi:10.1034/j.1600-0889.2001.01154.x.

Werner, M., P. M. Langebroek, T. Carlsen, M. Herold, and G. Lohmann, 2011: Stable water isotopes in the ECHAM5 general circulation model: Toward high-resolution isotope modeling on a global scale. *Journal of Geophysical Research*, **116**, doi:10.1029/2011JD015681.

Yi, Y., J. J. Gibson, L. W. Cooper, J.-F. Helie, S. J. Birks, J. W. McClelland, R. M. Holmes, and B. J. Peterson, 2012: Isotopic signals (18O, 2H, 3H) of six major rivers draining the Pan-Arctic watershed. *Global Biogeochem. Cycles*, doi:10.1029/2011GB004159, in press.

Yoshimura, K., M. Kanamitsu, D. Noone, and T. Oki, 2008: Historical isotope simulation using Reanalysis atmospheric data. *Journal of Geophysical Research*, **113 (D19108)**, doi:10.1029/2008JD010074.

Yoshimura, K., T. Oki, N. Ohte, and S. Kanae, 2003: A quantitative analysis of short-term ^{18}O variability with a Rayleigh-type isotope circulation model. *Journal of Geophysical Research*, **108 (D20, 4647)**, doi:10.1029/2003JD003477.

Zhou, J., C. J. Poulsen, D. Pollard, and T. S. White, 2008: Simulation of modern and middle Cretaceous marine δ^{18}O with an ocean-atmosphere general circulation model. *Paleoceanography*, **23 (PA3223)**, doi:10.1029/2008PA001596.

Appendix A

Stable Oxygen Isotopes: Background

A.1 Introduction to Oxygen Isotopes

The relative abundance of stable oxygen isotopes - whether in seawater, planktic or benthic calcareous organisms, atmospheric water vapor, or ice stored on land - can be used to understand hydrologic cycling and physical environmental factors, such as temperature. Oxygen isotope abundances in the geologic record provide insight into environmental change through Earth history. Here, the mechanisms by which the relative abundance of oxygen isotopes varies are reviewed for atmospheric water vapor, snow and ice, seawater and biogenic calcium carbonate. The goal is to provide a basic understanding of how δ^{18}O records may be interpreted with respect to paleoclimate changes.

The oxygen isotopes ^{16}O, ^{17}O, and ^{18}O consist of one oxygen atom with 8 protons and 8, 9, or 10 neutrons, respectively. ^{16}O composes approximately 99.8% of all oxygen on Earth, and ^{18}O (^{17}O) accounts for 0.2% ($< 0.1\%$) (Bradley, 1999, p. 129). Due to the presence of the extra one or two neutrons, ^{17}O and ^{18}O have larger atomic mass than ^{16}O. The ratio of ^{18}O to ^{16}O, normalized to a standard (e.g. Vienna Standard Mean Ocean Water (V-SMOW)), defines the quantity δ^{18}O:

$$\delta^{18}O(permil) = \frac{(\frac{^{18}O}{^{16}O})_{sample} - (\frac{^{18}O}{^{16}O})_{standard}}{(\frac{^{18}O}{^{16}O})_{standard}} \times 1000 \qquad \text{(A.1)}$$

Stable oxygen isotopes do not grow or decay. Earth's isotopic composition of oxygen

was set when the Earth was formed, and is a function of the oxygen isotopic composition of the solar system (Scott, 2007). The isotopic composition of oxygen in any one component of the climate system atmosphere, hydrosphere, and cryosphere is not constant. This variation in δ^{18}O over time and space can be used to interpret environmental conditions and changes at the global and local level.

Because oxygen isotopic composition is governed by physical processes including the water cycle, temperature, and ice volume, oxygen isotopes deposited and preserved in marine and terrestrial cores serve as an important repository of paleoclimate information. In this section, I review the primary mechanisms affecting δ^{18}O in various components of the climate system - atmospheric water vapor, snow and ice, sea water, and in biogenic calcium carbonate from ocean sediments. The goal is to provide an understanding of δ^{18}O shifts in time and in space.

A.2 Variability in Atmospheric Water Vapor δ^{18}O

The ratio of ^{18}O to ^{16}O is not constant in the atmosphere, but varies as air masses undergo evaporation and condensation, either by transport away from a water source and continued condensation (resulting from temperature changes) or by transport that changes the latitude (and therefore mean temperature) or altitude (and again temperature). All of these processes may cause the isotopic content of an air mass to change, and the contributions should be evaluated. Here I will present each process the 'rainout effect', 'latitude effect', and 'altitude effect' separately.

Before discussing the processes acting on an atmospheric air mass and their effect on the air mass δ^{18}O, it is important to understand the first order relationships between δ^{18}O in an air mass ($\delta^{18}O_{vapor}$), δ^{18}O in the precipitation falling from from the air mass ($\delta^{18}O_{precip}$), and temperature.

A water molecule is composed of two hydrogen atoms and one oxygen atom. Hydrogen has two isotopes, ^{1}H and ^{2}H (known as deuterium), and oxygen has the three aforementioned isotopes ^{16}O, ^{17}O, and ^{18}O. Any given water molecule could have one of nine possible combinations of hydrogen and oxygen isotopes; since heavier isotopes are very uncommon, the chance is very low that a water molecule will consist of more than one heavy isotope. The vapor pressure of a 'light' water molecule (e.g. $^{1}H_2^{16}O$) is higher than that of the 'heavy' water molecules, such that the light water molecule can escape from its liquid phase to gas phase more easily (Bradley, 1999, p. 129). The vapor pressure difference between light and heavy water molecules is the

fundamental reason for variation in δ^{18}O.

As a parcel of water in equilibrium with its vapor is evaporated, the vapor is enriched with $^{1}H_2^{16}O$, and the remaining liquid is enriched with the heavier $^{1}H_2^{18}O$. During condensation, the lower vapor pressure of $^{1}H_2^{18}O$ causes it to preferentially change to the liquid phase, such that the resulting condensate is enriched (i.e. in heavy oxygen isotopes) relative to the vapor (Bradley, 1999, p. 129). As condensation of a given air mass continues, the remaining air mass vapor becomes negative (otherwise termed 'light' or 'depleted') in ^{18}O relative to ^{16}O. This is a Rayleigh process if the exchange occurs at equilibrium (in the absence of kinetic effects) and the condensate is immediately removed from the system (Dansgaard, 1964; Jouzel, 1986). Continued condensation can occur as an air mass travels poleward, cools, and condenses, or as the air mass rises, cools adiabatically, and condensation occurs. The more cooling that the air mass experiences, the more condensation it will be subjected to, and the more depleted in ^{18}O relative to ^{16}O it will become.

There is a clear relationship between mean annual temperature (MAT) and $\delta^{18}O_{precip}$ in mid to high latitudes. Decreasing MAT lowers the $\delta^{18}O_{precip}$ by a linear function with a slope of approximately $0.7‰^{\circ}C^{-1}$ (Dansgaard, 1964). Dansgaard (1964) found the relationship for the extratropics to be $\delta^{18}O = 0.695T - 13.6$, which Jouzel et al. (1987a, 1994) refined to $\delta^{18}O = 0.64T - 12.8$ for latitudes with MAT less than 15°C. This T$-\delta^{18}$O relationship fails in the tropics where the balance of evaporation and precipitation, not MAT, dominates the δ^{18}O value. In the tropics the magnitude of precipitation controls the $\delta^{18}O_{precip}$ (Dansgaard, 1964). In addition, the relationship in the extratropics is not entirely linear, as the $\delta^{18}O_{precip}-$temperature slope is steeper (approximately $0.8‰^{\circ}C^{-1}$) in the coldest latitudes (Bradley, 1999, p. 135).

Considerable variation in $\delta^{18}O_{vapor}$ and $\delta^{18}O_{precip}$ occurs with latitude. This 'latitude effect' is principally related to decreasing temperatures at higher latitudes, and as such it is often referred to as an isobaric effect. Similar to the rainout effect, an air mass moving poleward will undergo repeated condensation events. While the rainout effect can occur for a constant temperature, the condensation events driving the latitude effect are driven by isobaric cooling. This causes the air mass to become depleted with respect to δ^{18}O with increasing latitude (Bradley, 1999, p. 134).

By causing an air mass to rise (or sink), changes in altitude lead to adiabatic cooling (or warming). Thus the altitude effect is also temperature driven. High elevation regions, such as the Andes in South America, strongly exhibit the altitude effect in $\delta^{18}O_{precip}$. The altitude effect can combine with the latitude effect and

rainout effect, producing the worlds most depleted $\delta^{18}O_{vapor}$ and $\delta^{18}O_{precip}$ in central Antarctica (Qin et al., 1994).

Atmospheric variation in $\delta^{18}O$ may be further affected by local or second-order effects. If the air mass moisture source is not the ocean, but rather an inland lake or continental ice sheet, the initial $\delta^{18}O$ will be depleted relative to sea water (Bradley, 1999, p. 132).

A.3 Variability in Snow and Ice $\delta^{18}O$

The isotopic composition of snow (and by extension, ice) is governed by the same processes controlling precipitation, described in the preceding section. Snow $\delta^{18}O$ (or $\delta^{18}O_{snowfall}$) is also well correlated with the temperature of the precipitation cloud (Bradley, 1999, p. 139).

Because summer snow is warmer than winter snow, a seasonal signal can be found in snow (and ice cores) given sufficiently high accumulation: $\delta^{18}O_{snowfall}$ is more negative in winter than in summer. The amplitude of the seasonal cycle attenuates with depth in an ice core due to processes involving isotopic exchange and molecular diffusion (Bradley, 1999, p. 143).

The interpretation of $\delta^{18}O$ in an ice core must take into consideration all of the processes described above and in the preceding section (i.e. what determines the $\delta^{18}O$ of snowfall), but is complicated by ice flow. As ice flows, it transports its isotopic properties. Ice flow can introduce large uncertainties to the dating of individual layers. The oldest ice is eventually transported to the margins of the ice sheet. For example, the ice divide of the ice sheet - the coldest, highest, and furthest-inland point - will accumulate the most negative snow. This ice will flow away from the ice divide, towards the ice sheet margins, and all downslope ice core locations will contain this older ice with an altitude effect requiring correction (Bradley, 1999, p. 151-152).

Associated with ice cores are the gas bubbles containing air samples of approximately the age of the ice layer. The $\delta^{18}O$ measured in these bubbles ($\delta^{18}O_{ATM}$) is representative of the bulk isotopic composition of the atmosphere, which is determined by the ocean isotopic composition at that time ($\delta^{18}O_w$), which is in turn set by the global ice volume (Bradley, 1999, p. 184). Because ice volume also dominates the benthic marine $\delta^{18}O$ record, $\delta^{18}O_{ATM}$ from ice cores can be correlated with marine $\delta^{18}O_{benthic}$. Processes acting upon the marine $\delta^{18}O_{benthic}$ composition will be

presented in the following section. It should be noted here only that the $\delta^{18}O_{ATM}$ record is distinct from the $\delta^{18}O_{snowfall}$ (and from $\delta^{18}O_{ice}$ and $\delta^{18}O_{precip}$) despite its ice core origin.

A.4 Variability in Seawater $\delta^{18}O$

The dominant influence on the bulk isotopic composition of oxygen in seawater ($\delta^{18}O_w$) is global ice volume. $\delta^{18}O$ mainly varies within the ocean based on the relative contributions of temperature and salinity (or evaporation-precipitation) effects on the source water. Modern sea surface $\delta^{18}O$ ranges from $-4‰$ to $+2‰$ over most of the global ocean (LeGrande and Schmidt, 2006). Previous researchers have described seawater $\delta^{18}O$ - globally, by basin, or regionally - as a function of salinity. $\delta^{18}O_w$ can be described in terms of salinity because both fluctuate with freshwater fluxes (Craig and Gordon, 1965). For example, Broecker (1979) estimated $\delta^{18}O_w = 0.5S - 17.12$ for the global ocean. One local effect of note is the input of very depleted freshwater via rivers to ocean regions near continental margins - this is known as the 'dilution effect'.

By storing large amounts of depleted water on land, high ice volume results in enriched sea water. The relationship between $\delta^{18}O$ and ice volume, however, is not necessarily linear. As ice volume increases, ice accumulates at higher ice sheet elevations, where it is isotopically lighter due to the altitude effect. If ice volume were to remain constant at this stage, with new ice added with very light values at the summit, and older ice with heavier values (deposited at lower elevations) removed from the ice sheet margins, the system would be at steady state with respect to ice volume, but seawater $\delta^{18}O$ would increase (Mix and Ruddiman, 1984).

A.5 Variability in Biogenic Calcite $\delta^{18}O$

Marine organisms that secrete calcium carbonate shells (tests) are the primary recorder of the isotopic composition of the ocean. The organisms incorporate the seawater ^{18}O and ^{16}O into their shells during calcification. Analyzing the $\delta^{18}O$ in foraminiferal calcite from regions where climatic events could produce a large signal is a standard approach in paleoclimate investigations. For example, planktic foraminifera living in a meltwater discharge region record meltwater pulse events as large negative excursions (ice sheet $\delta^{18}O$ meltwater values of $< -30‰$ would produce a discernible

signal on sea water, which is normally near 0‰) (Ruddiman, 2001, p. 306). Benthic foraminifera from the tropical Pacific (where meltwater events do not penetrate) are characterized by an isotopic value predominantly determined by global ice volume (Ruddiman, 2001, p. 338).

Urey (1947, 1948) first hypothesized that the δ^{18}O in the shells of ocean dwelling organisms would follow from thermodynamic principles applied to (inorganic) precipitation of calcium carbonate in sea water. Instead, Urey discovered a 'vital effect', whereby the calcite oxygen isotopic signature ($\delta^{18}O_c$) is in fact lower than the expected value (i.e. higher ^{18}O relative to seawater). Because living organisms consume energy and produce metabolic CO_2, it is not required that they secrete calcium carbonate in equilibrium conditions (Duplessy et al., 1970; Shackleton and Opdyke, 1973; Vinot-Bertouille and Duplessy, 1973). The magnitude of this vital effect varies by species, and depends on to what extent the species incorporates its metabolically-produced carbon dioxide in its shell (Grossman, 1987). One foraminifera species, *Globigerinoides ruber*, is approximately -0.5‰ from equilibrium (Shackleton and Opdyke, 1973), while another species *Pulleniatina obliquiloculata* secretes a shell at equilibrium with respect to sea water δ^{18}O (Shackleton, 1974). It is crucial to understand species level dynamics in order to interpret raw δ^{18}O measured in foraminiferal calcite: if unaccounted for, the -0.5‰ shift found in *Globigerinoides ruber* would translate into a 2.5°C difference in the estimated temperature (Bradley, 1999, p. 200).

Other complications arise from analyzing the δ^{18}O in shells of once-living organisms - specifically, the fact that an organism does not reside at constant depth for its entire life cycle. This is especially important for interpreting planktic (surface-dwelling) $\delta^{18}O_c$, as large temperature gradients may exist near the surface. A small change in depth can result in a large temperature driven δ^{18}O signal (Bradley, 1999, p. 201-202). Many foraminiferal species prefer to reside at a certain density level, and a change in either temperature or salinity will compel the organism to migrate vertically. Considering an interglacial-glacial transition, terrestrial ice storage would have increased the ocean salinity, and foraminifera may have migrated upwards to warmer water to maintain a constant density (Bradley, 1999, p. 202). The resulting interglacial-glacial $\delta^{18}O_c$ signal would therefore be muted (Savin and Stehli, 1974). Besides vertical migration driven by density preferences, foraminifera may move vertically in the water column due to other, life cycle motivations. For example, some species descend below the mixed layer for reproduction, and subsequently become enriched in δ^{18}O (Duplessy et al., 1981). Foraminifera are diverse, varying in the ex-

tent to which metabolic CO_2 is utilized in their calcite tests, in their depth or density habitat preferences, and in life cycle behavior. The interpretation of $\delta^{18}O_c$ includes the consideration of multiple factors.

A.6 Summary

In this section I have reviewed the main mechanisms affecting the distribution of stable water oxygen isotopes in sectors of the climate system - atmosphere, ocean, and cryosphere - as well as the biological mechanisms affecting the $\delta^{18}O$ record found in marine sediments. The relative distributions of oxygen isotopes in time and space can be used to interpret the physical (and biological) processes that caused their distribution, therefore informing us about past climate. While there are multiple and sometimes complicated factors to consider, the resulting data, once interpreted, are invaluable to reconstructing past climate.

Appendix B

Oxygen Isotope Model Equations and Testing

B.1 Isotope modelling details

The equations employed in the oxygen isotope enabled UVic ESCM consist of:

1. Calculation of fractionation factors;
2. Calculation of $H_2^{18}O$ moisture fluxes (for evaporation, precipitation, runoff, etc.);
3. Adjusting atmospheric $H_2^{18}O$ moisture transport over elevation, described in Section 3.2.4.

All expressions for the equilibrium and kinetic fractionation factors (α_{eq} and α_{kin}, respectively) are presented in Table 3.1, along with the equations governing the isotopic content (as the ratio of $H_2^{18}O$ to $H_2^{16}O$, or R_x) within each moisture flux x.

$H_2^{18}O$ moisture fluxes (for evaporation, precipitation, runoff, etc.) are depicted in the model schematic (Fig. 3.2), and take the form $F_{H_2^{18}O} = R \cdot F_{H_2^{16}O}$. For a moisture quantity x (x represents runoff, evaporation, etc.):

$$F_x^{H_2^{18}O} = R_x F_x = \frac{H_2^{18}O_x}{H_2^{16}O_x} F_x \tag{B.1}$$

B.1.1 Precipitation

When condensation occurs in the model, the ratio of oxygen isotopes in atmospheric water vapor, R_{vap} is enriched by the temperature-dependent equilibrium fractionation

factor, α_{eq}. The temperature is the surface air temperature adjusted for elevation by the atmospheric model lapse rate. As detailed in Table 3.1, the specific formulation for the fractionation factor depends on temperature: the vapor-liquid α_{eq} is employed at and above -10°C, the vapor-solid α_{eq} below -10°C, and an additional kinetic isotopic effect (discussed below) determines the effective fractionation below -20°C.

Here it is noted that fractionation processes and supersaturation over ice crystals are continuous processes, and the selection of a specific temperature at which conditions change from all vapour-liquid to entirely vapour-solid may be a severe simplification. Future work with the UVic model should consider a treatment of α_{eq} that takes continuous processes into account, perhaps following the implementation of Sinclair et al. (2011), which assumes mixed-phase conditions between 0° and -20°C. It is possible that the representation of low-temperature fractionation under mixed-phase conditions could improve the simulated precipitation δ^{18}O in mid and high latitudes.

The expression for α_{eq} is given in Table 3.1, which shows that as temperature increases, α_{eq}, and thus fractionation, decreases. This is demonstrated in the left panel of Figure B.1, where the equilibrium fractionation factor is calculated for a range of temperature values. The isotopic content of precipitation is plotted in the right panel of Figure B.1 for a constant atmospheric water vapor δ^{18}O value (-20‰). α_{eq} is always greater than one: across the -30 to $+30$°C domain, α_{eq} ranges from 1.0090 to 1.0185. Consequently, $\delta^{18}O_{precip}$ is always enriched relative to the atmospheric water vapor from which it condenses.

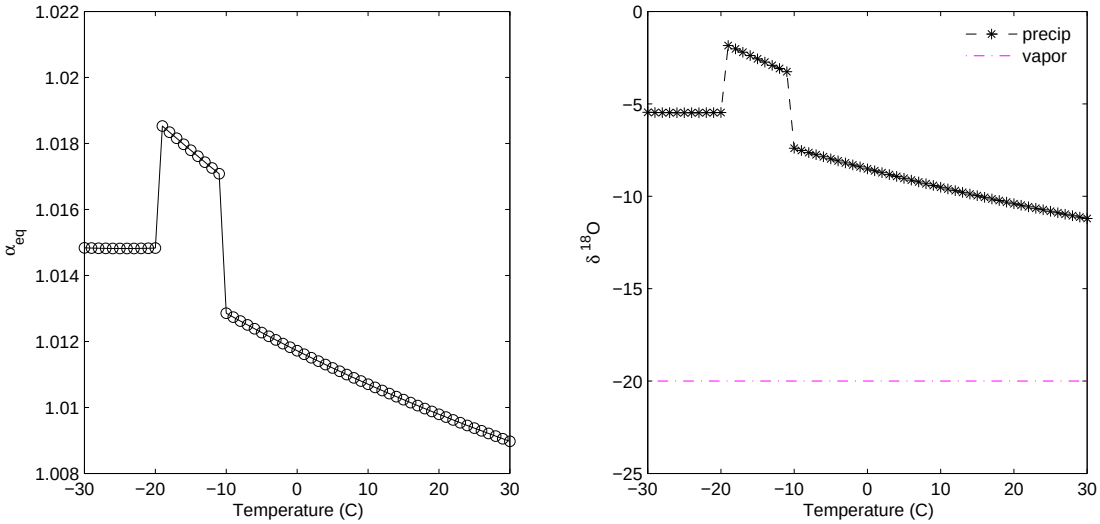

Figure B.1: Equilibrium fractionation factor (α_{eq} (left) and isotopic fractionation (right) for the vapor-liquid and vapor-solid phase change with respect to temperature. $\delta^{18}O_{vapor}$ is held constant at $-20‰$ in the isotopic fractionation example.

B.1.2 Evaporation

The isotopic content of evaporation from the sea surface (see R_e in Table 3.1) is dependent upon multiple variables: sea surface temperature (T, found in the determination of equilibrium fractionation factor α_{eq}), relative humidity (h), the isotopic gradient at the air-sea interface ($R_{oc} - R_{vap}$), and a kinetic isotope effect (the ratio of effective resistances for $H_2^{18}O$ and $H_2^{16}O$, $\frac{\rho_i}{\rho}$). The impact of the first three of these is demonstrated in Figure B.2, where for a scenario of $T = 5°C$, $\delta^{18}O_{oc} = 0‰$, $\delta^{18}O_{vap} = -10‰$, and $h = 0.85$, relative humidity, isotopic gradient and temperature are varied individually.

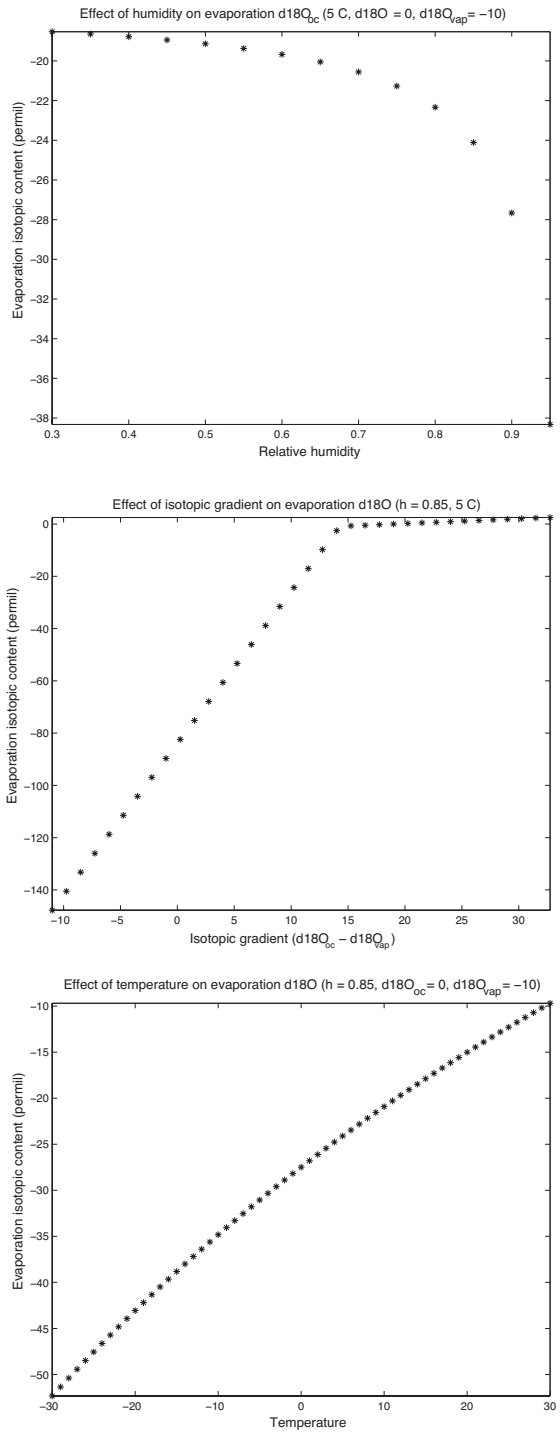

Figure B.2: Effect of humidity, the isotopic gradient at the air-sea interface, and temperature on the isotopic content of evaporate. The calculations employ a scenario of $T = 5°\mathrm{C}$, $\delta^{18}\mathrm{O}_{oc} = 0‰$, $\delta^{18}\mathrm{O}_{vap} = -10‰$, and $h = 0.85$, and the variables relative humidity (top), isotopic gradient (center) and temperature (bottom) are varied individually. Note that y-axis scales differ.

The annual average fields of the isotopic content in evaporation and atmospheric water vapor are shown in Figure B.3.

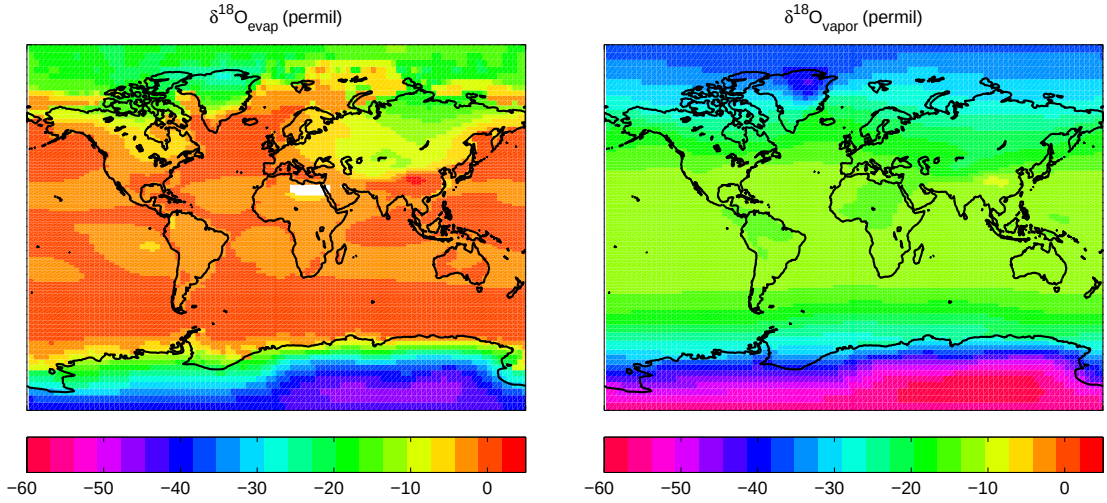

Figure B.3: δ^{18}O in evaporation and atmospheric water vapor. Annual average preindustrial δ^{18}O in evaporation (left) and vapor (right) simulated by the UVic model.

At 100% relative humidity, the system would theoretically produce equilibrium exchange, with no kinetic isotope effects. Larger fractionation (and more depleted evaporate) is produced from conditions corresponding to higher humidity, lower values of the ocean-atmosphere isotopic gradient ($\delta^{18}O_{oc} - \delta^{18}O_{vap}$), and lower temperature. Practically, however, model relative humidity over marine points is essentially constant ($h = 0.85$), while the ocean-atmosphere isotopic gradient typically ranges from +10 to +12 at tropical and subtropical points to more than +30 at some high latitude locations.

Because most of the variation is in $\delta^{18}O_{vap}$ (relative to $\delta^{18}O_{oc}$), a highly positive isotopic gradient corresponds to more depleted $\delta^{18}O_{vap}$. In this case, the effective resistance for $H_2^{18}O$ moving towards the open atmosphere and away from the air-sea interface is very high. This is represented in the model by the condition that fractionation occurs during evaporation only if the isotopic gradient is less than the quantity $\frac{\varepsilon}{h}$, where

$$\varepsilon = (1 - \alpha_{eq}) \cdot 1000 + (1 - h) \cdot (\frac{\rho_i}{\rho} - 1) \tag{B.2}$$

The ratio of effective molecular resistances for $H_2^{18}O$ and $H_2^{16}O$ is given by $\frac{\rho_i}{\rho}$ (Craig

and Gordon, 1965). When the isotopic gradient exceeds this limit, then for the purposes of calculating the isotopic content of the evaporate the atmospheric vapor δ^{18}O is adjusted to $\frac{-\varepsilon}{h}+\delta^{18}O_{oc}+$ (a small number) such that fractionation is negligible. This effect is discernible in Figure B.2's scenario by the change in gradient-$\delta^{18}O_{evap}$ slope near the isotopic gradient of +15‰. $\delta^{18}O_{evap}$ is subsequently calculated:

$$\delta^{18}O_{evap} = \frac{\alpha_{eq}^{-1} \cdot \delta^{18}O_{oc} - h \cdot \delta^{18}O_{vap} - \varepsilon}{1 - h + (1 - h) \cdot (\frac{\rho_i}{\rho} - 1) \cdot (1 \times 10^{-3})} \tag{B.3}$$

B.2 Additional model testing

The largest fractionation of isotopes occurs during evaporation and condensation. This, combined with the fact that the UVic ESCM atmosphere is highly simplified (i.e. a 2-dimensional atmosphere with vertically-integrated equations for heat and moisture balance), explains why it is most instructive to evaluate the model's response to varying the parameterizations employed during evaporation and formation of precipitation in the model. As model $\delta^{18}O_{precip}$ was initially not sufficiently depleted over high-elevation land points (when compared to observations), the effect of adjusting diffusion of $H_2^{18}O$ relative to $H_2^{16}O$ during the transport of atmospheric moisture, as described in Section 3.2.4, is also assessed. Table B.1 presents the experiments conducted in model testing.

Table B.1: List of experiments.

Experiment	**Description**
CONDH	Vary height at which atmospheric precipitation is assumed to form.
VAPSOLID	Vary temperature limit for vapor-solid equilibrium fractionation.
SICE	Evaluate effect of including a kinetic isotope effect during low temperature vapor-solid phase changes.
O18EVAP	Vary fractionation during evaporation from sea surface.
O18DIFFR	Vary amount by which the diffusion of $H_2^{18}O$ in atmospheric moisture transport is reduced over elevation.

B.2.1 Atmospheric condensation height (CONDH)

Precipitation amount depends on the specific humidity calculated using surface air temperature (adjusted by a model lapse rate for elevation) in the UVic ESCM. The

assumption of condensation occurring at surface temperature needs to be examined for the representation of oxygen isotopes, since ground-level condensation occurs at a warmer temperature than what would be measured at a cloud base 2 or 3 km above the surface.

The aim of the CONDH experiments is to assess to what extent the default ground-level condensation affects the resulting distribution of isotopes in atmospheric water vapor and precipitation. In this experiment, condensation height is set as either a constant value (at 0 km (control) and 8 km), or with latitude dependence between 10 km at equator and 1 km at poles. The linear function for the condensation height (*condh*, in m) variation with latitude (θ (degrees)) is denoted as $f(\text{lat})_{lin}$, and given by:

$$f(lat)_{lin} : condh = 10^4 - 10^2|\theta| \tag{B.4}$$

The non-linear function is denoted as $f(\text{lat})_{nonlin}$, and given by:

$$f(lat)_{nonlin} : condh = 9 \times 10^3 cos(\theta \frac{\pi}{180}) + 10^3 \tag{B.5}$$

Results for 0 km (control), 8 km, and with linear and non-linear latitude dependence are shown in Figures B.4 and B.5, and summarized in Table B.2.

Table B.2: Experimental results. The experiments are listed in the first column, with the parameter to be varied in parentheses. Parameter values are given in the second column. The mean value of precipitation δ^{18}O ($\overline{\delta^{18}O_p}$), and the difference between the mean value and the control ($\Delta\overline{\delta^{18}O_p}$) are listed in the third and fourth columns, respectively. The last column gives the minimum and maximum annual mean values for δ^{18}O in model precipitation.

		$\overline{\delta^{18}O_p}$ (‰)	$\Delta\overline{\delta^{18}O_p}$ (‰)	$\delta^{18}O_p^{min} : \delta^{18}O_p^{max}$ (‰)
CONDH ($condh$)	0 km	-6.2	–	$-19.6 : -2.2$
	8 km	-6.6	-0.4	$-34.0 : 7.1$
	$f(\text{lat})_{lin}$	-5.0	$+1.2$	$-25.0 : 10.2$
	$f(\text{lat})_{nonlin}$	-6.7	-0.5	$-32.4 : 9.5$
VAPSOLID ($T_{vap-solid}$)	-10°C	-7.5	–	$-47.1 : 4.4$
	0°C	-7.6	-0.1	$-48.6 : 5.4$
SICE ($include$)	*yes*	-7.5	–	$-47.1 : 4.4$
	no	-7.3	0.2	$-44.5 : 4.4$
O18EVAP (f)	0%	-7.5	–	$-47.0 : 4.4$
	-0.5%	-10.8	-3.3	$-50.1 : 1.6$
	-1%	-15.7	-8.2	$-55.5 : -3.4$
	-2%	-25.6	-18.1	$-65.0 : 13.4$
	-3%	-35.5	-28.0	$-74.6 : -23.5$
O18DIFFR (X)	0	-8.4	–	$-23.2 : -2.4$
	5×10^2	-8.8	-0.4	$-25.4 : -2.4$
	1×10^3	-9.2	-0.8	$-29.4 : -2.4$
	2×10^3	-10.1	-1.7	$-38.5 : -1.3$
	4×10^3	-11.8	-3.4	$-57.6 : 2.8$

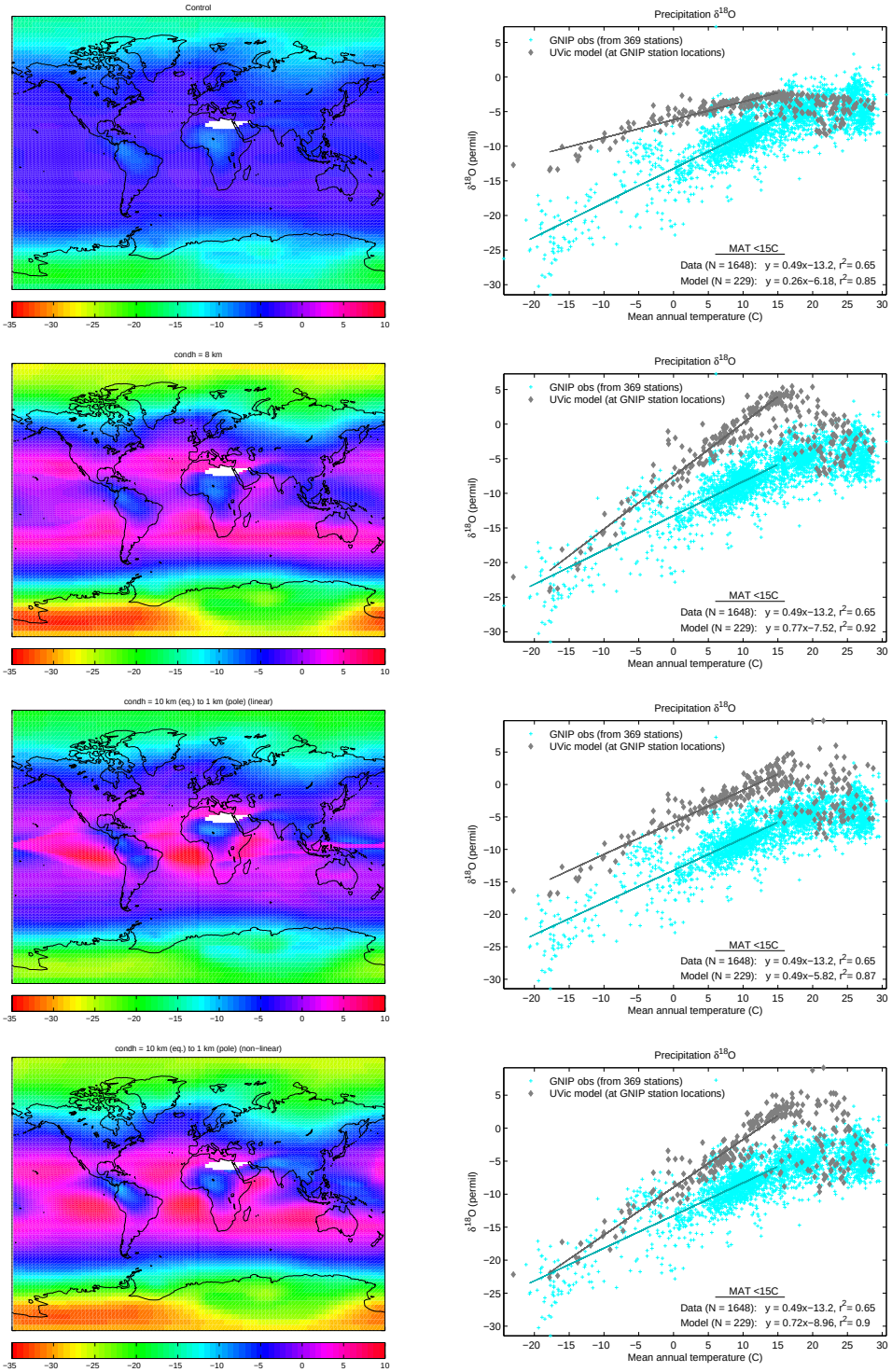

Figure B.4: Impact of condensation height on precipitation δ^{18}O. Mean annual $\delta^{18}O_{precip}$ is mapped (left) and plotted against mean annual temperature (right) for condensation height at 0 km (control), 8 km, and with linear and non-linear latitude dependence between 10 km at equator and 1 km at poles (top to bottom, respectively).

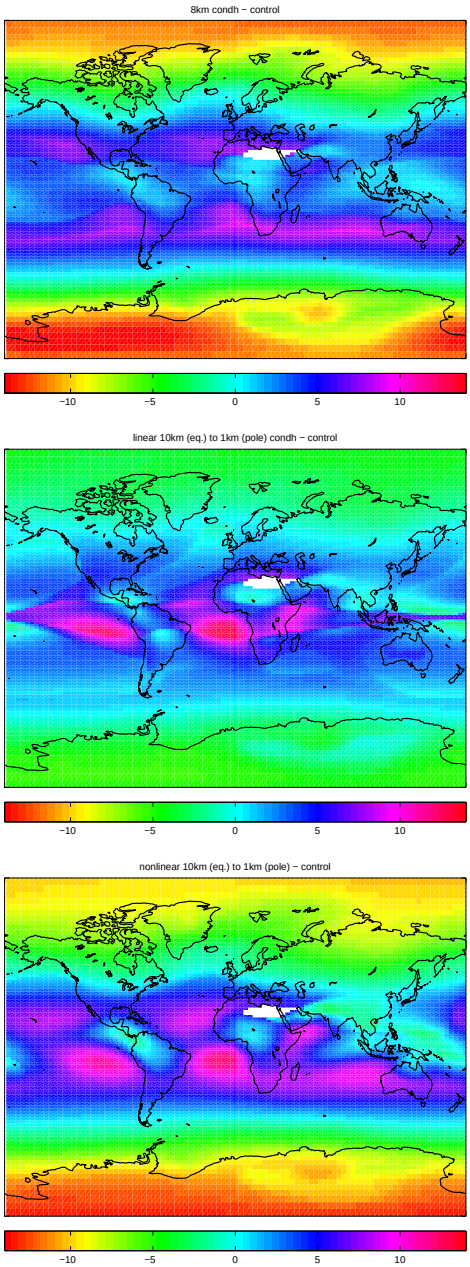

Figure B.5: Change in annual mean precipitation δ^{18}O due to varying condensation height. Mean annual $\Delta\delta^{18}O_{precip}$ (permil) (simulation − control) is mapped for condensation height at 8 km, and with linear and non-linear latitude dependence between 10 km at equator and 1 km at poles (top to bottom, respectively).

Increasing condensation height in the model produces greater enrichment (or positive values) at lower latitudes and greater depletion at higher latitudes (Fig. B.4 and B.5). This redistribution of $H_2^{18}O$ within the atmosphere is observed in the

MAT$-\delta^{18}$O relationship (Fig. B.4): the slope varies around an approximately constant central tendency. The conclusion is that altering condensation height does not improve the modeled distribution of oxygen isotopes. Therefore, changes in condensation height are not adopted.

B.2.2 Temperature limit for fractionation in vapor-solid phase change (VAPSOLID)

Precipitation falls as snow in the model when the surface air temperature falls below 0°C. In the VAPSOLID experiment, the temperature boundary between the vapor-liquid versus vapor-solid phase change with respect to isotopic fractionation is explored. The vapor-solid transition occurs when the surface air temperature falls below a certain limit. VAPSOLID tests the effect of setting this temperature limit to 0°C or, following other isotope-enabled models, to −10°C.

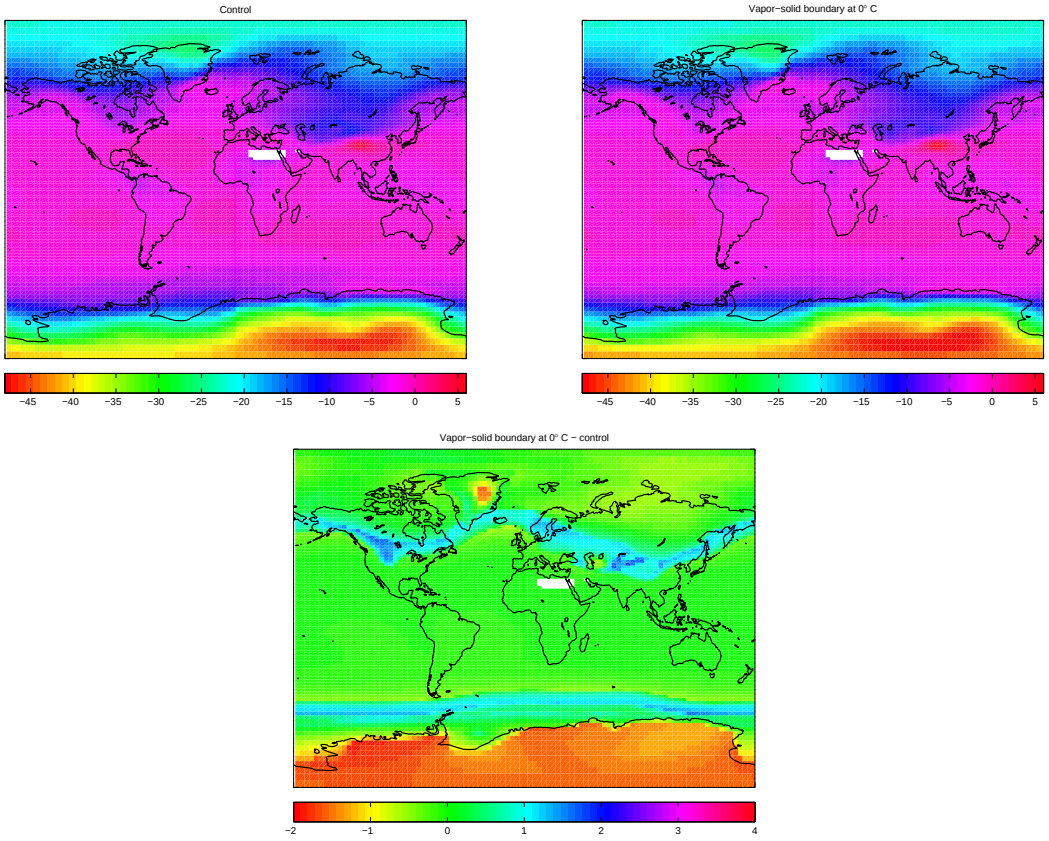

Figure B.6: Effect of the vapor-solid temperature boundary on precipitation δ^{18}O. Mean annual $\delta^{18}O_{precip}$ is mapped for the boundary at -10°C (corresponding to the control) (top left), and for the boundary at 0°C (top right). The $T^{0°C}_{vap-sol}$ - control anomaly is mapped in the lower plot.

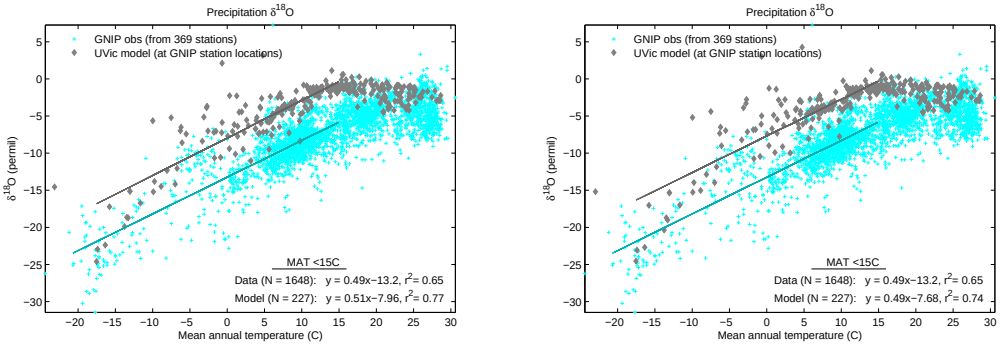

Figure B.7: Effect of the vapor-solid temperature boundary on MAT − precipitation δ^{18}O relationship. Mean annual $\delta^{18}O_{precip}$ (‰) is plotted against mean annual temperature for the control simulation (left), and for a vapor-solid temperature boundary of 0°C (right).

When the temperature of the vapor-solid boundary is set at 0°C as opposed to the value of −10°C used in other isotope-enabled models, there are two main consequences. First, a mid-latitude enrichment of approximately +1 is found in both hemispheres in the regions corresponding to the mean annual 0° isotherm. Second, a small depletion (on the order of 1.5‰) results over high latitude, high elevation regions in Antarctica and Greenland corresponding to the −10°C isotherm (Fig. B.6). There is no detectable difference in the relationship between MAT and $\delta^{18}O_{precip}$ for these simulations (Fig. B.7). As the isotopic shifts are small, it seems ideal to retain the same vapor-solid temperature boundary employed across models, and the $T_{vap-solid}$ remains −10°C in the UVic ESCM.

B.2.3 Inclusion of kinetic isotope effect for low temperature vapor-solid phase change (SICE)

Jouzel and Merlivat (1984) identified an offset between δ^{18}O observed in polar snow versus that calculated using an assumption of equilibrium fractionation, and determined the cause to be an isotope kinetic effect during low-temperature (< −20°C) vapor deposition due to supersaturation with respect to ice. Other isotope-enabled models typically include this kinetic effect, which at colder temperatures produces a slightly reduced fractionation relative to what occurs for vapor-solid exchange under equilibrium conditions. This is seen in Figure B.1. The SICE experiment includes simulations with and without the kinetic effect. The kinetic effect is applied when

model surface air temperature falls below −20°C. As shown in Table 3.1, the effective fractionation is equivalent to the equilibrium fractionation factor multiplied by the kinetic fractionation factor ($\alpha_{eq} \cdot \alpha_{kin}$), and depends on the temperature-dependent supersaturation parameterization, S_{ice} (Jouzel et al., 1987b), as well as the ratio of isotope molecular diffusivities.

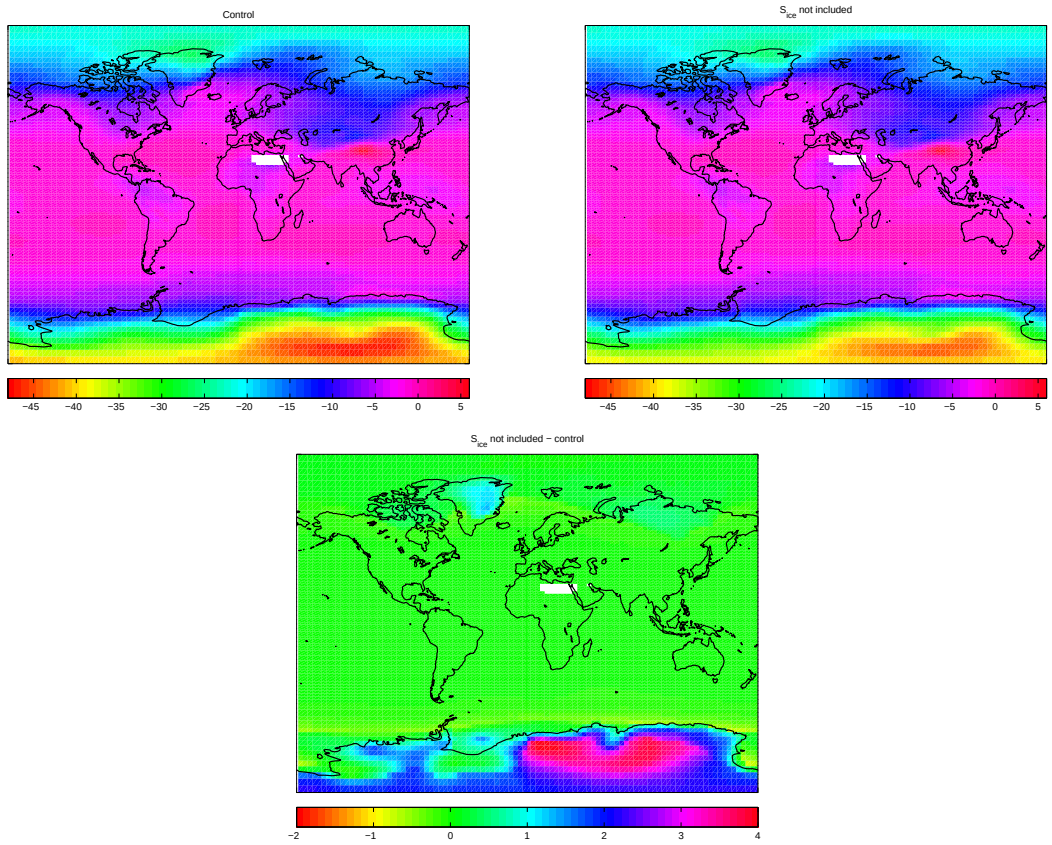

Figure B.8: Effect of the low-temperature isotope kinetic effect on precipitation δ^{18}O. Mean annual $\delta^{18}O_{precip}$ (‰) is mapped for the control simulation including S_{ice} (top left), and when S_{ice} is neglected (top right). The no S_{ice} - control anomaly is mapped in the lower plot.

It is clear from Figure B.8 that including S_{ice} in the model produces more depleted $\delta^{18}O_{precip}$ in Greenland (by > 1‰) and Antarctica (by up to 4‰), and these are the only affected regions. S_{ice} is retained in the model description of precipitation, as this choice is both in line with other models and improves the model distribution of $\delta^{18}O_{precip}$.

B.2.4 Fractionation during evaporation from sea surface (O18EVAP)

The goal of the O18EVAP experiments is to assess the impact of increasing kinetic fractionation during evaporation from the sea surface on the overall distribution of oxygen isotopes in the model. This is achieved by scaling $H_2^{18}O$ in the calculated evaporate by the factor y, such that:

$$F_{evap}^{H_2 18O} = y \cdot F_{evap}^{H_2 18O} \tag{B.6}$$

$$y = 1 + f \tag{B.7}$$

, and f takes on values of 0 (default), -0.005, -0.01, -0.02, and -0.03, which correspond to scaling the evaporative $H_2^{18}O$ flux by 0%, -0.5%,-1%, -2%, and -3%.

Results from the control simulation and the simulation with evaporate $H_2^{18}O$ scaled by -0.5%, -1%, and -2% are shown in Figures B.9 and B.10, and presented in Table B.2.

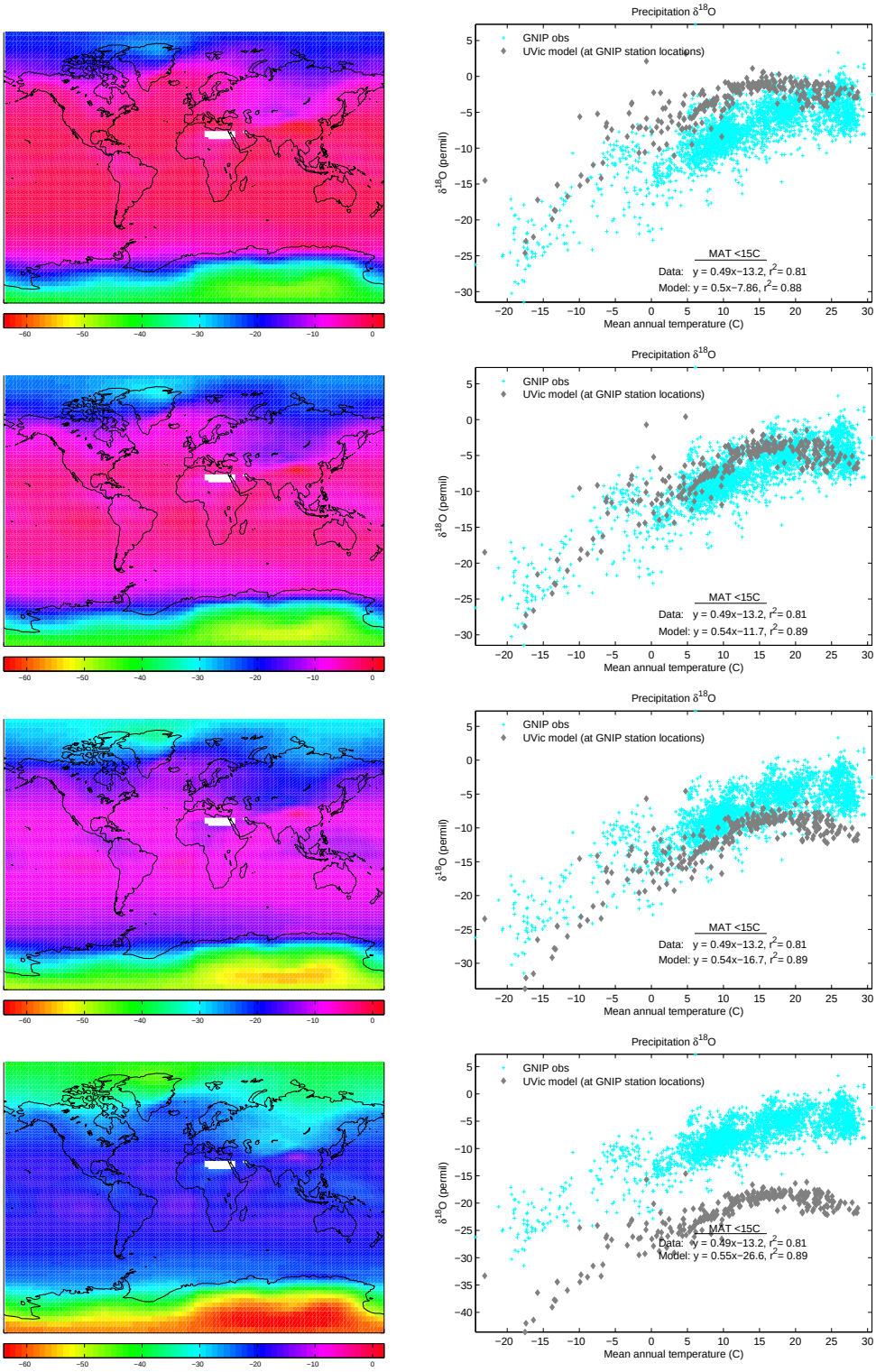

Figure B.9: Impact of evaporation fractionation on precipitation δ^{18}O. Mean annual $\delta^{18}O_{precip}$ is mapped (left) and plotted against mean annual temperature (right) in the control, -0.5%, -1%, and -2% simulations (top to bottom, respectively).

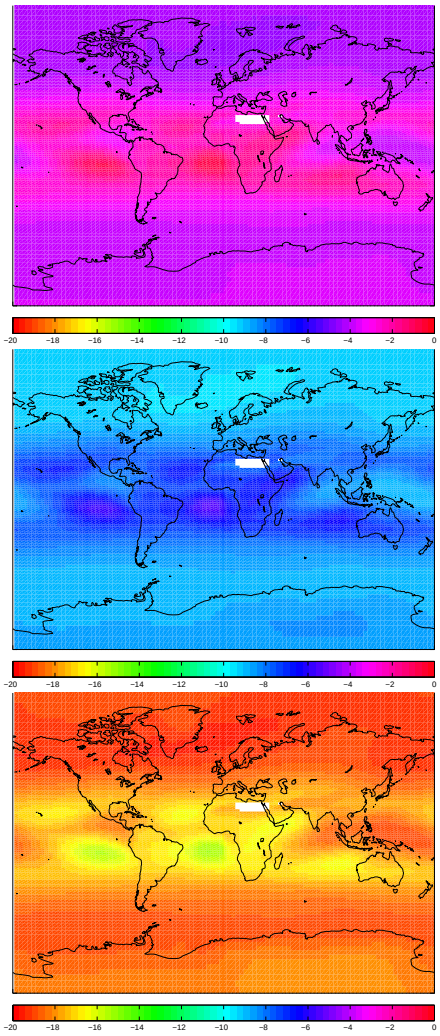

Figure B.10: Change in annual mean precipitation δ^{18}O due to varying isotope fractionation in evaporation. Mean annual $\Delta\delta^{18}O_{precip}$ (permil) (simulation − control) is mapped for the -0.5%, -1%, and -2% simulations (top to bottom, respectively).

Figure B.9 demonstrates that by increasing the scaling factor f, the mean value of $\delta^{18}O_{precip}$ decreases, resulting in more depleted precipitation at all latitudes. This is also seen in the differences relative to the control in Figure B.10. The MAT$-\delta^{18}O_{precip}$ relationship reveals this bulk depletion: relative to the observations, the model values are offset downwards towards negative $\delta^{18}O_{precip}$, while the shape of the relationship does not vary greatly between simulations. This result indicates that adjusting the evaporation isotopic fractionation changes the ocean-atmosphere isotopic partitioning. While this result is instructive, no modification or scaling of isotopic fractionation during evaporation from the sea surface is implemented in the model.

B.2.5 $H_2^{18}O$ diffusion in atmospheric moisture transport (O18DIFFR)

As described in Chapter 3 (Section 3.2.4), $\delta^{18}O_{precip}$ was originally not sufficiently depleted over high-elevation land points, compared to observations. The impact of adjusting the diffusion of $H_2^{18}O$ during atmospheric moisture transport is evaluated in the O18DIFFR experiments. Where *o18diffr* is the absolute reduction in the meridional moisture diffusion coefficient, *dn*, and the zonal moisture diffusion coefficient, *de*, is scaled accordingly, such that:

$$dn(H_2^{18}O) = dn(H_2^{16}O) - o18diffr \tag{B.8}$$

$$de(H_2^{18}O) = de(H_2^{16}O) - o18diffr \cdot \frac{de(H_2^{16}O)}{dn(H_2^{16}O)} \tag{B.9}$$

Both *dn* and *de* are limited to values greater or equal to zero. The expression for *o18diffr* takes the form:

$$o18diffr = X \cdot elev(i,j) \tag{B.10}$$

In the O18DIFFR experiments, the quantity X is set to: 0 (default), 5×10^2, 1×10^3, 2×10^3, and 4×10^3.

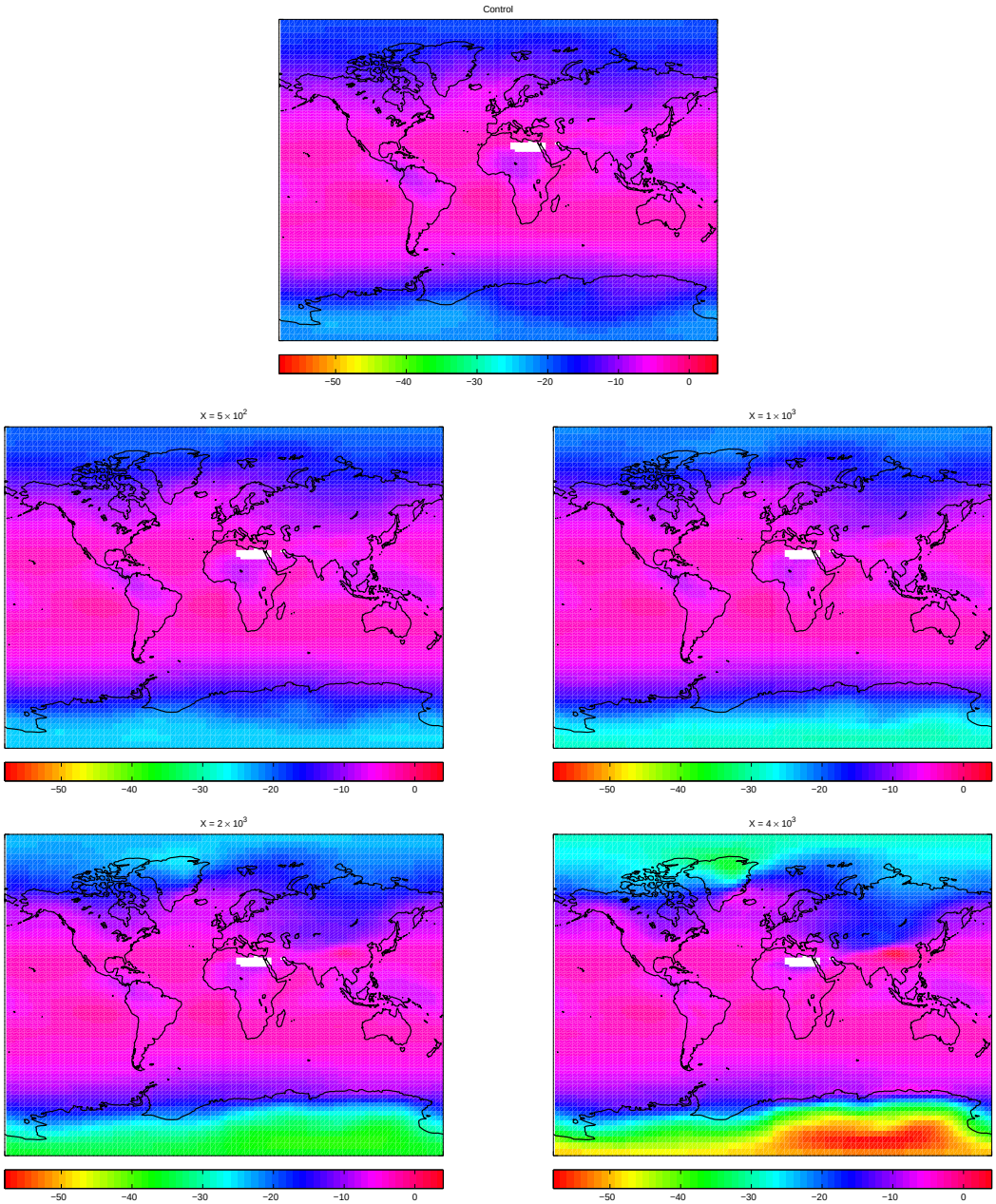

Figure B.11: Effect of varying atmospheric $H_2^{18}O$ diffusion over elevation on precipitation $\delta^{18}O$. Mean annual $\delta^{18}O_{precip}$ is mapped for $X = 0$ (top), 5×10^2 (center left), 1×10^3 (center right), 2×10^3 (bottom left), and 4×10^3 (bottom right).

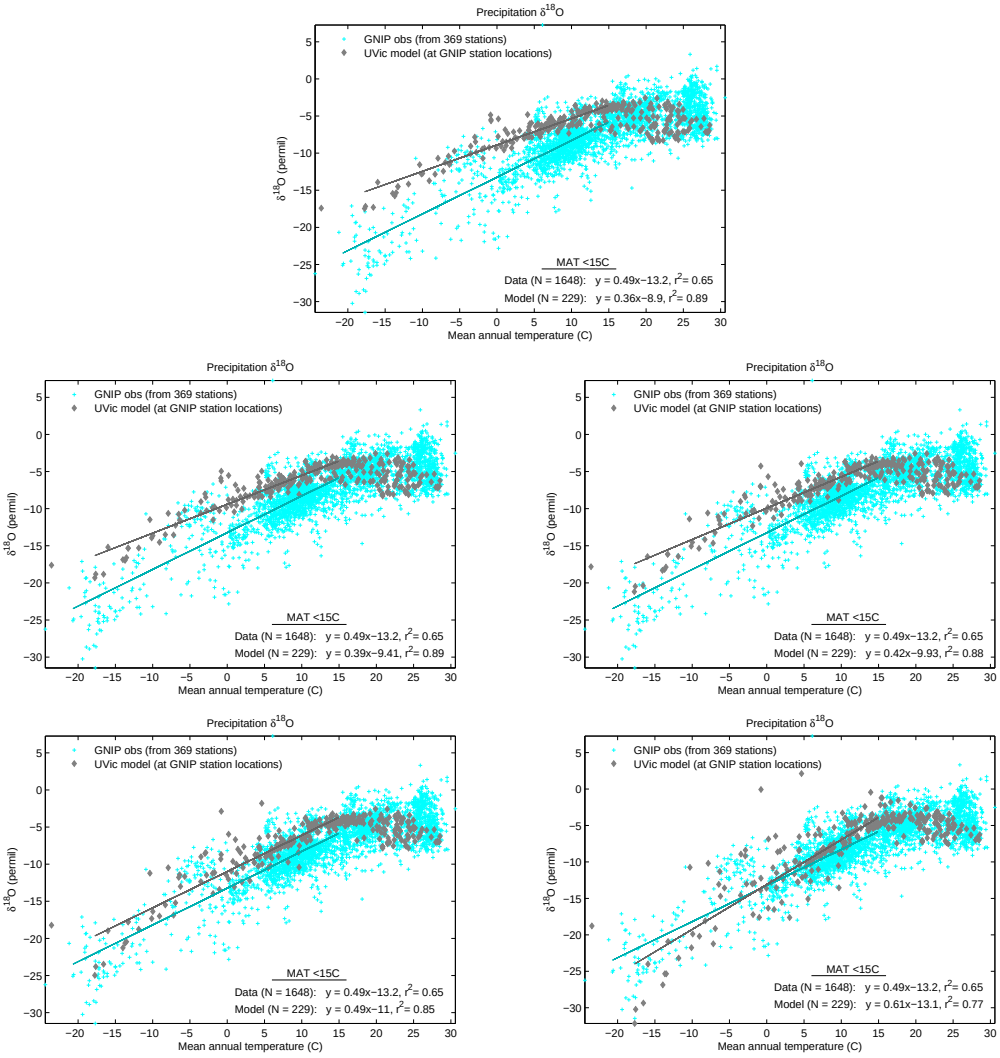

Figure B.12: Effect of varying atmospheric $H_2^{18}O$ diffusion over elevation on MAT − precipitation $\delta^{18}O$ relationship. Mean annual $\delta^{18}O_{precip}$ is plotted against mean annual temperature for $X = 0$ (top), 5×10^2 (center left), 1×10^3 (center right), 2×10^3 (bottom left), and 4×10^3 (bottom right).

Figures B.11 and B.13 demonstrate that as X increases, $\delta^{18}O_{precip}$ becomes increasingly depleted over high latitude regions. The largest decreases are found at and poleward of the highest elevation points in Eastern Antarctica and central Greenland. Since low latitude points are largely unaffected (with the exception of the region corresponding to the Himalaya Mountains in Asia), the MAT−$\delta^{18}O$ slope steepens with increasing X as well. $X = 3 \times 10^3$ is implemented in the UVic ESCM.

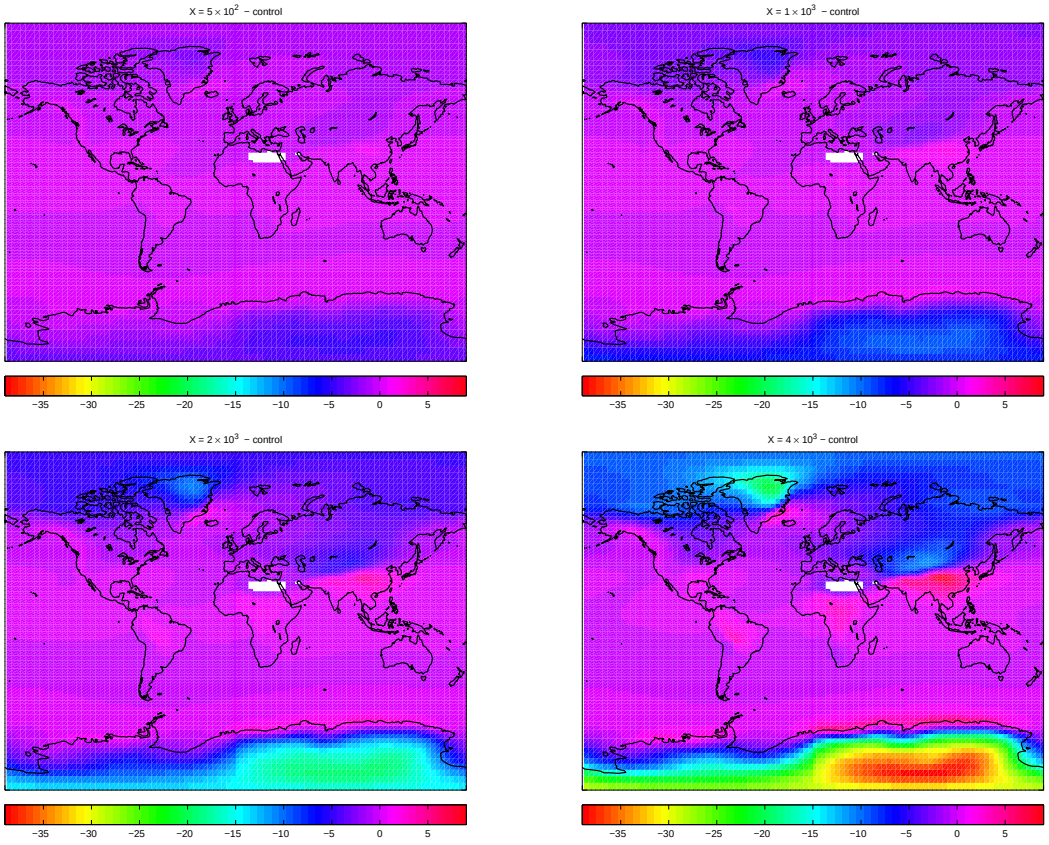

Figure B.13: Change in annual mean precipitation δ^{18}O due to varying the atmospheric $H_2^{18}O$ diffusion coefficient. Mean annual $\Delta\delta^{18}O_{precip}$ (permil) (simulation − control) is mapped for $X = 5 \times 10^2$ (top left), 1×10^3 (top right), 2×10^3 (center left), and 4×10^3 (center right).

Appendix C

Simulated Sea Ice Variability: Supplemental Information

Sea ice simulated under preindustrial and LGM conditions is the subject of the paleoclimate model investigation presented in Chapter 4. Additional sea ice variability findings are presented in this Section.

The model simulates differences in interglacial versus glacial sea ice extent, volume, and seasonal cycle of growth and melt.

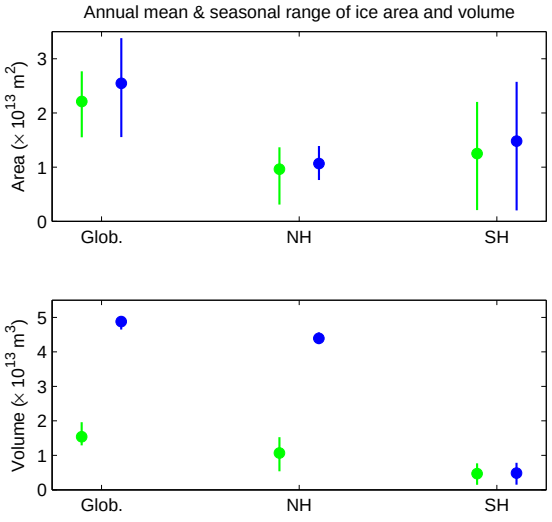

Figure C.1: Annual mean and seasonal range of sea ice area and volume simulated for preindustrial (green) and LGM (blue) climates. Values are global (Glob.), and for the Northern Hemisphere (NH) and Southern Hemisphere (SH).

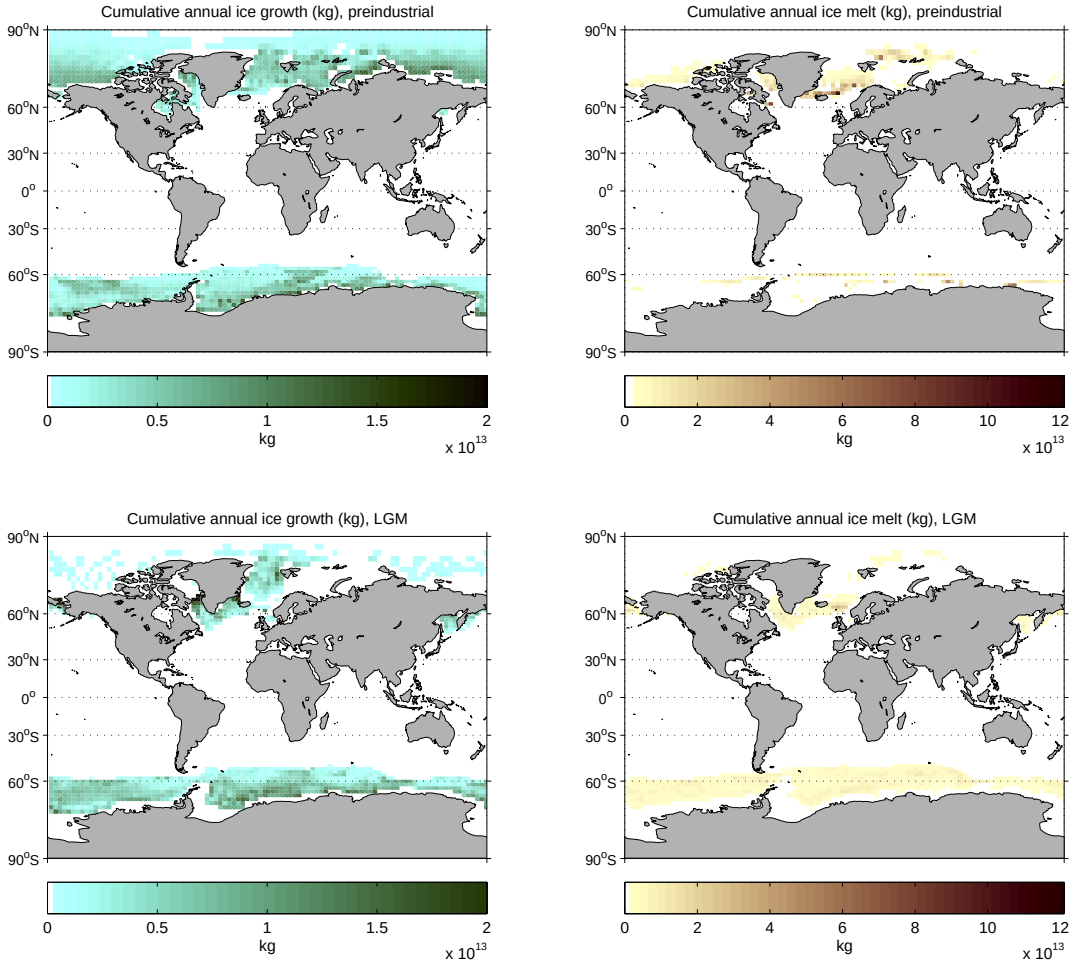

Figure C.2: Annual cumulative sea ice growth (left) and melt (right) (kg) simulated for the preindustrial (top) and LGM (bottom).

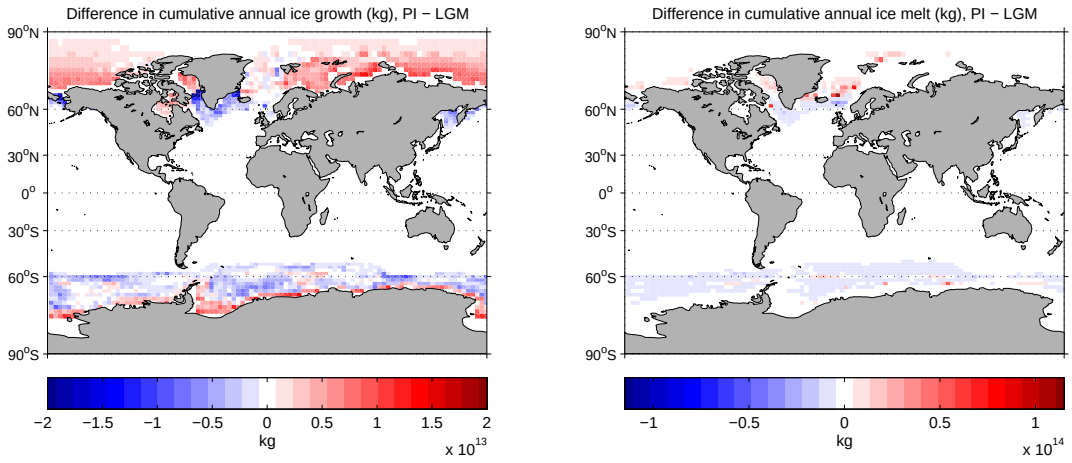

Figure C.3: Difference between preindustrial and LGM (PI-LGM) annual cumulative sea ice growth (left) and melt (right) (kg).